Trabajo Fin de Máster

Máster Universitario en Ingeniería Industrial

Coils and power supply design for the SMall Aspect Ratio Tokamak (SMART) of the University of Seville

Author: Manuel Agredano Torres

Tutors: Juan Manuel Ayllón Guerola and Manuel Barragán Villarejo

Dpto. de Ingeniería Mecánica y Fabricación
Dpto. de Ingeniería Eléctrica
Escuela Técnica Superior de Ingeniería
Universidad de Sevilla

Sevilla, 2020

Trabajo Fin de Máster
Máster Universitario en Ingeniería Industrial

Coils and power supply design for the SMall Aspect Ratio Tokamak (SMART) of the University of Seville

Autor:
Manuel Agredano Torres

Tutores:
Juan Manuel Ayllón Guerola
Profesor Ayudante Doctor Interino
Manuel Barragán Villarejo
Profesor Ayudante Doctor

Dpto. de Ingeniería Mecánica y Fabricación
Dpto. de Ingeniería Eléctrica
Escuela Técnica Superior de Ingeniería
Universidad de Sevilla

Sevilla, 2020

Trabajo fin de Máster: Coils and power supply design for the SMall Aspect Ratio Tokamak (SMART) of the University of Seville

Autor: Manuel Agredano Torres

Tutores: Juan Manuel Ayllón Guerola y Manuel Barragán Villarejo

El tribunal nombrado para juzgar el TFM arriba indicado, compuesto por los siguientes miembros:

Presidente:

Vocales:

Secretario:

Acuerdan otorgarle la calificación de:

Sevilla, 2020

El Secretario del Tribunal

A mi familia

AGRADECIMIENTOS

En primer lugar, quiero dar las gracias a mis tutores, Juanma y Manuel, por todo su apoyo y el esfuerzo extra que hubo que hacer en los últimos momentos antes de la finalización de este trabajo, el cual ha merecido la pena. Agradecer también al departamento de ingeniería eléctrica y al grupo de Ciencia del Plasma y Tecnología de Fusión por la gran experiencia que he tenido en estos años.

Especial gracias a Manolo García Muñoz y nuevamente a Juanma, habéis sido una excelente guía y apoyo en mis primeros pasos por la carrera investigadora, y seguiréis siendo mis referentes en mi nuevo camino. También a Manuel Toscano Jiménez, quien sembró la semillita para adentrarme en un campo tan apasionante como la fusión.

Agradecer a mis padres su incondicional apoyo durante todos estos años, y en especial durante estos últimos meses de confinamiento en plena pandemia. Tanto ellos como mi hermana son la roca en la que siempre puedo confiar para no caer.

Dar las gracias también, por toda la ayuda recibida, a compañeros y amigos como Juanjo, Juanlu, Scott, Jorge y muchos más que habría que mencionar. Pero en especial a Alessio y a los dos Javis, aparte de compañeros de trabajo, y de agobios también, os habéis convertido en grandes amigos que han conseguido que estos últimos años hayan sido increíbles.

Manuel Agredano Torres

Sevilla, 2020

RESUMEN

Durante el último siglo, la producción energética ha sido predominantemente abastecida por plantas de combustible fósil. Los efectos nocivos sobre el medio ambiente, que los recursos fósiles han causado, han despertado conciencia sobre la necesidad de una fuente alternativa de energía. Las energías renovables están liderando este cambio. Sin embargo, la dependencia en las condiciones climáticas de estas fuentes de energía, dificultan alcanzar un sistema 100% renovable. Por tanto, una fuente de energía diferente, actuando como central de base, podría complementar a un sistema con una alta penetración de energías renovables. La energía de fusión nuclear emerge como una solución prometedora para lograr una sociedad sostenible sin emisiones de gases de efecto invernadero ni residuos radiactivos de vida larga.

La investigación en fusión nuclear pretende obtener una planta comercial en las próximas décadas. Uno de los dispositivos mas avanzados es el tokamak, donde fuerte campos magnéticos crean y confinan un plasma donde la reacción de fusión se alcanza. Los campos magnéticos están inducidos por bobinas, que necesitan ser alimentadas por formas de corriente específicas controladas por sus fuentes de alimentación. Un nuevo dispositivo de investigación de fusión, SMART (*SMall Aspect Ratio Tokamak*, tokamak de pequeña relación de aspecto), está siendo diseñado en la Universidad de Sevilla para dos fases de operación. Por tanto, el objetivo principal de esta contribución es el diseño de un sistema capaz de crear y confinar el plasma dentro del dispositivo.

El equipo de física dentro del grupo de Ciencia del Plasma y Tecnología de Fusión ha obtenido las curvas de corriente requeridas para las dos fases de SMART. Utilizando las curvas como punto de partida, cada grupo de bobina es diseñado para soportar el calentamiento por efecto Joule durante la operación del tokamak para ambas fases. Con este fin, se define un modelo térmico analítico, y las restricciones debido a la geometría de la vasija son tenidas en cuenta para obtener el diseño de las bobinas.

Debido a las altas corrientes requeridas en los tokamaks, los sistemas de alimentación son una parte exigente del diseño. La mayoría de los tokamaks relevantes utilizan sistemas basados en tiristores y conectados a la red o a volantes de inercia. Sin embargo, siguiendo la tendencia actual, el diseño de un sistema de alimentación más flexible y modular, basado en IGBT y supercondensadores, se presenta en este documento para la primera fase de operación de SMART. Se explican las topologías y la estrategia de control de los sistemas de alimentación. El desempeño del sistema es validado en MATLAB Simulink, demostrando su viabilidad antes de la construcción del sistema.

ABSTRACT

During the last century, energy production has been predominantly supplied by fossil fuel power plants. The negative environmental effects that fossil fuels have caused, have raised awareness of an alternative source of energy. Renewable energies are leading this change. However, the dependency on weather conditions of these sources of energy, stood in the way of a 100% renewable energy system. Therefore, a different energy source, acting as baseload producer, could complement a system with high penetration of renewable energies. Nuclear fusion energy arisen as a promising solution to achieve a sustainable society without green-house effect gasses emissions and long-lived radioactive wastes [1].

Nuclear fusion research aims to reach a commercial nuclear fusion power plant in the next decades. One of the most advanced devices is the tokamak, where strong magnetic fields create and confine a plasma where the fusion reaction is achieved. The magnetic fields are induced by coils, which need to be fed by specific current waveforms controlled by their power supplies. A new research fusion device, SMART (SMall Aspect Ratio Tokamak), is being designed at the University of Seville for two operation phases. Therefore, the main goal of this contribution is to design a system capable of creating and confining the plasma inside the device.

The physics team of the Plasma Science and Fusion Technology group has obtained the current waveforms required for the two phases of SMART. Taking the current waveforms as starting point, each set of coils has been designed to withstand the Joule heating during the tokamak operation for both phases. To this end, an analytical thermal model is defined and the vessel geometry restrictions are considered to achieve the coils design.

Due to the large currents required in tokamaks, power supplies are a challenging part of their design. Most relevant tokamaks use thyristor-based power supplies fed by flywheels or the grid [2]. Nevertheless, following the present trend [3], the design of a more flexible and modular power suppliy, based on IGBTs and supercapacitors, is presented in this document for the first operation phase of SMART. The topologies and control system of the power supplies are explained. The performance of system has been validated in MATLAB Simulink, proving its feasibility before the construction of the system.

INDEX

TABLES INDEX

FIGURES INDEX

1 INTRODUCTION

Nowadays, society is rapidly increasing its energy demand. By the end of the century, it will have increased by a factor of three. However, the use of fossil fuels to supply the main part of this energy demand during the last century has caused important environmental damages. One of its main drawbacks is the emission of green-house effect gasses, which is the main factor for climate change. Hence, their use must be minimized in the near future and finally, completely avoided.

Renewables energies are emerging as a feasible solution for this problem. Nevertheless, they are intermittent sources of energy that depend on weather conditions. Therefore, a system with high penetration of renewable energies needs a back-up energy source [4].

A possible candidate for this role could be nuclear fusion energy, which is a source of energy currently under research. It could assume the role of providing a baseload energy production, complementing renewable energies. This source of energy does not emit green-house effect gasses, and, unlike conventional nuclear fission energy, there is no long-lived radioactive wastes and its fuel is almost unlimited [1]. Thus, the development of commercial nuclear fusion power plant could be the answer for achieving a fully sustainable society.

1.1 Nuclear fusion reaction

The first step to understand how a nuclear fusion power plant works is to study the reaction from which its energy is released. A fusion reaction occurs when two atomic nuclei join to form a heavier one. It is the opposite reaction to fission, where a heavy nucleus splits into lighter ones. The energy released in nuclear reactions is related to the difference between the potential energy of reactants and products. The potential energy of a nucleus is equal to the binding energy, which is the minimum energy required to disassemble an atomic nucleus into its component parts [5]. It is represented in Figure 1-1 for different elements and isotopes.

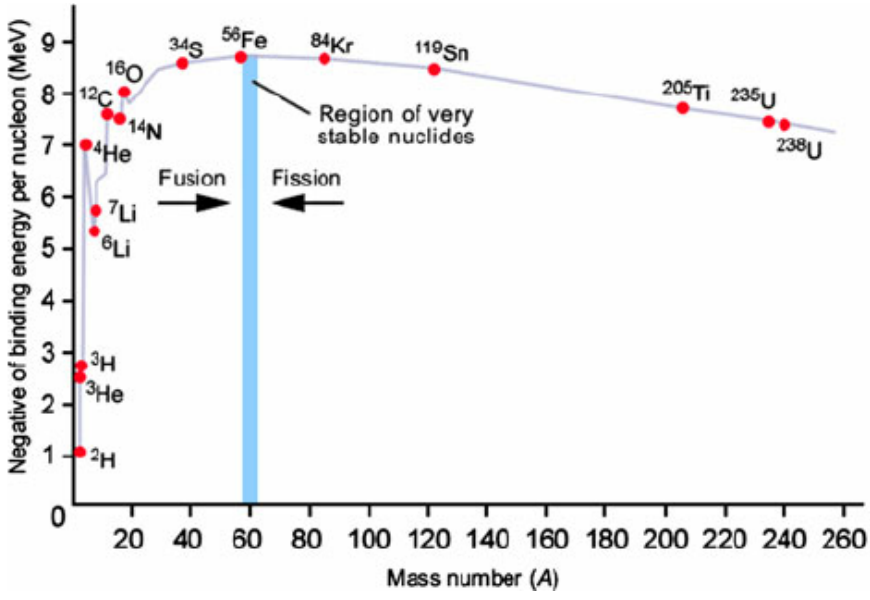

Figure 1-1: Binding energy, reprinted from [6]

Fe^{56} is the most stable element as it has the highest binding energy i.e. the lowest potential energy. In conventional nuclear power plants, nuclei as U^{235} or U^{238} undergo fission to create elements closer to Fe^{56}. However, the energy obtained from fusion reactions is much higher as the difference in the binding energy of the elements is greater. They are the reactions that occurs in stars as the sun. The main challenge to achieve the reaction is to surpass the potential barrier due to the repulsion of the two positive nuclei. In the stars, the strong gravitational forces allow particles to overtake this barrier and fuse.

Nevertheless, these forces cannot be replicated on Earth, so magnetics forces or lasers are used instead. This are the two main methods to try to achieve fusion, magnetic and inertial confinement. Furthermore, the candidate fusion reaction on Earth is the one with more possibilities to be achieved, which is related to a higher cross section (σ) [7]. The cross section for different reactions is shown in Figure 1-2.

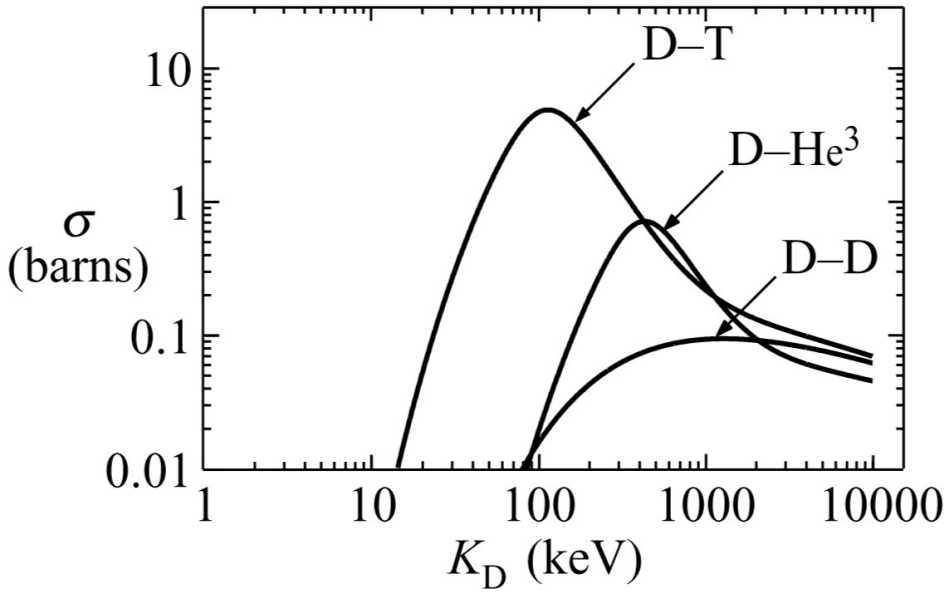

Figure 1-2: Experimental data of cross sections σ, reprinted from [7]

As it can be seen, this candidate reaction is the one with deuterium (D or H^2) and tritium (T or H^3) as reactants, represented in Equation (1-1) and Figure 1-3. The obtained products are an alpha particle (^{4}He) with 3.5MeV of kinetic energy and a neutron (n) with 14.1MeV.

$$H^2 + H^3 \rightarrow He^4 + n + 17.6\ MeV \tag{1-1}$$

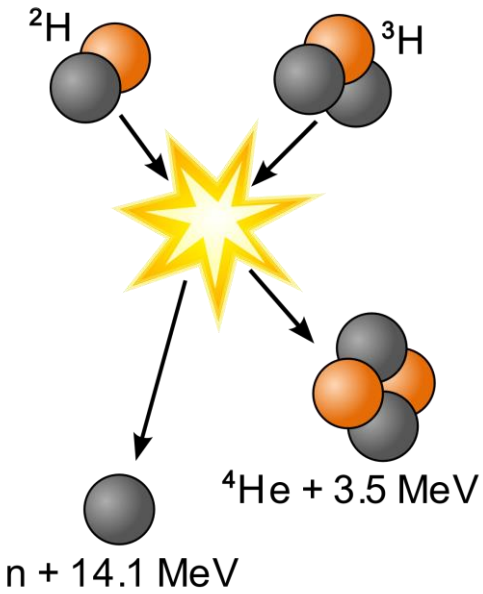

Figure 1-3: Deuterium-Tritium reaction, reprinted from [5]

1.2 Magnetic confinement

As it was mentioned in Section 1.1, magnetic confinement is one of the most extended methods to try to achieve a fusion device profitable enough to develop a commercial nuclear fusion power plant. The main idea is to heat deuterium and tritium up to the plasma state, where the electrons of the atoms move freely respect their nuclei. Therefore, plasma is an ionized gas and it can be confined using magnetics fields.

When the reaction takes place, the alpha particle is still trap in the magnetic field and its energy allows to maintain the chain reaction, colliding with other particles. However, the neutron, a particle without charge, escape from the confinement and hit the wall, heating it up. This heat can be extracted by cooling systems and produces electricity with similar thermodynamic cycles employed in conventional thermal power plant.

The continuous impact of neutrons to the walls of the device activate them and become radioactive. Another radioactive source is the tritium used as fuel. Nevertheless, the only radioactive waste would be the walls of the device, as the tritium is consumed in the reaction. The radioactive live of this waste is of around one to five hundred years, much less compare to long-live radioactive wastes of fission power plants, and the could be recycle for new power plants after one hundred years stored [1].

There are two main devices to achieve fusion by magnetic confinement, the tokamak and the stellarator. The main difference is that stellarators do not induce a plasma current, which is required in tokamaks. However, the stellarator requires complicated and twisted coils to obtain the required magnetic fields compared to the simple coils shapes of the tokamak. For this reason, the tokamak is the most advanced device nowadays and the most important fusion experiment under development, ITER, is a tokamak [1].

1.3 The tokamak and its coils groups

The tokamak is the most advanced fusion device that aims at becoming a feasible nuclear fusion reactor. It is important to highlight that most of nowadays tokamaks, except very few cases such as JET in England, or the future ITER, have not studied the fusion reaction itself. The main current goal of fusion research devices is to study matter in plasma state and minimize possible instabilities.

The plasma formed is controlled by the magnetic fields induced by different coils, giving the plasma the shape of a torus. It is characterized by 3 main coils groups: toroidal field coils, transformer coils or central solenoid and vertical or poloidal field coils. They are represented in Figure 1-4 [8]. Each of them has a different function, thus, different current waveforms need to be supplied to each coils group.

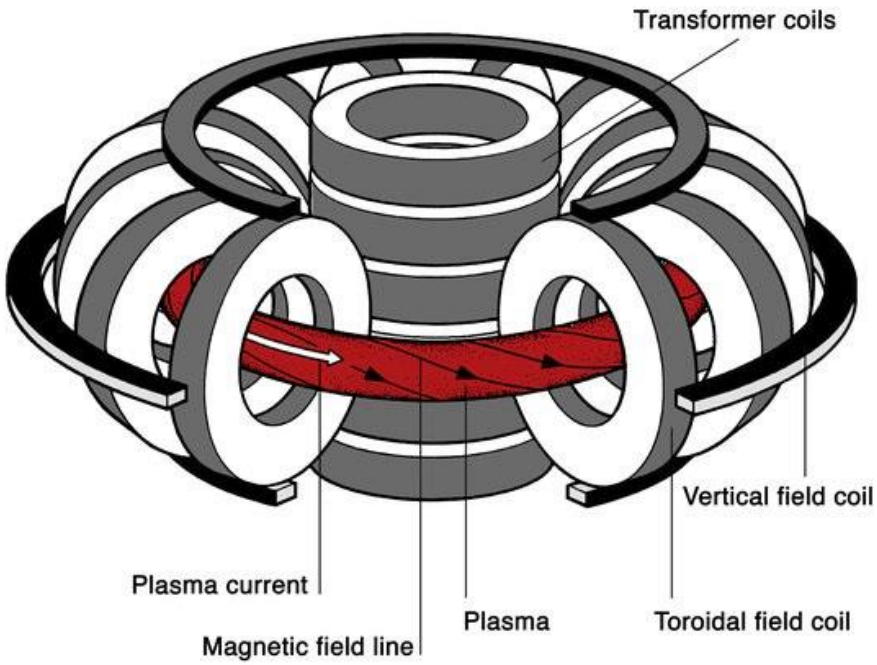

Figure 1-4: Tokamak coils scheme, reprinted from [8]

1.3.1 Toroidal Field Coils (TFC) function

The toroidal field coils (TFC) oversee the creation of the main magnetic field which gives the plasma the toroidal shape. The field has to be maintained constant during the hole plasma operation. The current required for all the TFC would like the one represented in Figure 1-5.

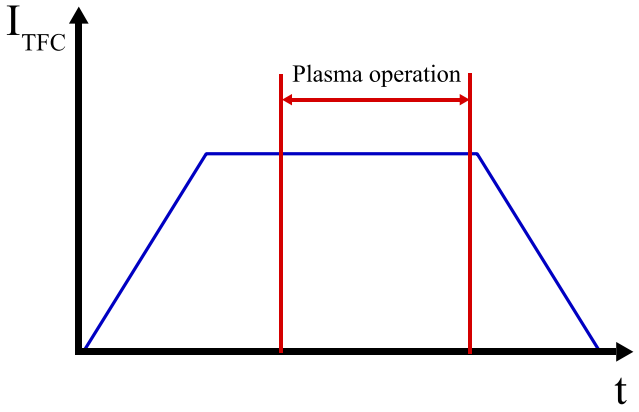

Figure 1-5: Generic TFC current waveform

1.3.2 Central solenoid function

The TFC are able to shape the plasma into its toroidal shape. However, the difference in the strength of the magnetic field between the inner and outer side of the torus causes a drift that make the particles scape. To avoid this drift, a current is induced in the plasma, which creates a second field that makes particles move in a helical form and finally confines the plasma. This plasma current is induced by transformer coils, also called central solenoid. An electromotive force efm, or loop voltage, is required to create and maintain the plasma current. Considering Faraday's law, represented in Equation (1-2), a linear increasing flux Φ is required, which is directly proportional to the current of the coil.

$$efm = -\frac{d\Phi}{dt} \tag{1-2}$$

Therefore, the central solenoid generally requires a steep slope for the creation of the plasma, also called breakdown, followed by a smoother slope for increasing the plasma current (I_p) and finally a smoother one for maintaining the plasma flattop. The current waveform compared to the plasma current is shown in Figure 1-6.

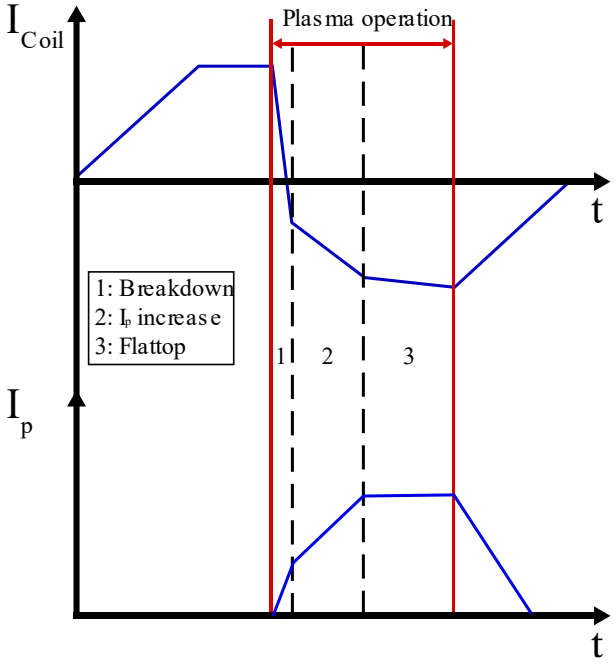

Figure 1-6: Generic central solenoid current waveforms compared to the plasma current

This make the tokamak operation pulsed. When the solenoid reaches its maximum current value, the tokamak has to be turned off and restart the operation. Nowadays, tokamaks experiments maintain the plasma in flattop conditions during a short period of time. This flattop pulse length varies from a few milliseconds to up to some minutes [9][10][2].

1.3.3 Poloidal field coils (PFC) function

The vertical or poloidal field coils (PFC) are in charge of shaping and position control of the plasma. Therefore, they generally have a constant current profile during the plasma breakdown and, afterwards, they transient into another constant profile during the flattop of the plasma. Each of them has different current waveforms, a generic representation is shown in Figure 1-7.

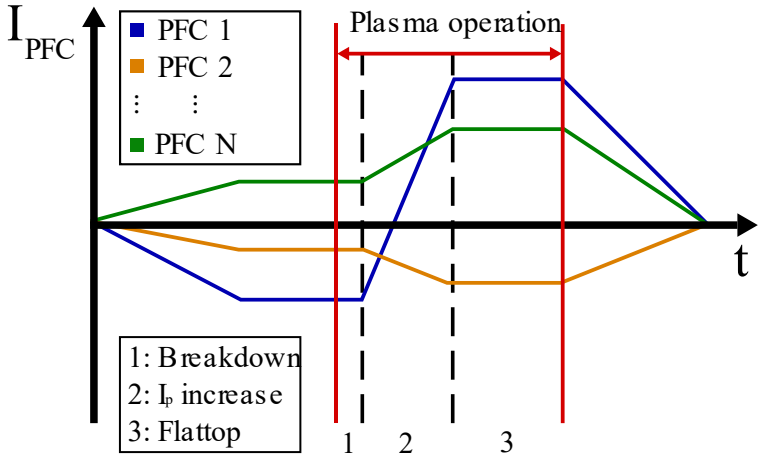

Figure 1-7: Generic PFC current waveforms

1.3.4 Power supply

In order to achieve the current waveforms required for the coils, they are connected to a power supply based on a power converter in charge of controlling the current and fed by a storage system. This system is represented in Figure 1-8. The TFC, as they all have the same current waveform, are connected in series to the same power converter.

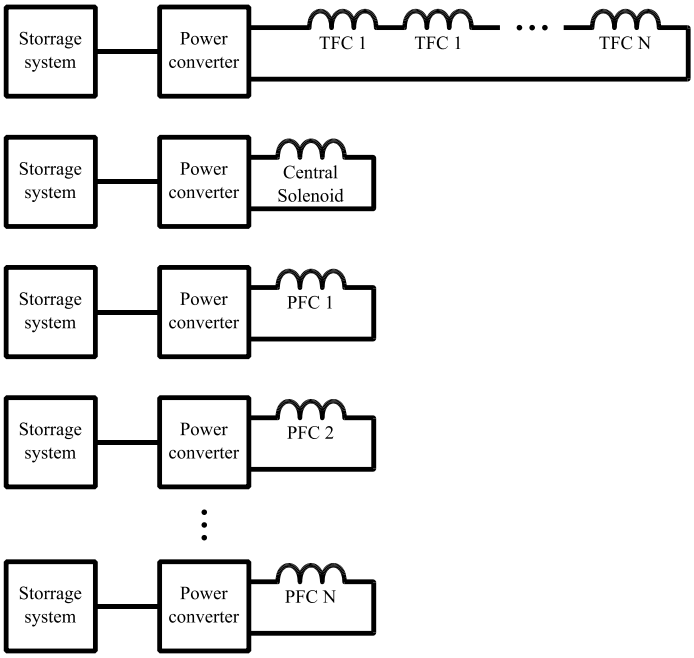

Figure 1-8: Generic power supply for each of the coils of a tokamak

Due to the pulsed operation of tokamaks, most of their power supplies are feed by storage systems. Large-scale tokamaks traditionally have used flywheels [2]. Medium and small tokamaks generally can be connected directly to the grid. However, with the development of supercapacitors as storage systems for pulse applications, it has become more efficient and economical to rely on supercapacitors modules than from the grid [3]. Even large tokamaks have started to plan the replacement of flywheels by supercapacitors [11].

1.4 Spherical tokamak

The subject of study of this contribution, explained in the next section, is a specific sub-kind of tokamak, the spherical tokamak. Spherical tokamaks differ from standard tokamaks mainly in its geometry. The aspect ratio A, as is shown in Equation (1-2), is the relation between the major radius, or geometric radius R_{geo}, and minor radius a of the toroidal shape of the plasma. As it is shown in Figure 1-9, the aspect ratio of a spherical tokamak is much lower, generally lower than two.

$$A = \frac{R_{geo}}{a} \tag{1-3}$$

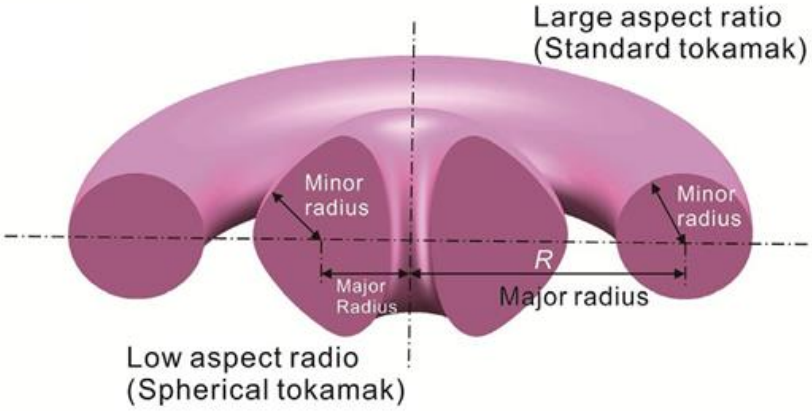

Figure 1-9: Comparison between standard and spherical tokamak [12]

This characteristic makes spherical tokamaks more compact devices and they obtain higher β numbers. The β number is the ratio between the plasma and the magnetic pressure. Therefore, a higher β number means that to obtain the same plasma pressure, a lower magnetic pressure is required, reducing the constructive and operational costs of the device [12].

Another advantage of these devices is to have a higher safety factor. The safety factor is the number of turns of a particle in the toroidal direction per turn in the poloidal one. A higher safety factor increases the magnetohydrodynamic stability of the plasma [13]. In Figure 1-10, typical aspect ratios and safety factors of spherical and standard tokamak is shown.

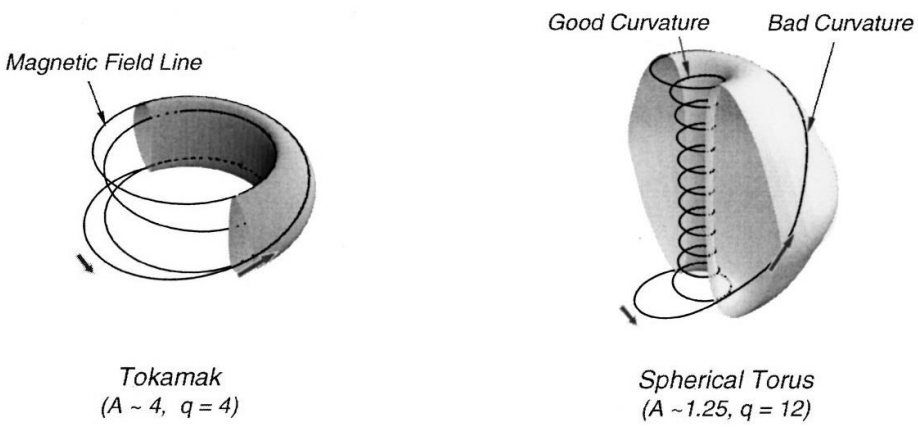

Figure 1-10: Aspect ratio (A) and safety factor (q) of a tokamak and a spherical torus, reprinted from [12]

Despite these beneficial factors, spherical tokamaks have as disadvantage the small space left in the inner side of the tokamak for the TFC and the central solenoid. Therefore, the optimization of this space, named central stack, is a key point of the design of these machines.

1.5 Motivation: the SMall Aspect Ratio Tokamak (SMART)

The plasma Science and Fusion Technology (PSFT) group, of the National Accelerators Centre (*Centro Nacional de Aceleradores,* CNA) and the University of Seville, plan to build a fusion device to enhance their contribution to fusion research and train future fusion engineers and physicists. The chosen device is a spherical tokamak due to the reduction of costs to achieve the same plasma pressure compare to a standard tokamak explained in Section 1.4.

It is named SMall Aspect Ratio Tokamak (SMART) and a 3D model is shown in Figure 1-11. SMART is currently under design and its construction will start by the end of year 2020. It is expected to obtain a first operation phase with low plasma parameters and then a second phase with an upgraded power supply in the future, enhancing the tokamak performance. As it have been explained in Section 1.3, the main plasma parameters in a tokamak are the toroidal field (B_t), plasma current (I_p) and flattop pulse length (τ). The parameters required for each operation phase of SMART are shown in Table 1-1.

One of the main components in the design of a tokamak are the coils responsible for generating the magnetic field needed for confining the plasma. To be able to create the required fields, the coils need to be supplied by specific current waveforms controlled by their power supplies.

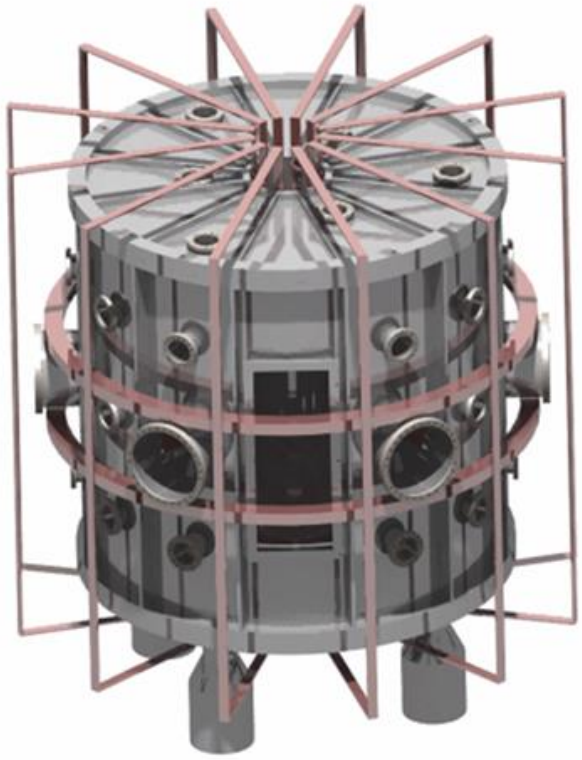

Figure 1-11: SMART 3D model

Table 1-1: Plasma parameters for the two operation phases of SMART [14]

Phase	**B_t (T)**	**I_p (kA)**	**τ (ms)**
1	0.1	30	20
2	0.3	100	100

1.6 Objectives and scope

The main goal of this contribution is to design a system able to generate the suitable magnetic fields required to create and confine the plasma inside SMART by controlling the currents waveforms of its coils. To achieve this objective, a series of tasks within the project have being developed that can be considered secondary objectives and are presented as the following chapters:

- Chapter 2: Reference fusion devices

To have a better understanding in order to design the coils and power supplies for SMART, a review of reference devices is presented. Coils from spherical tokamaks as GLOBUS-M, MAST or VEST will be described as well as power supplies from VEST and other fusion devices, such as PROTO-SPHERA or ASDEX Upgrade.

- Chapter 3: SMART and operational limits

SMART is presented together with its main components to be able to confine the plasma, the coils and power supplies. The current waveform of each coil depends on their function confining the plasma. The final current waveforms for different plasma scenarios are presented. These waveforms have been obtained by the physics team of the PSFT group for the two operation phases of SMART and only a short explanation of its obtention is presented in this work. However, they are a key point for the design as they are used to define the maximum operational limits for the coils and power supply.

- Chapter 4: Coils design

Considering the operational limits defined in Chapter 3, a thermal model has been used to obtain the minimum cross-section required for each of the coils in order to withstand the two operation phases of SMART. For some of the coils, water cooling has been considered. After the geometric definition of the coils, their electrical parameters are also determined.

- Chapter 5: Power supply design

With the operational limits for the first operation phase of the device defined in Chapter 3 and the resistance and inductance of each of coils from Chapter 4, the power supplies can be dimensioned. In this Chapter, the power supply will be designed to fulfill the operational limits of the coils, in the most economic and robust way, for the first operation phase of SMART.

2 REFERENCE FUSION DEVICES

Fusion devices require coils in order to induce the magnetic field used to create and confine a plasma inside of them. To achieve this aim, coils have to be fed and controlled by power supplies. In this chapter, a state of the art is presented of the coils and power supplies of references fusion devices. Coils of others spherical tokamaks like Globus-M, MAST and VEST are described, followed by power supplies systems from fusion devices as VEST, PROTO-SPHERA and ASDEX Upgrade.

2.1 Globus-M

Globus-M is a spherical tokamak located in the Abram Fedorovich Ioffe Institute from St. Petersburg, Russia. It was built in 1998. It has a plasma minor radius of 0.24m, a plasma major radius of 0.36m and a toroidal field of 0.5T [15]. Nowadays, this tokamak has been upgraded to Globus-M2, but the description of this section is based on the first version of the device. The tokamak model is show in Figure 2-1 and its main parameters are in Table 2-1.

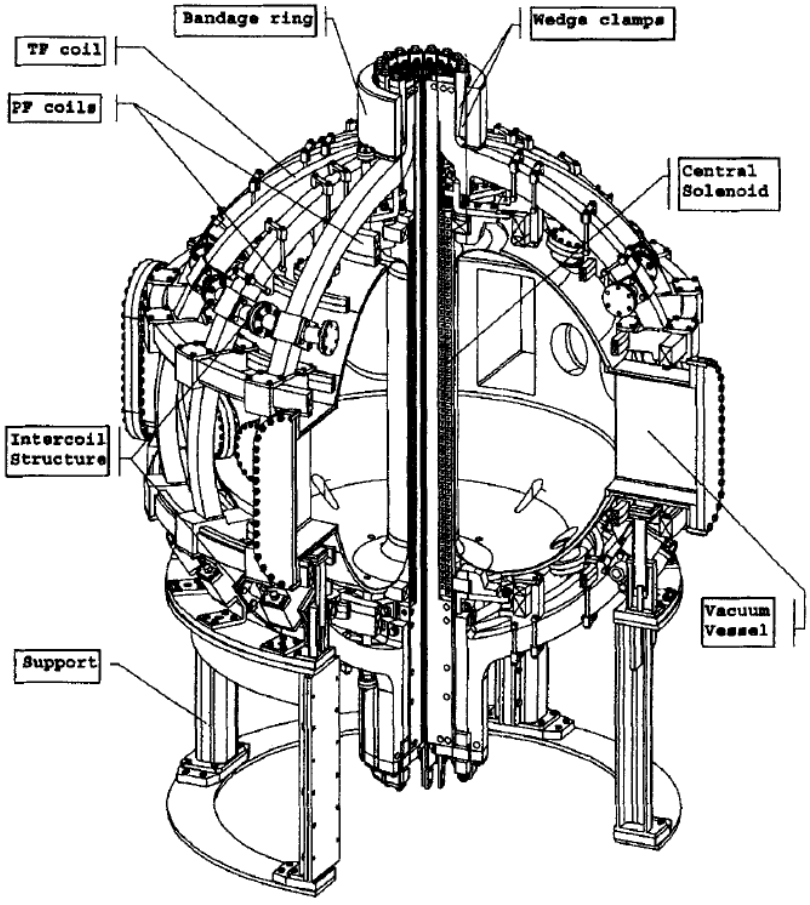

Figure 2-1: Globus-M 3D model, reprinted from [15]

Table 2-1: Main parameters of Globus-M [15]

Parameters	Values
Chamber dimension (m)	Φ 2 (D) x 2.6 (H)
Aspect ratio	1.5
Toroidal field (T)	0.5
Plasma current (kA)	300
Pulse length (ms)	300

2.1.1 Coils design

As a tokamak, explained in Section 1.3, Globus-M has three group of coils: TFC, the central solenoid and PFC. The TFC, as it is shown in Figure 2-1, consist of 16 turns with inner legs, located inside the central stack, and outer limbs. The outer limb has a 60x80mm^2 cross-section.

However, due to the lack of space in the central stack, inner legs have a smaller cross-section, requiring water-cooling. The cross section of the TFC inner legs is represented in Figure 2-2. The insulation between each of the inner legs has 2mm of thickness.

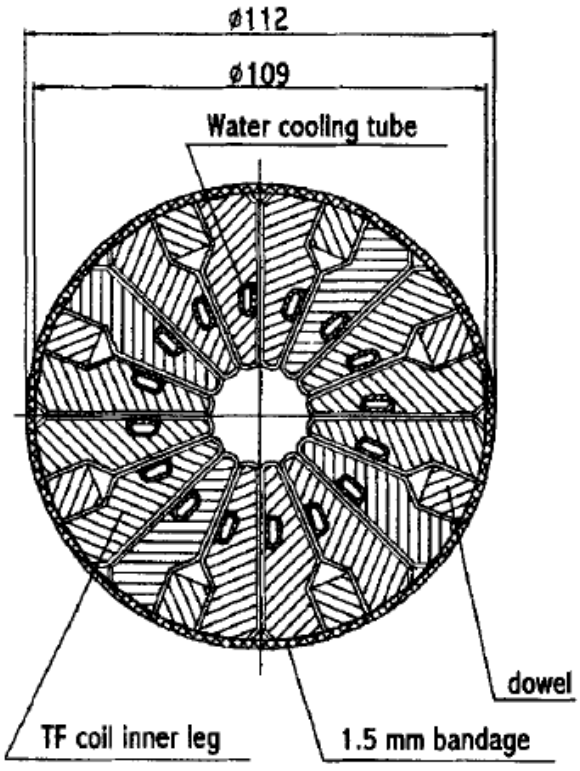

Figure 2-2: Globus-M TFC inner legs cross-section, reprinted from [15]

In this type of devices, the cooling system does not reduce the temperature increase during the discharge significantly, because of the high currents and short times required in the experiment, but it is useful to reduce the cooling down time of the coils between two discharges [16].

Regarding the central solenoid, it has the shape of a long circular coil of 2 layers with 60 turns each. The insulation thickness between turn to turn is 2.5mm. The cross-section of each turn is 20x20mm^2 and it has a cooling hole diameter of 6mm, represented in Figure 2-3.

There are 9 pairs of PFC. Three pairs are for plasma shaping and position monitoring, other three pairs are for vertical and horizontal control and the last three are connected in series to compensate the central solenoid stray field. They have a section of 6x6mm and a cooling hole diameter of 3mm.

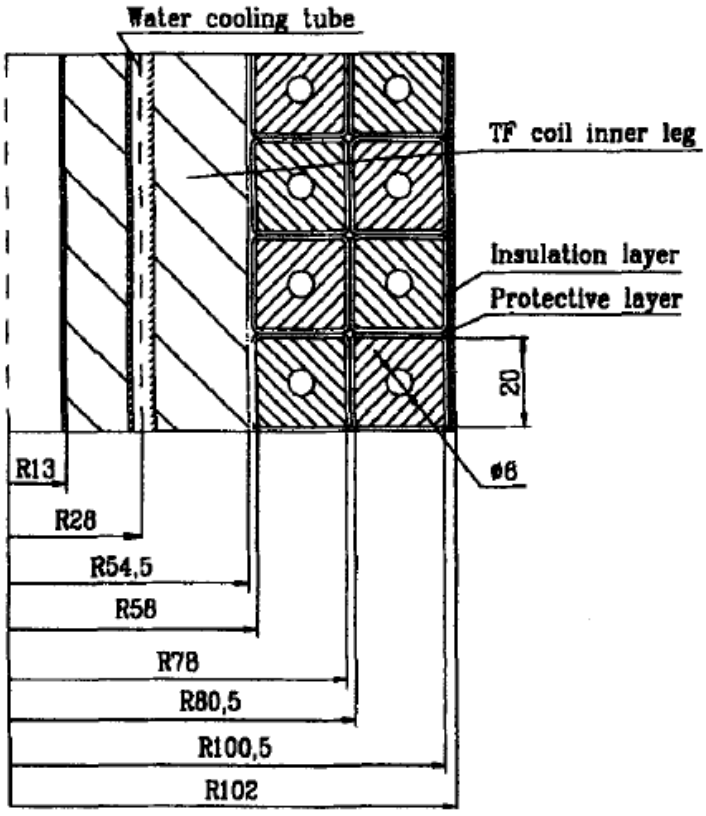

Figure 2-3: Central solenoid cross section, reprinted from [15]

2.2 MAST

The Mega Amp Spherical Tokamak (MAST) is a spherical tokamak of the Culham Centre for Fusion Energy (CCFE) in United Kingdom. It has a mayor radius of 0.7m and a minor one of 0.5m and a maximum toroidal field coil of 0.63T [17]. The rest of parameters are shown in Table 2-2. As well as Globus-M, nowadays is under development an upgrade called MAST-U, but the following description is just about MAST.

Table 2-2: Main parameters of MAST [17]

Parameters	Values
Chamber dimension (m)	Φ 4 (D) x 4.4 (H)
Aspect ratio	1.4
Toroidal field (T)	≤0.63
Plasma current (MA)	≤2.2
Pulse length (s)	1÷5

2.2.1 PFC design

The scale of this tokamak is much larger than SMART. However, it has the interesting approach of including the PFC inside the vacuum vessel. If they were outside, the rectangular shape of the vessel would place the PFC too far from the plasma. With this configuration, the power demand of the coils decreases as they are closer to the plasma. Furthermore, the shielding effect, that the eddy currents of the vessel produce during the current variations of the PFC, is avoided. As it is shown in Figure 2-4, there are 5 pairs of PFC and all of them are water-cooled with hollow conductors. They are enclosed in a stainless steel layer of 3mm, which acts as the vacuum boundary [17].

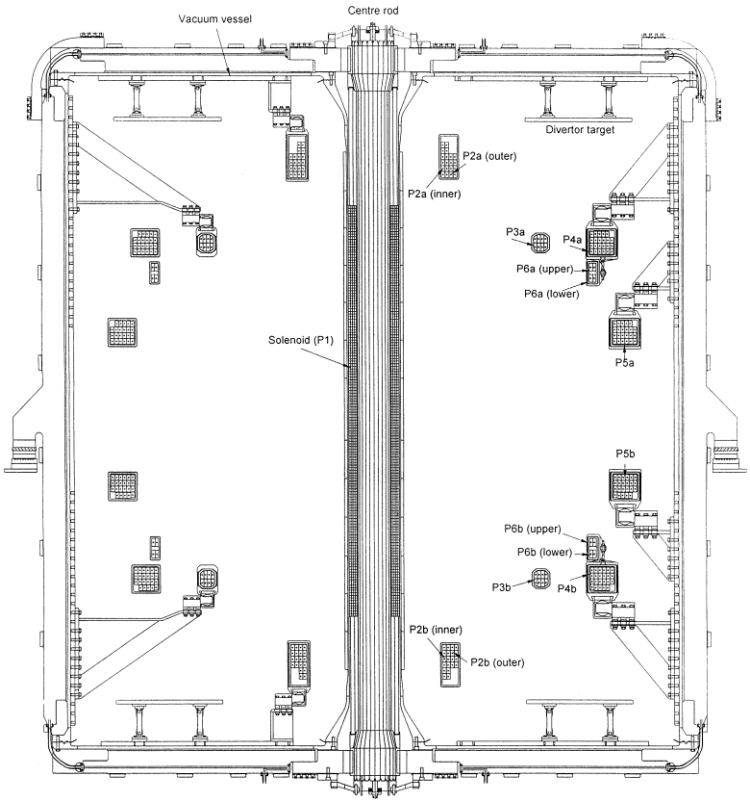

Figure 2-4: MAST cross-section, reprinted from [17]

2.3 VEST

The Versatile Experiment Spherical Torus (VEST) is a spherical tokamak of the Centre of Advance Research in Fusion Reactor Engineering at Seoul National University, South Korea. Its first plasma was in 2013. It has a mayor radius of 40cm, minor one of 30cm and a toroidal field of 0.1T. The rest of parameters are in Table 2-3.

VEST has one main chamber in the middle and two small ones in the upper and lower part. The design tries to achieve the double null merging compression [18], where two small plasmas are first created and then converge in the middle to obtain a larger one, as it is represented in Figure 2-5. However, VEST is also able to start up the main plasma in a conventional way and have similar parameters to the first operation phase of SMART.

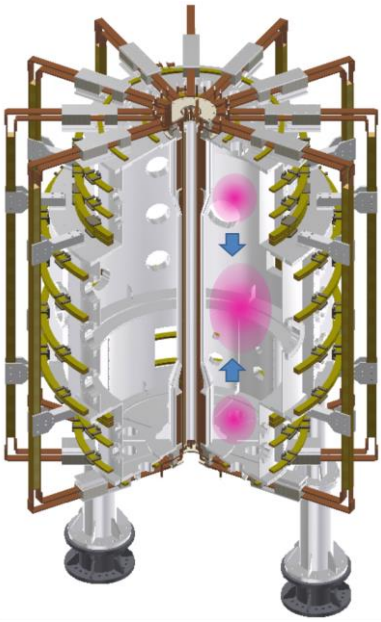

Figure 2-5: VEST with a simple representation of the double null merging process, reprinted from [18]

Table 2-3: Main parameters of VEST [18]

Parameters	Values
Chamber dimension (m)	Main chamber: Φ 1.6 (D) x 1.2 (H) Small Chambers: Φ 1.2 (D) x 0.6 (H)
Aspect ratio	>1.3
Toroidal field (T)	0.1
Plasma current (kA)	30
Pulse length (ms)	40

2.3.1 Coils design

The TFC, as it happened with Globus M in section 2.1.1, have a smaller section in the inner side located inside the central stack. The inner side cross section is 12x12mm^2 with a water-cooling hole diameter of 6mm, while the outer side cross section is 50x10mm^2, assembled in 12 coils of 2 turns each.

The role of the central solenoid is divided between three coils in this case. A long solenoid, named PF1, located inside the TFC is in charge of the start-up of the main plasma, while two partial solenoids, named PF2, induce the plasma in the upper and lower part. The cross section of this coils is 3.5x15mm^2. A detail description of the central stack is represented in Figure 2-6.

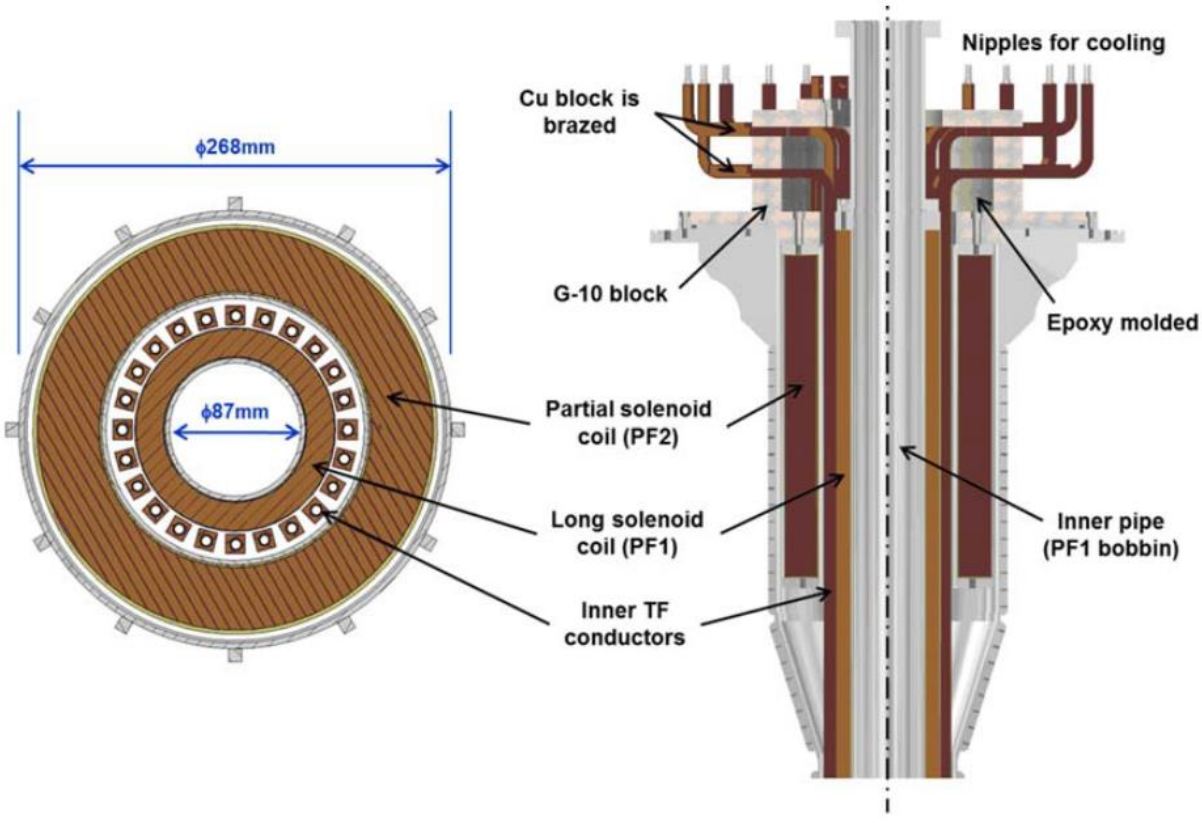

Figure 2-6: VEST radial and axial cross section, reprinted from [18]

The PFCs have cross sections of 6.5x6.5mm^2 with a water-cooling hole diameter of 3.5mm. The turns are assembled in several pancake modules in series of 2 turns in the axial direction and 6 turns in the radial one, except PF2 and PF4 which just have 4 turns in the radial direction. The position and function of each of the PFC and solenoids is presented in Figure 2-7.

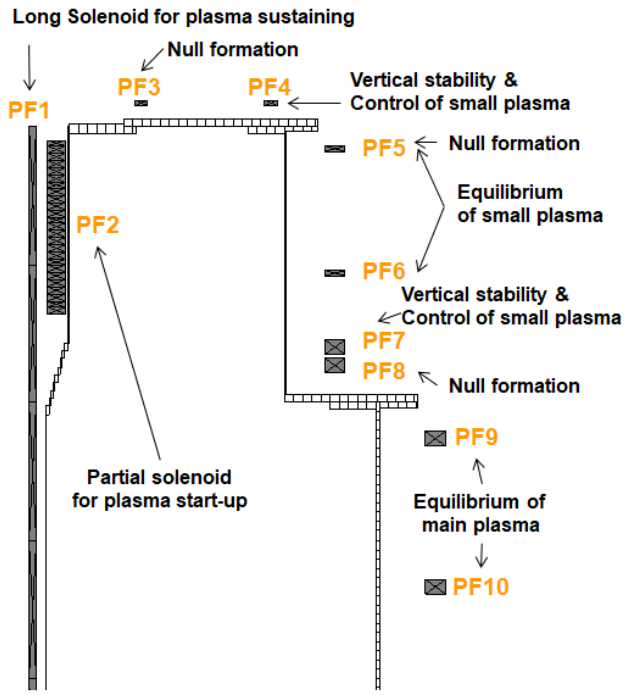

Figure 2-7: Solenoids and PFC position and main functions, reprinted from [18]

2.3.2 Power supply design

Each of the coils group requires a different kind of current waveforms. Therefore, the power supplies also differ. The TFC power supply needs to provide a constant current that can go up to 9.22kA. It is based on 10 battery modules connected in parallel represented in Figure 2-8.

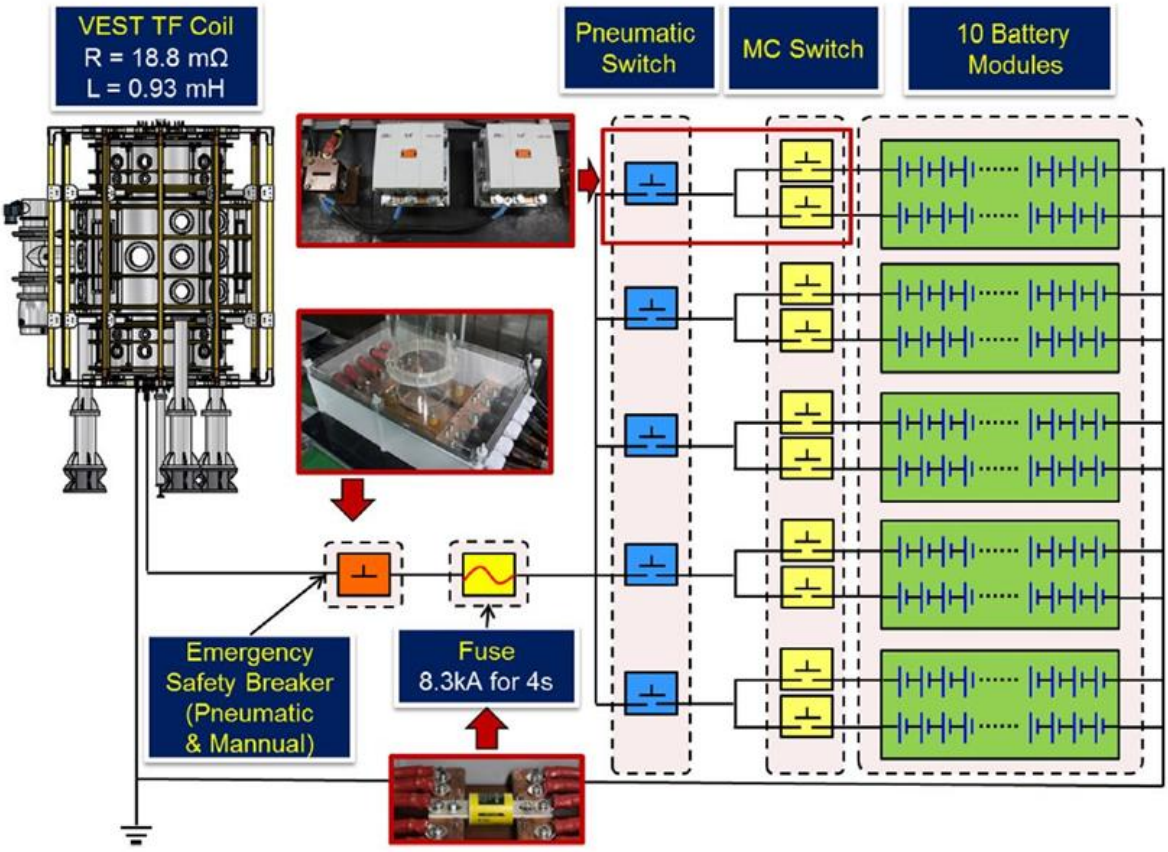

Figure 2-8: TFC power supply for VEST device, reprinted from [19]

Each module is composed of 20 deep-cycle batteries of 100 Ah of capacity connected in series [19]. Depending on the number of modules connected for the experiment, different discrete values of current can be obtained during the discharge, as it can be seen in Figure 2-9.

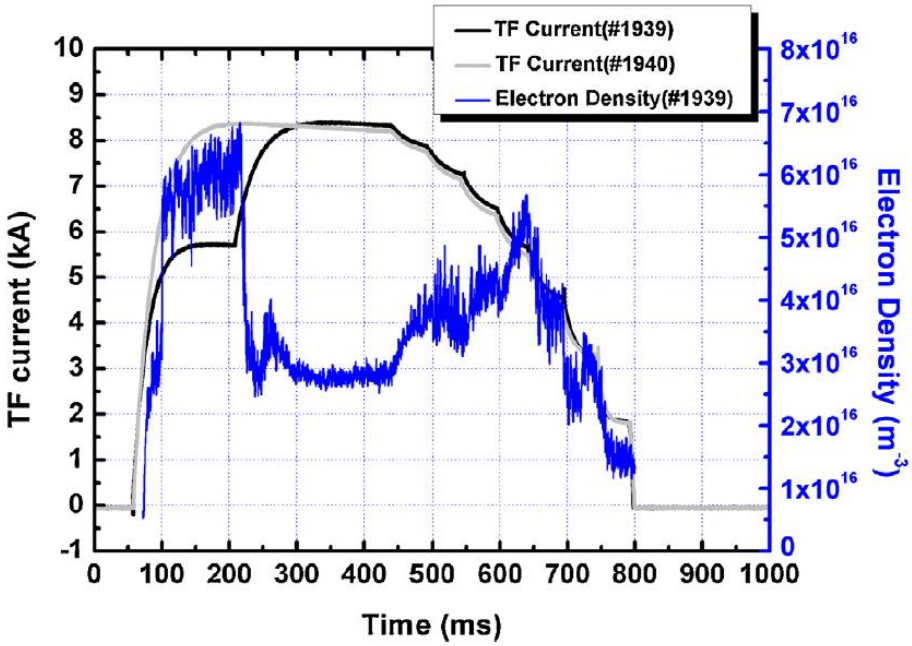

Figure 2-9: In experiment #1939, TFC current increase at 200ms due to the connection of 2 extra battery modules, changing the plasma density profile, reprinted from [19]

The long solenoid has a thyristor-based power supply and it is going to be replaced for another one of IGBTs. However, the behaviour of each power supply is very similar, they consist on second order dynamics of several RLC circuits. Both are shown in Figure 2-10.

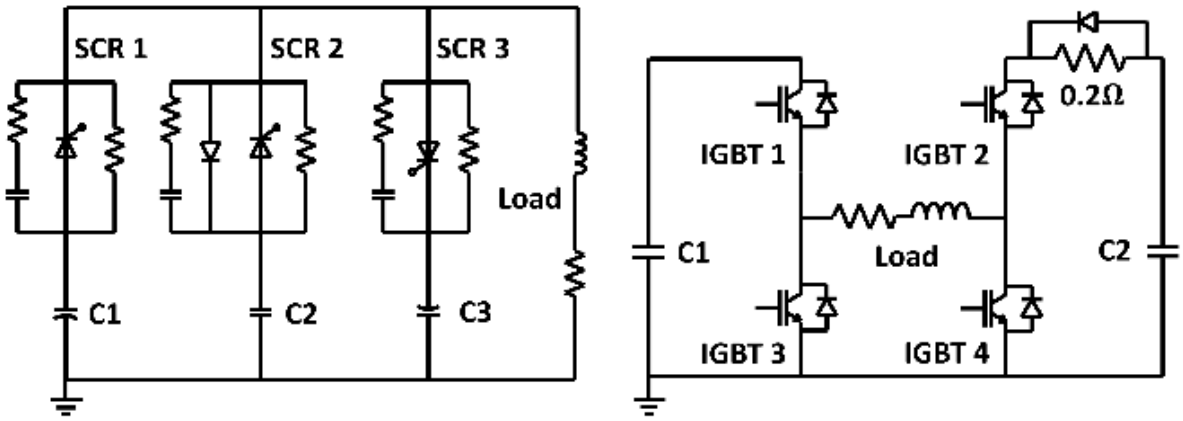

Figure 2-10: Thyristor-based PF1 power supply and IGBT-based one, reprinted from [20]

In the first power supply, the three thyristors (SCR 1, SCR 2 and SCR 3), are closed sequentially, obtaining a current waveform that goes from a maximum positive value to a negative one. This is the reason why this kind of power supplies for solenoids are called double-swing circuits.

In the case of the target power supply, first, IGBT 1 and IGBT 4 are closed until the current reaches the maximum positive value. At that point, these switches are opened and IGBT 2 and IGBT 3 are closed. In Figure 2-11, the dynamic of each circuit is shown and how the new system is able to achieve faster the loop voltage threshold required for plasma breakdown [20].

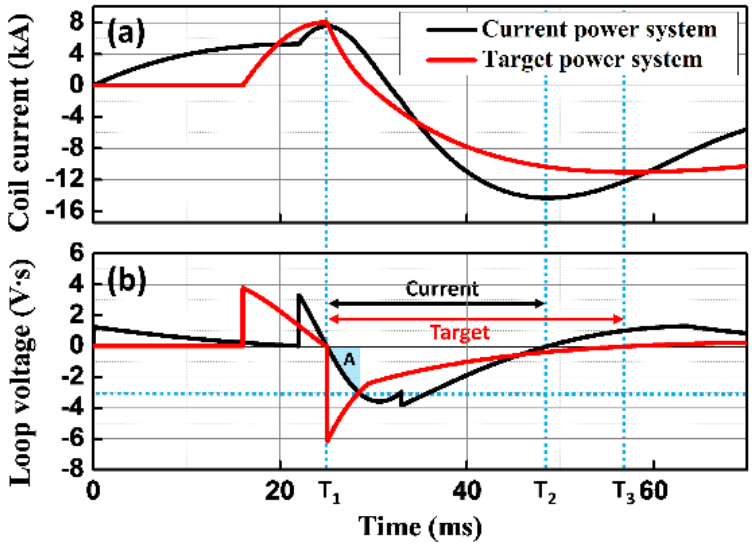

Figure 2-11: PF1 current and loop voltage for the present power supply and the target one, reprinted from [20]

Finally, the PFC power supply is based on a H-bridge converter, represented schematically in Figure 2-12. It is controlled by a feedback control. The control opens and closes the IGBTs to achieve the desire pre-defined current waveform by measuring the real value of the current in real time. In Figure 2-13, is shown how the current reference is achieved with a certain ripple [21].

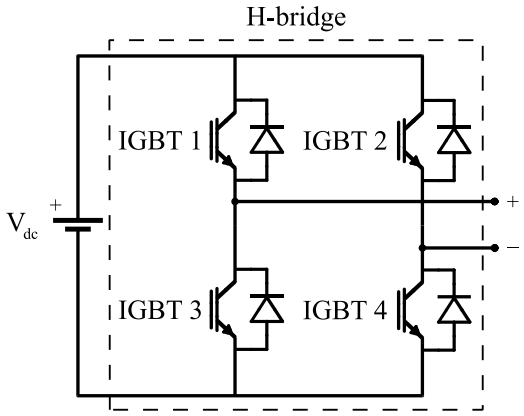

Figure 2-12: H-bridge converter, employed for the PFC power supply of VEST

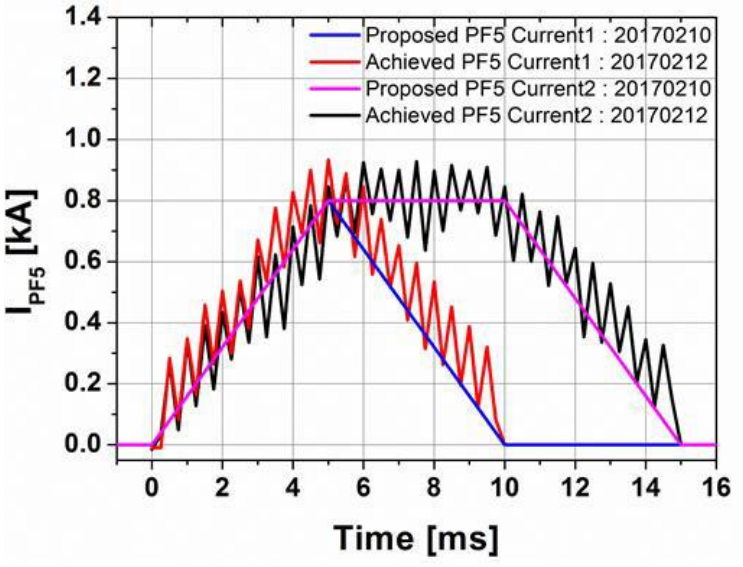

Figure 2-13: Controlled currents of PF5 compared to the target ones, reprinted from [21]

2.4 PROTO-SPHERA

The PROTOtype Spherical Plasma for HElicity Relaxation Assessment (PROTO-SPHERA) is a spherical tokamak with a spheromak configuration, where the metal central stack has been replaced for a plasma central stack. It has an aspect ratio around 1.2 ÷ 1.3 and it is expected to achieve a toroidal plasma current between 120 ÷ 240kA. The rest of parameters are shown in Table 2-4.

Its main advantage is to simplify the design of the vacuum vessel, shown in Figure 2-14, deleting the most critical part of most of spherical tokamaks, the central stack. It started to operate in 2014 at the Italian National Agency of New Technologies, Energies and Sustainable Development (ENEA), Italy [22].

Furthermore, this device only counts on PFC to achieve the plasma. The plasma central stack is created thanks to the upper and lower PFC and rest of the middle ones are in charge of the plasma shaping. Therefore, the use of TFC and a central solenoid is avoided.

Table 2-4: Main parameters of PROTO-SPHERA [22]

Parameters	Values
Chamber dimension (m)	Φ 2 (D) x 2.5 (H)
Aspect ratio	1.2 ÷ 1.3
Toroidal field (T)	0.05
Plasma current (kA)	120 ÷ 240
Pulse length (ms)	70

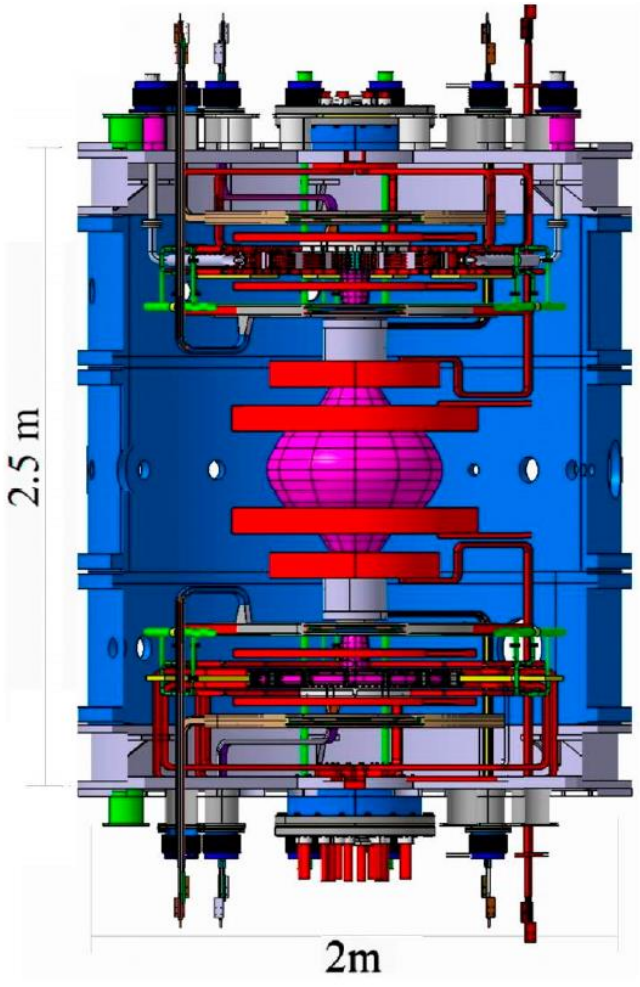

Figure 2-14: PROTO-SPHERA 3D model, reprinted from [22]

2.4.1 PFC Power supply design

The power supplies for the PFC is going to be updated to a modular system based on H-bridges converters and supercapacitors. The scheme of the present tested system is represented in Figure 2-15, where there are four main elements.

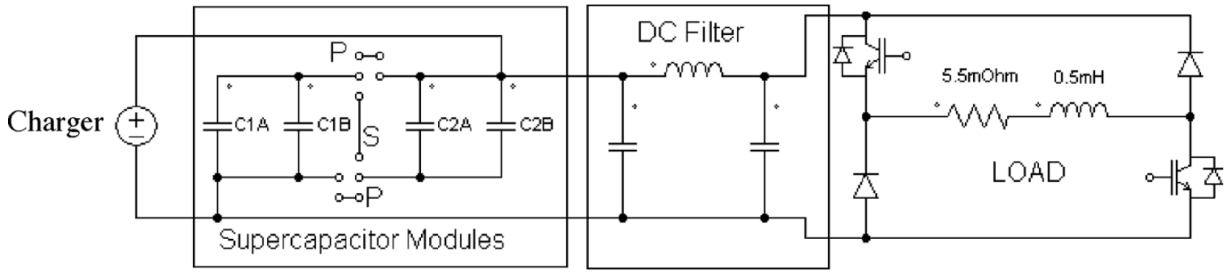

Figure 2-15: Simplified scheme of the PFC power supply for PROTO-SPHERA, reprinted from [3]

From right to left, the first element is the H-bridge converter, in this case modified to a two quadrants version, with the RL load connected. Then, a DC filter is connected between the converter and the storage system to protect it from a high current ripple.

The supercapacitors have a configurable system to increase the versatility of the power supply by connecting the 4 modules in parallel or in a 2x2 configuration. Finally, the auxiliary system for charging the supercapacitors is at the left side [3][23][24].

This system also has a feedback control to achieve a current that tends to the predefined reference. However, compare to VEST PFC power supply, the ripple in this case is lower than 0.5%. Furthermore, a specific solution was implemented to a achieve negative current slope that can go up to 200A/ms without increasing the voltage required in the supercapacitors. The current obtained and the voltage of the DC filter is shown in Figure 2-16.

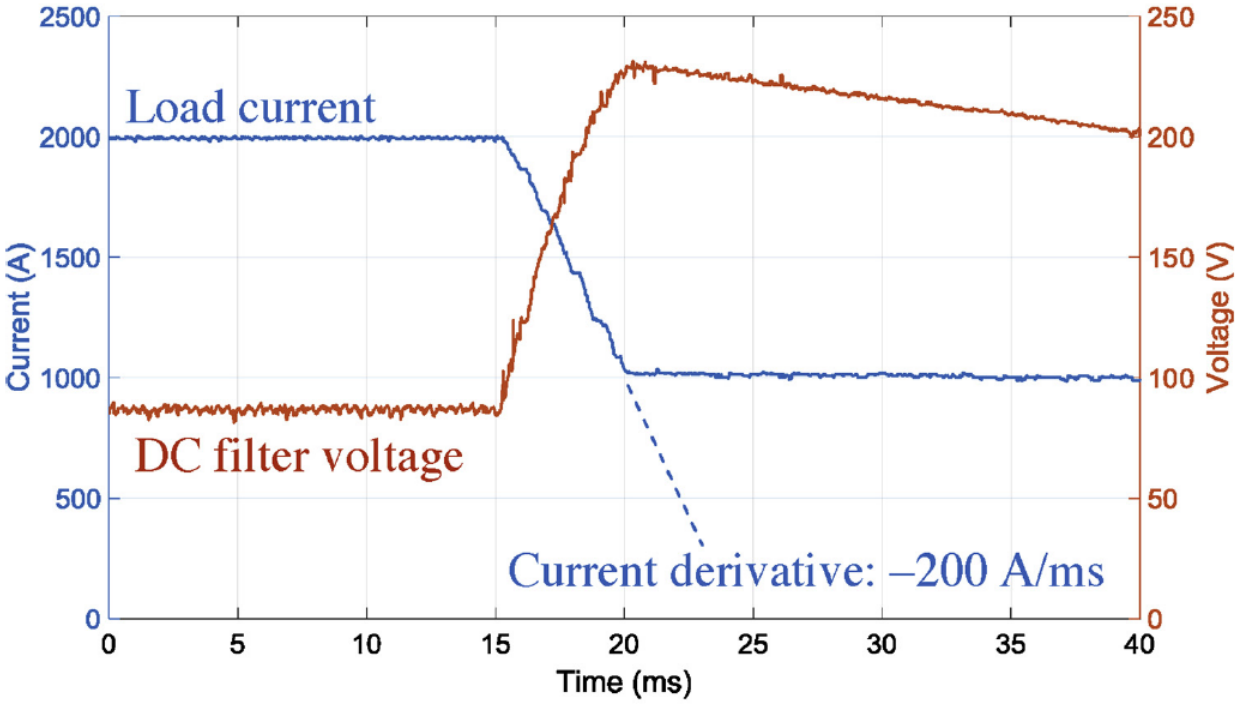

Figure 2-16: Current of the PFC prototype power supply for the PROTO-SPHERA and voltage in the DC filter, reprinted from [3]

2.5 ASDEX Upgrade

The Axially Symmetric Divertor Experiment (ASDEX) Upgrade, shown in Figure 2-17, is a tokamak located at the Max-Planck Institute for Plasma Physics in Garching, Germany. It went into operation in 1991. It has a mayor radius of 1.65m and minor radius of 0.5÷0.8m. The rest of parameters are in Table 2-5.

Table 2-5: Main parameters of ASDEX Upgrade [14]

Parameters	Values
Chamber dimension (m)	Φ 10 (D) x 9 (H)
Aspect ratio	2 ÷ 3.3
Toroidal field (T)	3.9
Plasma current (MA)	2
Pulse length (s)	10

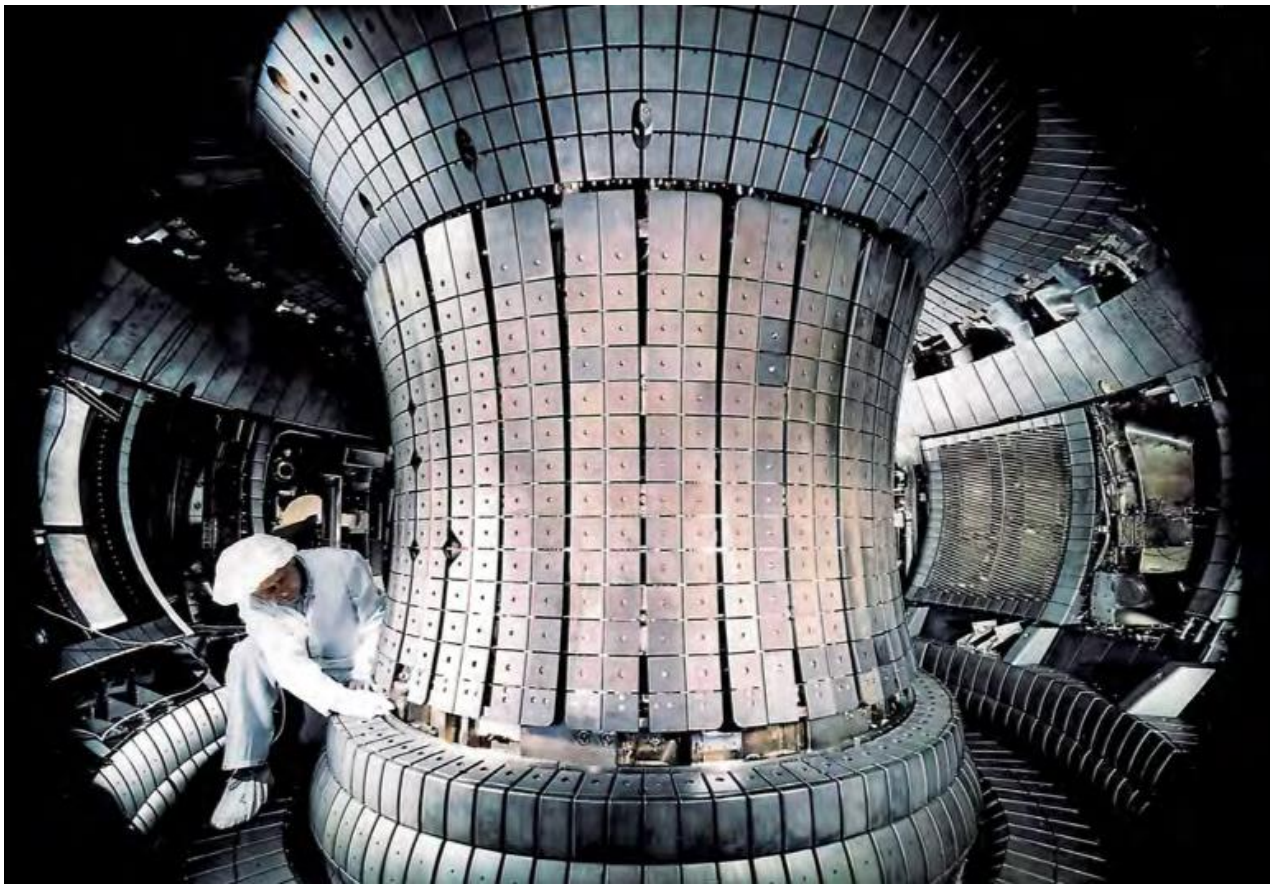

Figure 2-17: Image of the interior of ASDEX Upgrade, reprinted from [11]

2.5.1 TFC Power supply design

Nowadays, the power supply of ASDEX Upgrade is based on 3 flywheel generators and thyristor converters [25]. However, the biggest generator was built in 1973 and, if there is any major fault, it is not possible to replace it. Therefore, an alternative power supply based on supercapacitors and IGBT is currently under development in a prototyping phase [11].

The system is based on a Modular Multilevel Converter (MMC) topology, where different switching modules are connected in cascade to increase the voltage of the load. Furthermore, the branches are connected in parallel to increase the current. In this case, the switching modules are half bridges as is shown in Figure 2-18.

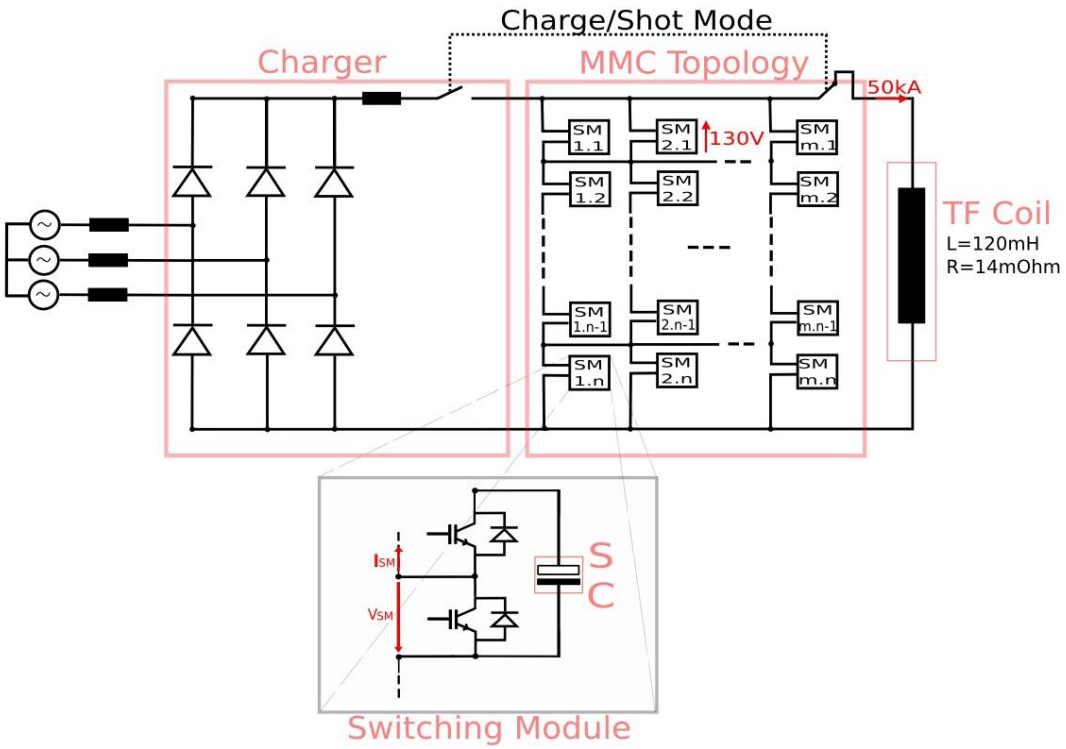

Figure 2-18: Alternative TFC power supply design for ASDEX Upgrade, reprinted from [11]

Each of the modules have two states. They can supply the voltage of the supercapacitor or cero. Therefore, depending on the number of modules connected in series and the voltage of the supercapacitors, the system obtain a range of discrete values of voltages, obtaining current waveforms as the one represented in Figure 2-19.

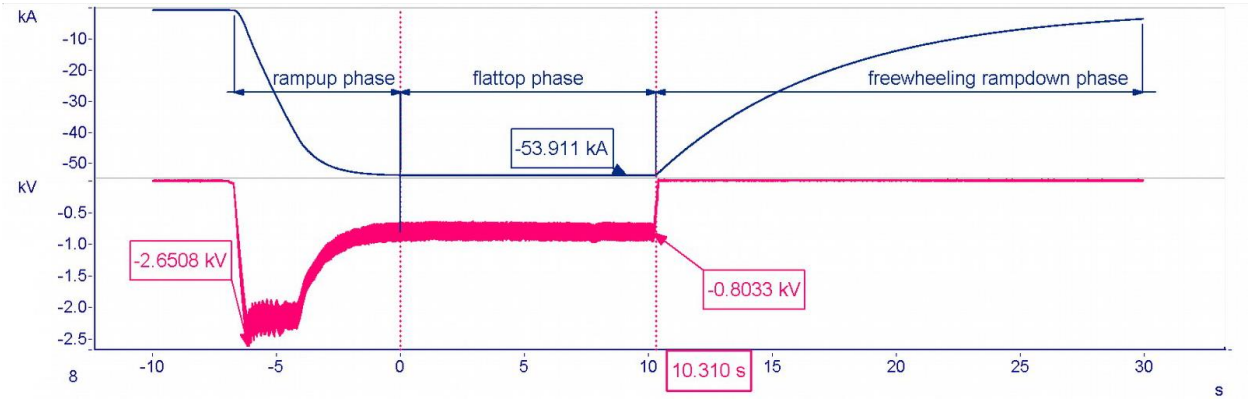

Figure 2-19: Simulated current and voltage for the alternative TFC power supply for ASDEX Upgrade, reprinted from [11]

3 SMART AND OPERATIONAL LIMITS

The spherical tokamak currently under design by the PSFT group, SMART, is described and a complete overview of its components is shown. Afterwards, a definition of the operational limits for voltage and current of the coils and power supplies, and magnetic pressure for the coils, is shown.

The voltages limit cannot be determined until the electrical parameters of the coils are obtained. However, the current waveforms required for coils of the tokamak to confine the plasma where obtained by the physics team of the PSFT and are presented as starting point of the design. Considering the current waveforms required for different plasma scenarios for phase 1, the operational limits for the power supplies are defined, whereas the operational limits for phase 2 are used for the coils design. Finally, with the maximum current for the coils design, the magnetic pressure of the coils is estimated.

It is important to stand out that all the designs and conclusions showed in this document are the result of an iterative work between the physics and engineering teams of the PFST group. The engineering specifications have been obtained from the physics models and then, the models were refined with the engineering design.

3.1 SMART description

SMART, represented in Figure 3-1, is a spherical tokamak designed by the PSFT group of the University of Seville and the CNA which is planned to start its construction at the end of the year 2020. It has a mayor radius of 0.45m and a minor radius of 0.25m. The goal is to achieve a plasma with an aspect ratio lower than 2 and with the parameters showed in Table 3-1 for two operation phases. The coils are designed to withstand beyond phase 2. However, the power supply design just achieves phase 1 and a future upgrade will be done to fulfill phase 2 requirements.

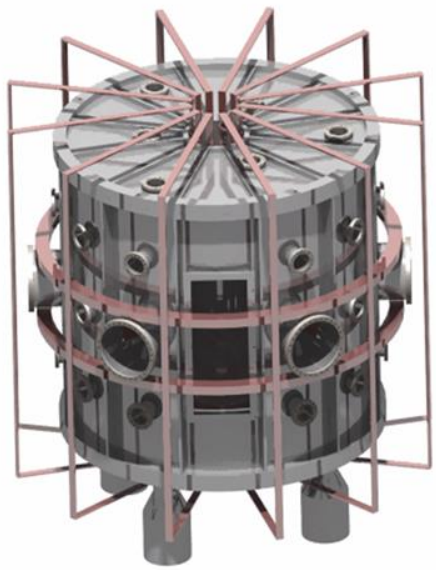

Figure 3-1: SMART 3D model

Table 3-1: Main parameters of SMART for its two operation phases [14]

Parameters	Phase 1	Phase 2
Chamber dimension (m)	Φ 0.815 (D) x 1.63 (H)	
Aspect ratio	≤2	
Toroidal field (T)	0.1	0.3
Plasma current (kA)	30	100
Pulse length (ms)	20	100

SMART is equipped with 12 TFC, a central solenoid and 4 pairs of PFC, represented in Figure 3-2. All of them will be made of copper. 3 pairs of PFC are located inside the vessel where the plasma is confined as is shown in Figure 3-3.

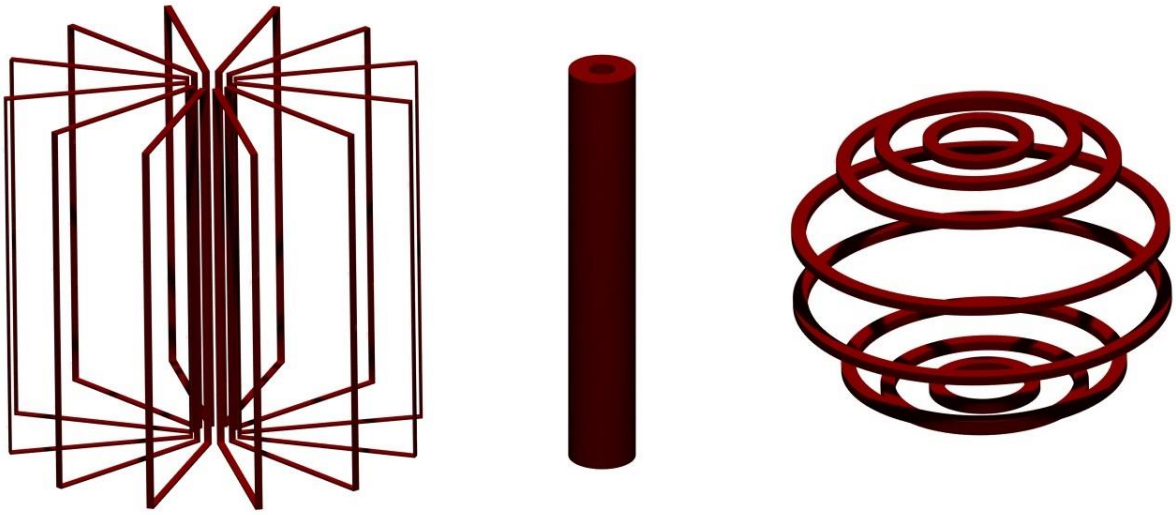

Figure 3-2: From left to right, simplified model of the 12 TFC, central solenoid and 8 PFC of SMART

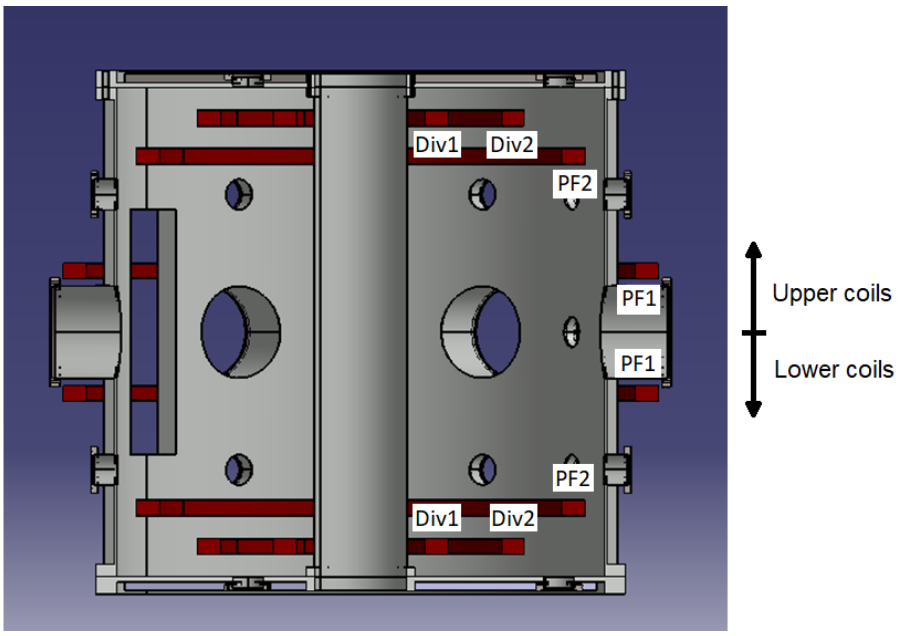

Figure 3-3: Cross section of SMART with 4 pairs of PFC distribution

The TFC consist of 4 turns each and are connected in series. Therefore, there are 48 turns in total and just one power supply. PFC have 24 turns and they have series connections in pairs except the upper and lower Div2 that will be independent. Hence, the PFC have 5 independent power supplies. Finally, the solenoid has 210 turns and one power supply for its operation. Thus, a total of 7 power supplies are required. A general scheme is presented in Figure 3-4, which is slightly changed in Chapter 5 after the final design of the system.

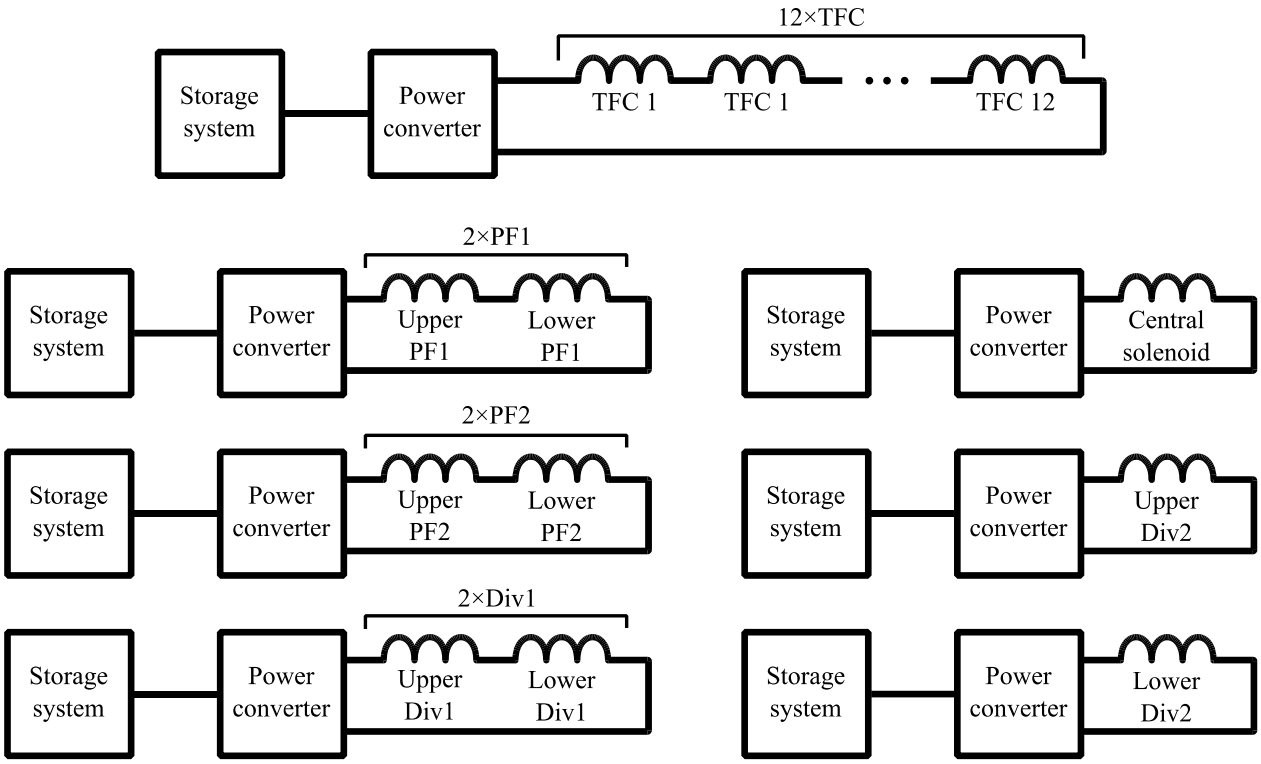

Figure 3-4: General scheme of the power supply required for SMART. Slight modifications are done after the final design of the system

3.2 Voltage operational limits

The voltage limit of the power supplies and coils cannot be estimated until the resistance and inductance of each coil is obtained. Considering the maximum currents and slopes , the voltage stand by a coil, and that need to be provided by the power supply, is obtained with Equation (3-1).

$$V = L \cdot \left(\frac{di}{dt}\right)_{max} + R \cdot I_{max} \tag{3-1}$$

3.3 Current waveforms for plasma confinement

The physics team of the PSFT group has calculated the current waveforms required to be fulfilled by each power supply for the operation phases 1 and 2. A short explanation of the obtention methods of this waveforms is done. Afterwards, for phase 1 and phase 2, the current waveforms for a baseline case are described and compared to two other plasma scenarios. The maximum values obtained from the comparison are used as the starting point for the definition of the operational limits for the power supply design, in the case of phase 1, and for the coils design, in the case of phase 2.

3.3.1 Obtention method for the TFC current

The TFC function is to provide the required toroidal field B_t in the mayor radius of the plasma. Therefore, it would just need to maintain a constant current during the hole experiment. The charging and discharging slopes is selected to avoid too high voltage requirements and charging times. This current value is obtained from Ampère's Law. In Equation (3-2), r_p is the mayor radius of the plasma, μ_0 is the magnetic permeability in vacuum and N_{TFC} is the total number of TFC turns.

$$I_{TFC} = \frac{2\pi \cdot r_p \cdot B_t}{\mu_0 \cdot N_{TFC}} \tag{3-2}$$

3.3.2 Obtention method for the central solenoid and PFC currents, the Fiesta code

The Fiesta code has been used to obtain the currents required for the central solenoid and the PFC for different plasma shape scenarios. In this document, it is described the waveforms for the baseline case, and it is compared to two others plasma scenarios.

The code started as a forward equilibrium solver for MATLAB developed by Geoffrey Cunningham from the Culham Centre for Fusion Energy [26]. This kind of codes solves the Grad-Shafranov equations to obtain the equilibrium of a plasma inside a tokamak [27].

Therefore, if the plasma current density profile is specified, together with the coils currents as boundary conditions, the equilibrium is solved and the rest of plasma parameters can be obtained, such as flux loop, magnetic field, pressure, etc.

Nowadays, the code has evolved into a toolbox with an object-oriented programming and can solve many other equilibrium-related problems. The Efit module has been used to obtain the coils currents for the plasma equilibrium based on the desired plasma parameters.

Moreover, the RZip code of the Centre for Research in Plasma Physics of Lausanne, Switzerland, which is integrated in Fiesta, allows dynamic simulations and the obtention of the currents required during the startup of the plasma.

3.3.3 Plasma scenarios

For each the two operation phases, the current waveforms have been studied for three plasma scenarios depending on the plasma triangularity. The plasma triangularity δ is define by Equation (3-3) as the mean value of the upper and lower triangularity, δ_{upper} and δ_{lower} respectively, which are obtained from Equation (3-4). For this calculus, is required the geometric or mayor radius R_{geo} of the plasma, the minor radius a and the points represented in Figure 3-5. The mayor and minor radii are defined in Equation (3-5).

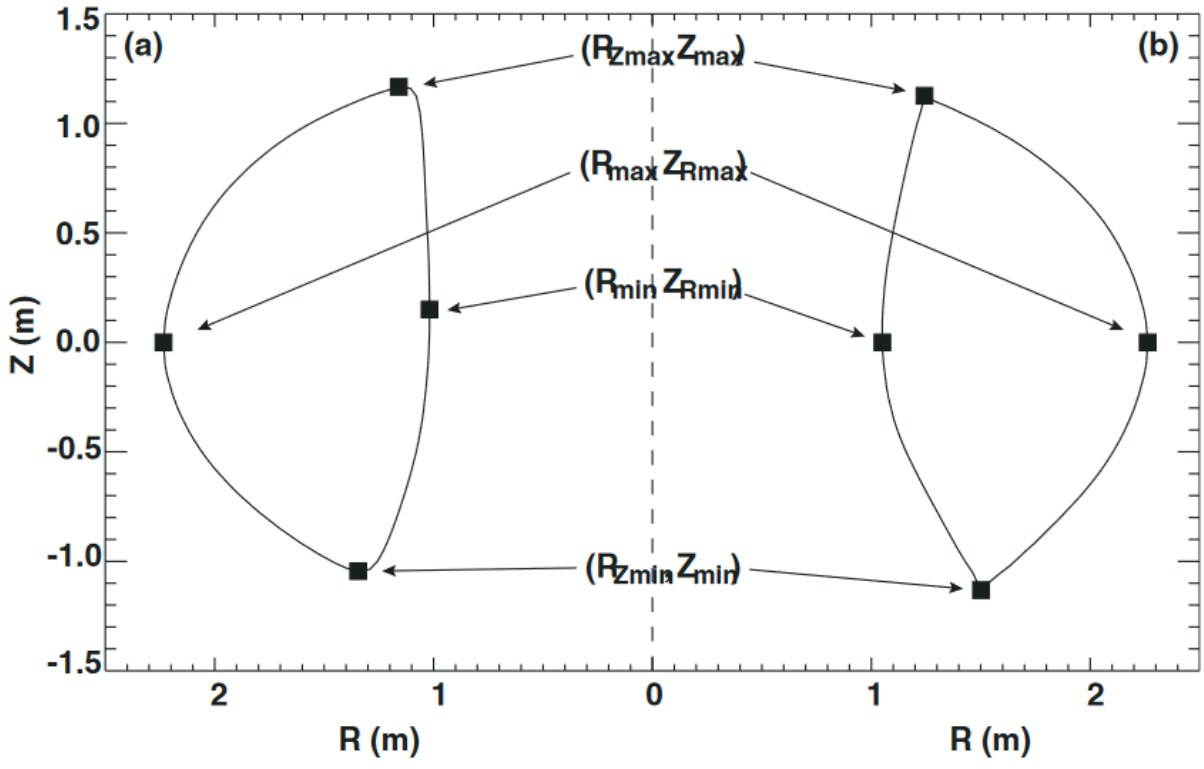

Figure 3-5: Plasma cross-section with the important points for the definition of plasma triangularity

$$\delta = \frac{\delta_{upper} + \delta_{lower}}{2} \tag{3-3}$$

$$\delta_{upper} = \frac{R_{geo} - R_{Zmax}}{a} \quad ; \quad \delta_{lower} = \frac{R_{geo} - R_{Zmin}}{a} \tag{3-4}$$

$$R_{geo} = \frac{R_{max} + R_{min}}{2} \quad ; \quad a = \frac{R_{max} - R_{min}}{2} \tag{3-5}$$

Therefore, the three cases of study, for phase 1 and phase 2, are the maximum positive triangularity case, the maximum negative triangularity case and an intermediate one which is considered the baseline case. An example of these three plasma scenarios for phase 1 is shown in Figure 3-6, representing half of the cross-section of the plasma.

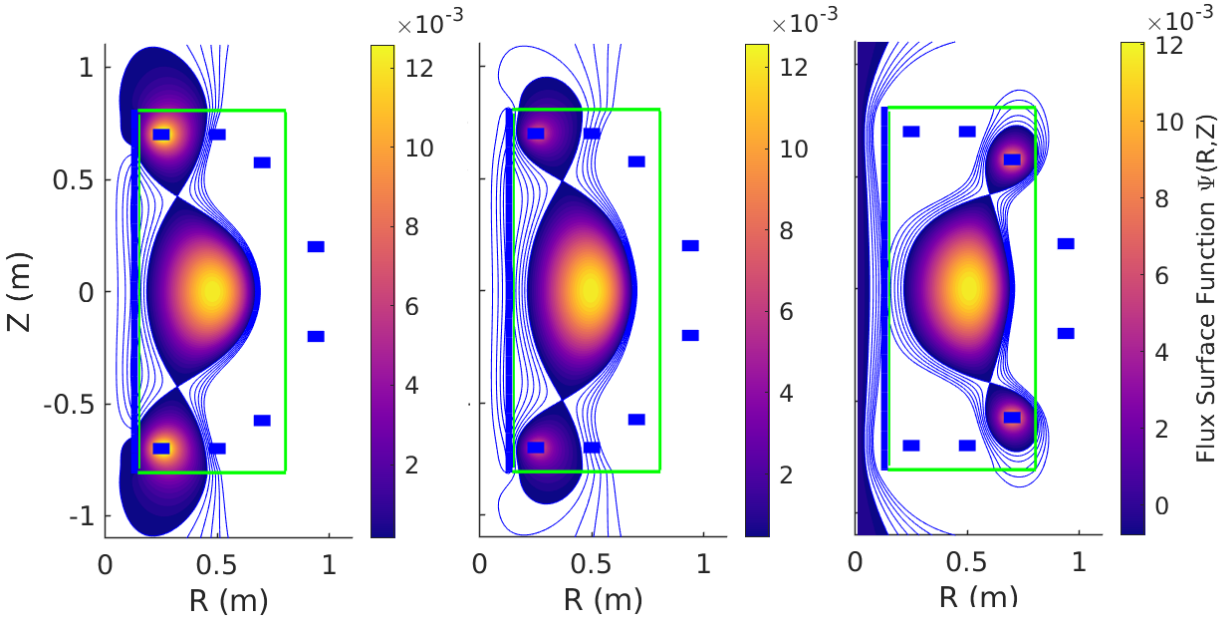

Figure 3-6: From left to right, half cross-section the plasma in SMART for maximum positive triangularity, baseline and maximum negative triangularity cases for phase 1

3.3.4 Phase 1 baseline

The baseline case is explained as an example of the current phase obtained for each of the coils of SMART. Afterwards, this case is compared with the maximum positive and negative triangularity cases and the maximum current values and slopes for the first operation of SMART are obtained.

The results for the first operation phase of SMART are considered for the power supply designed. The TFC current value is obtained from Equation (3-2), in Section 3.3.1, with the parameters of phase 1, obtaining a current of 4690A from Equation (3-6).

$$I_{TFC} = \frac{2\pi \cdot 0.45m \cdot 0.1T}{4\pi \cdot 10^{-7}T \cdot m \cdot A^{-1} \cdot 48} = 4690A \tag{3-6}$$

The current waveforms will be controlled to have a linear charging and discharging slope to minimize eddy currents in the vessel since they are directly related to the time-variation of the current. Considering a charging time of 135ms to avoid the need of higher voltages, the current waveform obtained is represented in Figure 3-7. The time is equal to zero in the moment in which the gas is ionized and the plasma is created.

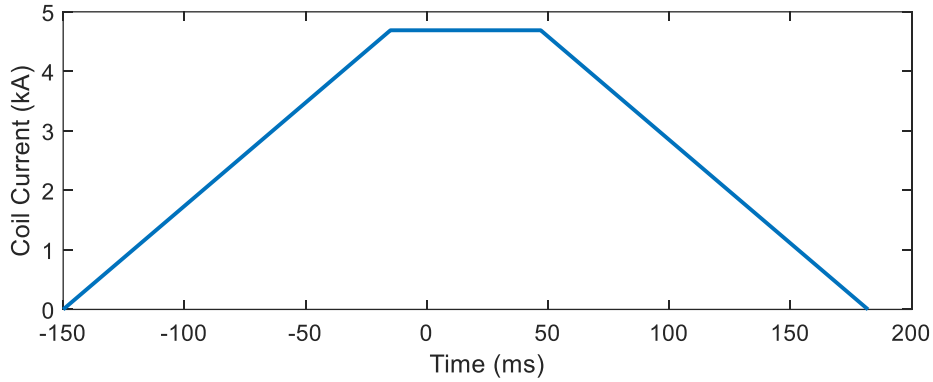

Figure 3-7: TFC current for phase

The rest of the coils current waveforms are obtained with the Fiesta code. Comparing the solenoid current waveforms, in Figure 3-8, with the plasma current, in Figure 3-9, it can be seen the function of each slope of the solenoid. The first positive ramp of the central solenoid is just for charging the coil. Then, it stays constant until the eddy currents of the vessel have decay. Afterwards, a high negative ramp is able to induce the required loop voltage to ionize the gas and achieve the breakdown of the plasma. The second negative slope maintain the growth of the plasma current up to the reference value and it is followed by a slightly positive ramp that maintains the plasma current in 30kA during 20ms. Finally, a last positive slope turns the solenoid current to zero.

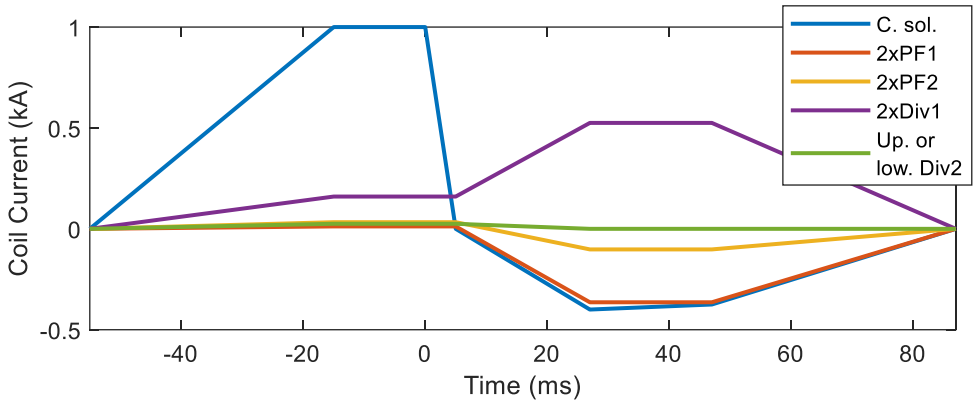

Figure 3-8: PFC and central solenoid currents for phase 1

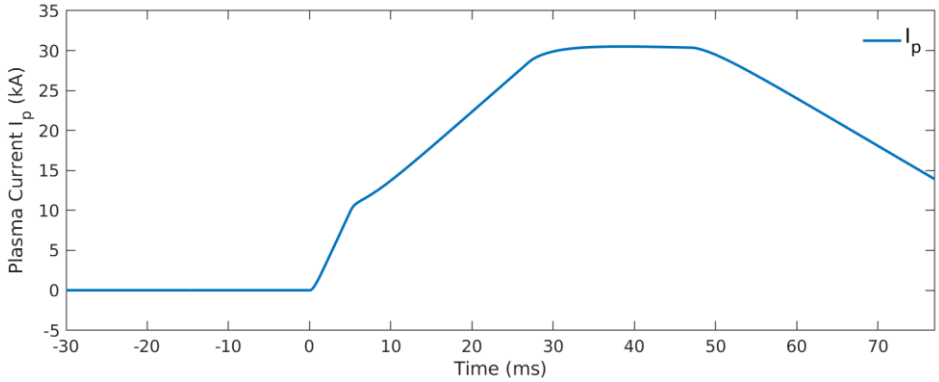

Figure 3-9: Plasma current for phase 1

Regarding the PFC, they have two main roles. First, they start constant in a null-field configuration to minimize the poloidal field to facilitate breakdown. After the breakdown is achieved, they transient up to the equilibrium configuration to shape the plasma during the flattop of the plasma current. The current required for the null-field configuration is very low. Therefore, to represent clearly all the coils current waveforms, they are also shown in Table 3-2. Upper and lower Div2 are just used for the null-field configuration but not for shaping the plasma during the equilibrium. This has been decided to try to minimize costs, so Upper and lower Div2 power supplies are more economical than the rest. The reason why it is interesting to have two independent power supplies for Div2 coils is because, during flattop, their main role is the real-time control of plasma vertical stability.

Table 3-2: Currents waveforms in phase 1

Time (ms)	12×TFC (A)	C. solenoid (A)	2×PF1 (A)	2×PF2 (A)	2×Div1 (A)	Upper or Lower Div2 (A)
-150	0	0	0	0	0	0
-55	3301	0	0	0	0	0
-15	4690	1000	12	33	160	25
0	4690	1000	12	33	160	25
5	4690	0	12	33	160	25
27	4690	-400	-364	-102	525	0
47	4690	-375	-364	-102	525	0
87	-3301	0	0	0	0	0
182	0	0	0	0	0	0

3.3.5 Operational limits for phase 1

The operational limits will consist of the maximum current value and slope that each power supply will be able to achieve. Therefore, the baseline case is compared to the maximum positive and triangularity cases to see the possible maximum values for each coil. For each of these plasma scenarios, Table 3-3 gathers the maximum current value and slope and determines the total maximum.

Table 3-3: Maximum current and slope for each plasma scenario and coil for phase 1

Coil	Plasma scenario	Max. current (A)	Max. current slope (A/ms)
12×TFC		**4690**	**31**
Central solenoid	Charging slope	**1000**	**25**
	Breakdown slope	**1000**	**200**
Central solenoid (flattop)	+ triangularity	350	16
	Baseline	400	18
	− triangularity	520	24
2×PF1	+ triangularity	321	12
	Baseline	364	17
	− triangularity	**519**	**22**
2×PF2	+ triangularity	**477**	**22**
	Baseline	102	6
	− triangularity	297	12
2×Div1	+ triangularity	1000	38
	Baseline	525	17
	− triangularity	**1500**	**75**
Upper or lower Div2	+ triangularity	**27**	**1**
	Baseline	25	1
	− triangularity	24	1

The TFC have the same current waveform in any plasma scenario. The central solenoid also has the same charging and breakdown slope in all cases and, although the flattop slopes vary, the breakdown and charging slope are predominant in all cases.

Therefore, in Table 3-4, the maximum currents and slopes for each coils are presented together with the final operational limits that will be considered for the power supply design. For the central solenoid, due to the high slope required for breakdown, two slopes will be considered for its design.

Table 3-4: Maximum currents slopes and operational limits for phase 1

Time (ms)	**12×TFC**	**C. solenoid**	**2×PF1**	**2×PF2**	**2×Div1**	**Upper or lower Div2**
Maximum current (A)	4690	1000	519	477	1500	27
Max. current slope (A/ms)	35	25	22	22	75	1
Max. breakdown current (A/ms)	–	200	–	–	–	–
Operational current (A)	6000	1500	800	800	2000	300
Op. current slope (A/ms)	50	50	50	50	100	50
Op. breakdown slope (A/ms)	–	300	–	–	–	–

3.3.6 Phase 2 baseline

As the coils have to withstand the two operation phases of SMART. The coils design is defined by the second operation phase. The baseline case of this phase is presented. The TFC current value is again calculated from Equation (3-2) of Section 3.3.1. With the parameters of phase 2, the current is obtained in Equation (3-7).

$$I_{TFC} = \frac{2\pi \cdot 0.45m \cdot 0.3T}{4\pi \cdot 10^{-7}T \cdot m \cdot A^{-1} \cdot 48} = 14063A \tag{3-7}$$

A charging and discharging time for the TFC of 135ms have been considered. Therefore, the current waveform of the TFC is shown in Figure 3-10.

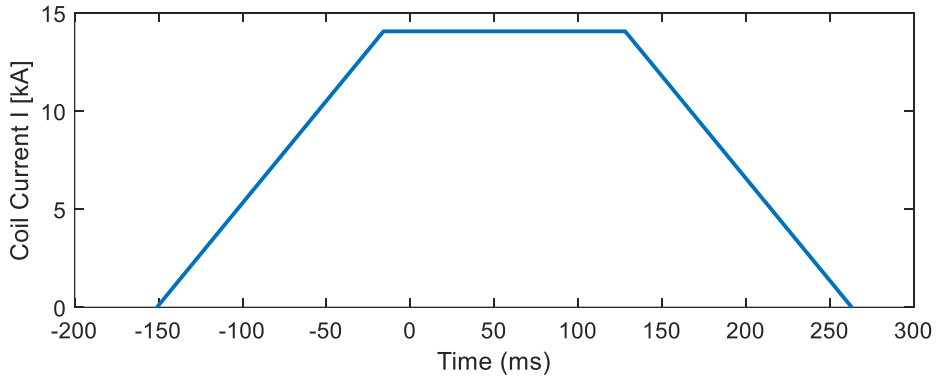

Figure 3-10: TFC current for phase 2

The rest of the current waveforms are represented in Figure 3-11 and Table 3-5. In this case, due to the longer pulse length, a third slightly negative slope is required in the central solenoid to maintain the plasma current, represented in Figure 3-12.

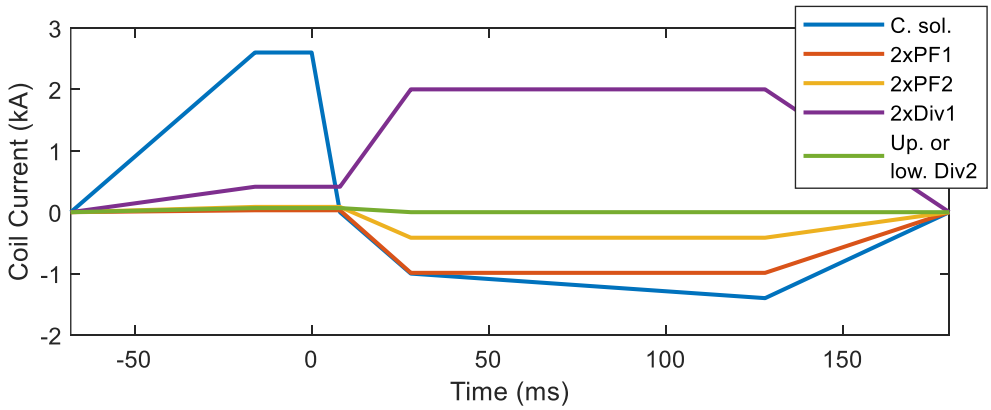

Figure 3-11: PFC and central solenoid currents for phase 2

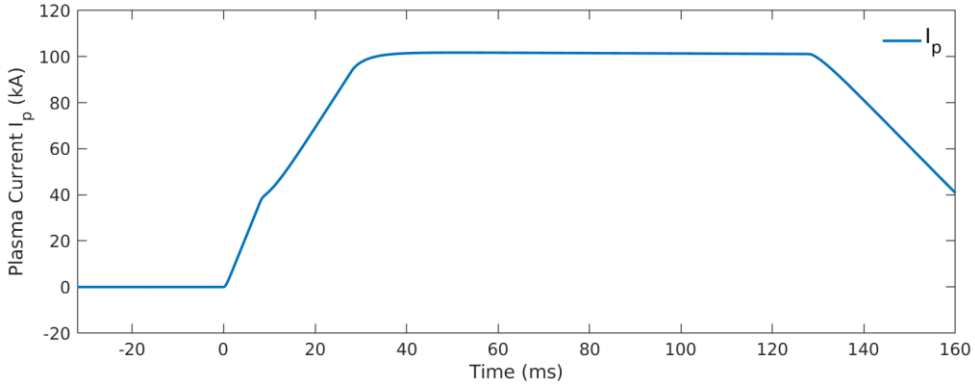

Figure 3-12: Plasma current for phase 2

Table 3-5: Currents waveforms in phase 2

Time (ms)	TFC (A)	C. solenoid (A)	PF1 (A)	PF2 (A)	Div1 (A)	Div2 (A)
-151	0	0	0	0	0	0
-68	8646	0	0	0	0	0
-16	14063	2600	31	86	414	67
0	14063	2600	31	86	414	67
8	14063	0	31	86	414	67
28	14063	-1000	-988	-416	2000	0
128	14063	-1400	-988	-416	2000	0
180	-8646	0	0	0	0	0
263	0	0	0	0	0	0

3.3.7 Operational limits for phase 2

Once again, apart from the baseline case, the maximum positive and negative triangularity cases have been studied to obtain the maximum current values and slopes for this phase. The results for each case and for each coil is presented in Table 3-6.

Table 3-6: Maximum current and slope for each plasma scenario and coil for phase 2

Coil	Plasma scenario	Max. current (A)	Max. current slope (A/ms)
TFC		**14063**	**56**
Central solenoid	Charging slope	**2600**	**50**
	Breakdown slope	**2600**	**325**
Central solenoid (flattop)	+ triangularity	1100	50
	Baseline	1400	50
	− triangularity	2200	50
PF1	+ triangularity	826	33
	Baseline	988	51
	− triangularity	**1421**	**69**
PF2	+ triangularity	**1550**	**77**
	Baseline	416	25
	− triangularity	696	40
Div1	+ triangularity	3500	154
	Baseline	2000	79
	− triangularity	**3500**	**196**
Div2	+ triangularity	**72**	**4**
	Baseline	67	3
	− triangularity	64	3

The maximum currents and slope results, together with the operational limits of phase 2 are shown in Table 3-7.

Table 3-7: Maximum currents slopes and operational limits for phase 2

Time (ms)	TFC	C. solenoid	PF1	PF2	Div1	Div2
Maximum current (A)	14063	2600	1421	1550	3500	72
Max. current slope (A/ms)	104	50	69	77	196	4
Max. breakdown current (A/ms)	–	325	–	–	–	–
Maximum coil current (A)	20000	5000	5000	5000	5000	5000
Operational current (A)	17000	4000	3000	3000	4500	300
Op. current slope (A/ms)	150	100	150	150	300	50
Op. breakdown slope (A/ms)	–	400	–	–	–	–

The operational limits of phase 2 will be useful for the future design of the power supply for phase 2. However, in this document the design of this power supply is not presented. This phase is important at this initial point for the coils design. Therefore, a maximum coil current has been defined. It is higher or equal than the operational limit in order to leave enough margin for studies of new plasma scenarios and configurations.

3.4 Magnetic pressure of the coils

For a first evaluation of the magnetic forces that have to withstand the coils, the magnetic pressure due to the own magnetic field is going to be evaluated. Soft tempered copper has a yield strength higher than 35MPa [28], but there are copper alloys that withstand up to 270MPa, as the case of the one used in Globus-M [15].

The magnetic pressure of a coil can be obtained with Equation (3-8). For the magnetic field induced by the central solenoid and the PFC, Equation (3-9) is used. Table 3-8 shows the magnetic field in the centre of each coils and magnetic pressure for each coil, which is much lower than the yield strength. Future studies will be carried out to evaluate the magnetic forces between coils.

$$P_B = \frac{B^2}{2 \cdot \mu_0} \tag{3-8}$$

$$B = \frac{\mu_0 \cdot N \cdot I}{H} \tag{3-9}$$

Table 3-8: Magnetic pressure stand by each coil

Parameter	TFC	C. solenoid	PF1	PF2	Div1	Div2
Mag. Field (T)	0.3	0.835	0.003	0.003	0.003	0.003
Mag. pressure (MPa)	0.04	1.76	0.00	0.00	0.00	0.00

4 COILS DESIGN

SMART, as a tokamak, requires three group of coils. It is necessary to point out that the different operation phases of the machine should imply minimum modifications of the tokamak in each phase. Therefore, the coils design presented in this document covers phases 1 and 2 with a single design. The operational limits for phase 2, obtained in Chapter 3, are considered as the rated values for the coils. Together with the geometry restrictions of the vessel, the coils geometry and their electrical parameters are defined. Finally, with the obtained resistance and inductance, the rated voltage of each coil is determined.

4.1 Estimation of coils cross sections

In order to estimate the cross-section of each coil to obtain the final coils geometries, a simple analytical thermal model is explained to obtain the copper cross-section and the insulation thickness is defined considering the insulation used in other similar devices.

4.1.1 Copper cross section: thermal model

In order to obtain the required cross section for the coils, a simple analytical thermal model have been considered to estimate the temperature increases during a discharge [29]. The conductor releases a power due to Joule effect that is equal to:

$$\frac{dE}{dt} = R \cdot i^2 \tag{4-1}$$

The instant current in the conductor is i and the resistance is R. This resistance depends on the temperature of the conductor. Considering R_{20} the resistance at 20ºC, T the temperature of the conductor and α the temperature coefficient of the conductor at 20ºC, the resistance is equal to:

$$R = R_{20} \cdot (1 + \alpha \cdot (T - 20\ ºC)) \tag{4-2}$$

The heat transferred to the copper depends on the mass m of the material, the specific heat C_e of the conductor; which, in this range of temperature, will be considered constant; and the derivative of the temperature:

$$\frac{dQ}{dt} = m \cdot C_e \cdot \frac{dT}{dt} \tag{4-3}$$

If the dissipation process is considered very fast and, conservatively, there is no heat transfer with the exterior, Equation (4-1) and Equation (4-3) are equal:

$$\frac{dE}{dt} = \frac{dQ}{dt} \quad \rightarrow \quad R_{20} \cdot \left(1 + \alpha \cdot (T - 20\ ºC)\right) \cdot i^2 = m \cdot C_e \cdot dT \tag{4-4}$$

Taking into account that R_{20} depends on the resistivity at 20ºC ρ_{20}, the length of the conductor l, and the cross-section S, and that de mass of the copper is the density D times the cross-section times the length:

$$R_{20} = \rho_{20} \cdot \frac{l}{S} \tag{4-5}$$

$$m = D \cdot S \cdot l \tag{4-6}$$

The expression obtained is:

$$\frac{1}{S^2} \cdot i^2 \cdot dt = \frac{D}{\rho_{20}} \cdot C_e \cdot \frac{dT}{1 + \alpha \cdot (T - 20\,ºC)} \tag{4-7}$$

If both terms are integrated and the first term is multiplied and divided by the interval of time:

$$\frac{(t_f - t_i)}{S^2} \cdot \left(\frac{1}{(t_f - t_i)} \cdot \int_{t_i}^{t_f} \cdot i^2 \cdot di \right) = \int_{T_i}^{T_f} \frac{D}{\rho_{20}} \cdot C_e \cdot \frac{dT}{1 + \alpha \cdot (T - 20\,ºC)} \tag{4-8}$$

The term in brackets is the root mean square value squared of the current. Solving the integral of the second term, the expression obtained is:

$$\frac{t_f - t_i}{S^2} \cdot I_{rms}^2 = \frac{D \cdot C_e}{\rho_{20} \cdot \alpha} \cdot ln\left(1 + \frac{T_f - T_i}{\frac{1}{\alpha} + 20\,ºC + T_i} \right) \tag{4-9}$$

Therefore, the final expression of the thermal model is:

$$S = \frac{\sqrt{t_f - t_i}}{k(T_i, T_f)} \cdot I_{rms} \quad with \quad k = \sqrt{\frac{D \cdot C_e}{\rho_{20} \cdot \alpha} \cdot ln\left(1 + \frac{T_f - T_i}{\frac{1}{\alpha} - 20\,ºC + T_i} \right)} \tag{4-10}$$

The parameters for the obtention of the factor k in the case of copper conductors are shown on Table 4-1.

Table 4-1: Parameters of the thermal model

Parameter	Value
D (g/cm^3)	8.9
C_e (J/(g·ºC))	0.385
ρ_{20} (Ω·m/mm^2)	0.0171
α (1/ºC)	$3.9 \cdot 10^{-3}$

4.1.1 Total cross section: insulation

In addition to the copper, the cross-section will be increased due to the minimum distances required for the insulation, which is a combination of epoxy resin and fibreglass like in other tokamaks [15][30]. The dielectric strength ε of glass-reinforced epoxy resin is higher than 15 kV/mm [31]. In addition, it would be assumed a maximum voltage difference between each coil V_{max} of 3 kV. Therefore, the minimum width of the insulation is 0.2mm. As is shown in Equation (4-11).

$$W_{epoxy} = 1.25mm \geq \frac{V_{max}}{\varepsilon} = 0.2\ mm \tag{4-11}$$

However, after the search of the insulation used in other similar tokamaks, all of them are using an insulation thickness from turn to turn of around 2.5 mm. In order to have a conservative estimation of the insulation width W_{epoxy}, it has been chosen 1.25 mm as insulation thickness.

4.2 Central stack optimization

The central stack is the main part of the design of a spherical tokamak and consists of the central solenoid and the inner legs of the TFC. As spherical tokamak needs an Aspect Ratio lower than 2, for SMART this implies a diameter for the central stack of 300 mm. The height of the central stack is 1.6m as the height of the Vacuum Vessel. A cross-section of the central stack es represented in Figure 4-1.

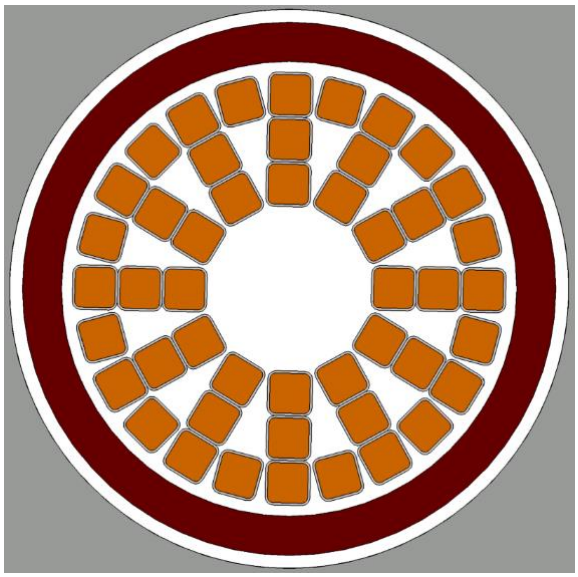

Figure 4-1: Central stack cross-section. The TFC are in the inner side and the central solenoid in the outer side

The choice of the best configuration is a compromise between electrical performances and easiness during the assembly of the machine. Having the solenoid outside could complicate the assembly but it allows reducing the current needs as the solenoid radius is larger.

Furthermore, it is important to preserve enough space between the inner vessel wall and the central solenoid because it is required for future extractions of the central column. The triangular free spaces between the TFC are intended to be used for cooling.

The cooling system is not required for Phase 1, but an air forced o liquid cooling system are considered for Phase 2 and a possible extension of this phase. The central solenoid is made of a hollow conductor to allow the future use of a water-cooling system.

To reduce costs, a square cross-section is employed for the TFC. With 48 turns, the distribution of the inner legs done in Figure 4-1 have been chosen to maximize the occupied space. The main idea for the design of the central stack is to optimize the space required for the TFC and the central solenoid.

Therefore, the thermal model considers that the temperature increase in both coils is equal, starting at 25ºC, and each of them maintains constantly their maximum coil current. However, in order to take into account that the TFC operates during a longer time than the central solenoid, the time this current is maintained is equal to the full operational time length of each coil current waveform shown in Section 3.3.6. The parameters are presented in Table 4-2.

Table 4-2: Thermal model input parameters for the central stack design

Coil	$I_{rms}=I_{max}$ (kA)	t_1-t_0 (ms)	T_0 (ºC)
TFC inner legs	20	414	25ºC
Central solenoid	5	248	25ºC

An iterative process is done to obtain the final design values presented in Table 4-3. A rounding radius of 2mm for the TFC have been considered. For the central solenoid cross-section a commercial conductor from Luvata have been selected [28].

Table 4-3: Final temperature an cross-sections for the central stack

Coils	T_f (ºC)	S (mm^2)	Dimensions (mm×mm)	Rounding radius (mm)	Cooling diameter (mm)
TFC inner legs	30	89.5	21.5×21.5	3	–
Central Solenoid	30	445	8×12.5	1	3.5

With these cross-sections and a solenoid of two layers, the optimization of the central stack is achieved with a space between the solenoid and the vacuum vessel of 10mm, and between the solenoid and the TFC of 5mm. The temperature increase is just of 5ºC in phase 2, what allows a future study of an extended phase 2.

4.3 Solenoid design

The central solenoid will consist of 2 layers of 105 turn each, as it is represented in Figure 4-2. With the obtained cross-section in Section 4.2 and the geometry of the coils we can estimate its resistance and inductance from Equation (4-12) and Equation (4-13) respectively. The inductance is obtained with the expression of an ideal long solenoid. The radius of the central solenoid is r, N is the total number of turns and H the height of coil. The final results, together with the main geometry parameters, are shown in Table 4-4.

Figure 4-2: Section of the central solenoid.

$$R = \rho_{20} \cdot \frac{2\pi \cdot r \cdot N}{S} \tag{4-12}$$

$$L = \mu_0 \cdot \frac{\pi \cdot r^2 \cdot N^2}{H} \tag{4-13}$$

Table 4-4: Main parameters of the central solenoid

Parameter	Central solenoid
Height (m)	1.6
2-layers width (mm)	21
Radius (mm)	132.5
Number of turns	210
Resistance (mΩ)	33.4
Inductance (mH)	1.93

4.4 TFC design

The inner legs TFC cross-section has been obtained in Section 4.4, but the outer limbs cross-sections have to be obtained. Figure 4-3 represents one rectangular TFC. The outer limbs do not have any space restriction and they are not be equipped with a cooling system. Therefore, it is considered a temperature increase lower than 1ºC to obtain the cross-section and they are distributed in a 2×2 configuration. The cross-section is represented in Figure 4-4 and its parameters are shown in Table 4-5.

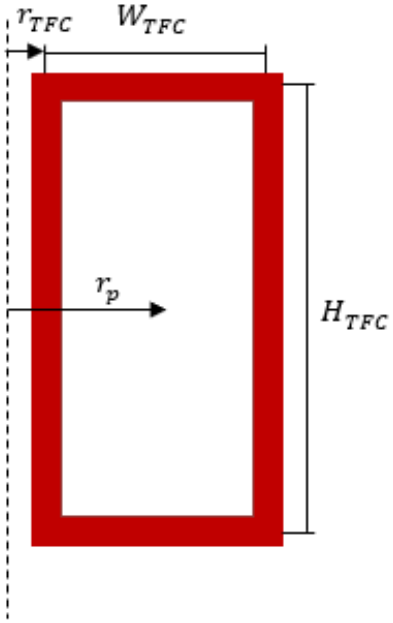

Figure 4-3: One TFC simplified scheme with its main dimensions.

Table 4-5: Thermal model and cross-section parameters for the TFC outer limbs

Coils	$I_{rms}=I_{max}$ (kA)	t_1-t_0 (ms)	T_0 (ºC)	T_f (ºC)	S (mm^2)	Dimensions (mm×mm)	Rounding radius (mm)
TFC outer limbs	20	414	25	<26	1292	36×36	2

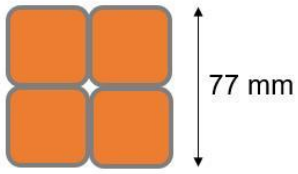

Figure 4-4: Conductors configuration for the TFC outer limbs.

The TFC consist of 12 coils of 4 turns each. Each of them is a rectangular coil with one of the long sides as inner leg and the other three sides as the outer limb. The total resistance and inductance are obtained from Equation (4-14) and Equation (4-15). H_{TFC}, W_{TFC} and r_{TFC} are the height, width and internal mean radius of the TFC, respectively. The main parameters are shown in Table 4-6.

$$R = \rho_{20} \cdot N \cdot \left(\frac{H_{TFC}}{S_{inner}} + \frac{(2 \cdot W_{TFC} + H_{TFC})}{S_{outer}} \right) \quad (4\text{-}14)$$

$$L = \mu_0 \cdot \frac{H_{TFC} \cdot N^2}{2\pi} \cdot ln\left(\frac{r_{TFC} + W_{TFC}}{r_{TFC}} \right) \quad (4\text{-}15)$$

Table 4-6: Main parameters of the TFC

Parameter	TFC (one coil)
Height (m)	2
Width (mm)	919
Internal mean radius (mm)	81
Parameter	**12×TFC**
Number of turns	48
Resistance (mΩ)	6.13
Inductance (mH)	2.32

4.5 PFC design

The PFC are made of hollow conductors to allow the future use of a cooling system, shown in Figure 4-5. Therefore, to make them coherent with the central stack design, the temperature increase considered is equal, obtaining the cross-section of Table 4-7. A commercial conductor of Luvata have been selected [28].

Table 4-7: Thermal model and cross-section parameters for the PFC

Coils	$I_{rms}=I_{max}$ (kA)	t_1-t_0 (ms)	T_0 (ºC)	T_f (ºC)	S (mm^2)	Dimensions (mm×mm)	Rounding radius (mm)	Cooling diameter (mm)
PFC	5	248	25	30	85	10×10	1	4

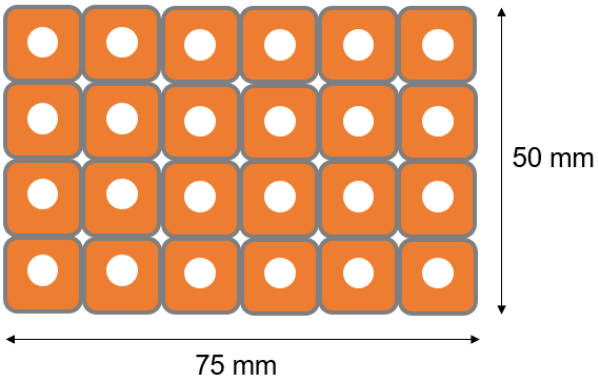

Figure 4-5: PFC Configuration

Each coil has 24 turns. The conductors will be placed in a 6×4 configuration. The resistance and inductance is obtained from Equation (4-16) and Equation (4-17). The inductance is obtained with the ideal long solenoid expression multiplied by a correcting factor obtained in Equation (4-18) for short coils, the Nagaoka coefficient. The main parameters are shown in Table 4-8.

$$R = \rho_{20} \cdot \frac{2\pi \cdot r_{PFC} \cdot N}{S_{copper}} \tag{4-16}$$

$$L = k_N \cdot \mu_0 \cdot \frac{\pi \cdot r_{PFC}^2 \cdot N^2}{H_{PFC}} \tag{4-17}$$

$$k_N = \frac{2}{\pi} \cdot \frac{H_{PFC}}{2 \cdot R_{PFC}} * \left(\ln\left(\frac{8}{\pi} + 4 \cdot \left(\frac{2 \cdot R_{PFC}}{H_{PFC}} \right) \right) - \frac{1}{2} \right) \tag{4-18}$$

Table 4-8: Main parameters of each individual PFC

Parameter	PF1 (one coil)	PF2 (one coil)	Div1 (one coil)	Div2 (one coil)
Height (mm)	50	50	50	50
Width (mm)	75	75	75	75
Radius (mm)	940	700	250	500
Number of turns	24	24	24	24
Parameter	**2×PF1**	**2×PF2**	**2×Div1**	**Div2 (one coil)**
Resistance (mΩ)	56.0	41.6	14.88	14.9
Inductance (mH)	6.16	4.30	1.18	1.42

4.6 Rated voltage definition

Although the insulation thickness has been highly overestimated to have similar values than other devices, it is going to be assure a rated voltage for each of the coils. Considering the maximum coils currents and the operational slopes for phase 2 obtained in Section 3.3.7, the voltage stand by each coil is obtained with Equation (4-19). The voltage withstood and the rated voltage considered in the design are presented in Table 4-9.

$$V = L \cdot \left(\frac{di}{dt}\right)_{max} + R \cdot I_{max} \tag{4-19}$$

Table 4-9: Maximum voltage stand by each coil

Parameter	12×TFC	C. solenoid	2×PF1	2×PF2	2×Div1	Div2 (one coil)
Voltage withstood (V)	470	941	1204	854	428	145
Rated voltage (V)	1000	2000	2000	2000	1000	1000

The complete design of the coils has been defined with enough margin to guarantee a robust and flexible system. The electrical parameters of the coils will allow the design and simulation of the power supplies to assure the correct operation of the system.

5 POWER SUPPLY DESIGN

Once the operational limits for phase 1 have been defined in Section 3.3.5 and the electrical parameters of the coils were obtained in Chapter 4, the power supply for each coil is designed. Starting from a power supply baseline and explaining the main elements of the power supply, the topology and specifications for each group of coils power supplies are described and the simulation results are presented, proving their feasibility.

5.1 Power supply baseline

The power supply system is based on 7 independently controlled power supplies, as it was presented in Section 3.1. The TFC are represented as the equivalent inductance of the series connection of the 12 coils, as well as the PF1, PF2 and Div1coils are represented as the equivalent of the series connection of the upper and lower coils. The system represented in Figure 5-1 has been considered as a starting baseline and it has been modified up to final design.

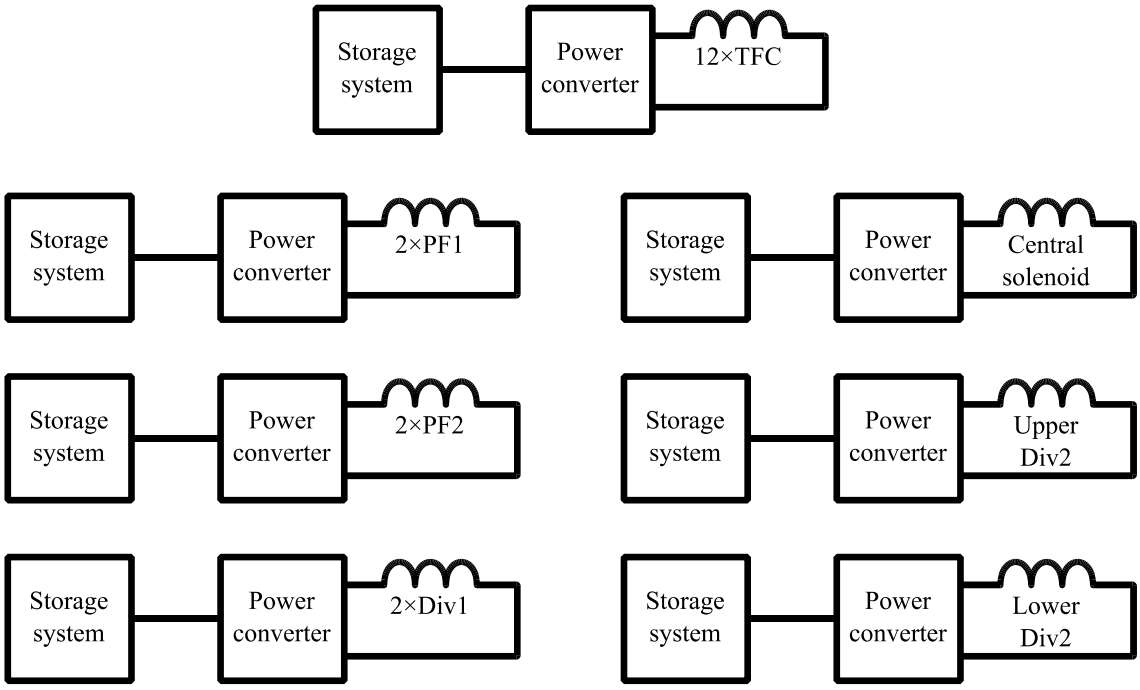

Figure 5-1: Power supply baseline distribution for SMART. Slight modifications are done after the final design of the system

Moving to the detailed design of each power supply baseline, each of them is based in the OCEM power supply for PROTO-SPHERA and is also similar to the PFC power supply from VEST, explained in Chapter 2. The power supply is represented in Figure 5-2, the coil is fed by a supercapacitor bank (SB), of which current is controlled by a H-bridge converter, switching at high frequency. The LC filter protects the supercapacitors from the ripple caused by the converter.

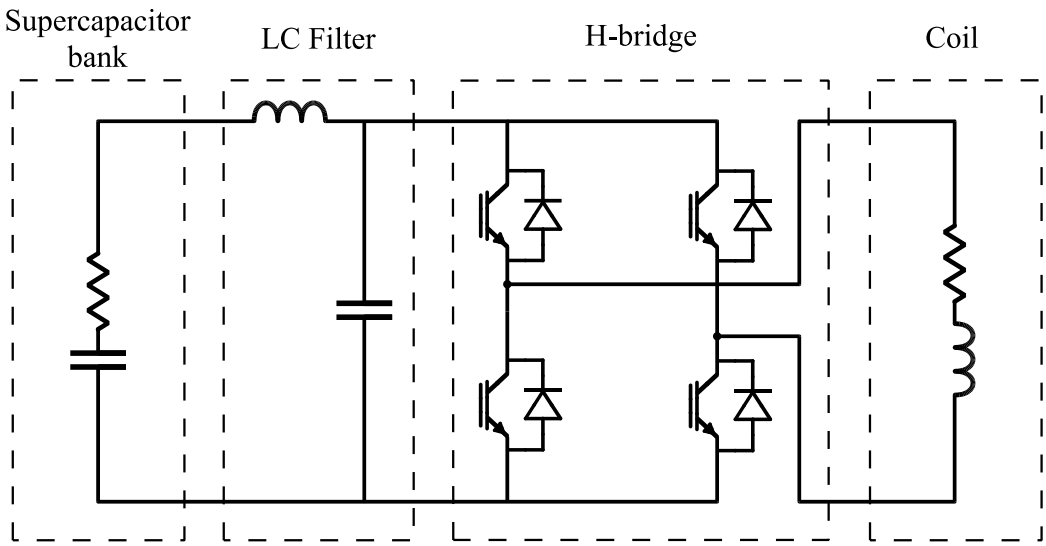

Figure 5-2: Power supply baseline for each coil

5.1.1 H-bridge as power converter

A commercial power converter is considered for all the power supplies in order to achieve a realistic design. After an exhaustive search, the IFF2400P17LE440988 converter from Infineon [32] have been chosen. Its main specifications are shown in Table 5-1.

Table 5-1: Infineon converter specifications

Parameter	Value
Integrated chip voltage (V)	1700
Integrated chip current (A)	2400
Typical higher output voltage (V_{RMS})	690
Rated output current (A_{RMS})	1550

The topology of the converter consists of four independent branches of two IGBT each, as it is shown in Figure 5-3. They can be connected in pairs to have two independent H-bridges. The main idea of choosing these commercial components is to have an idea of the main limitations of each technology.

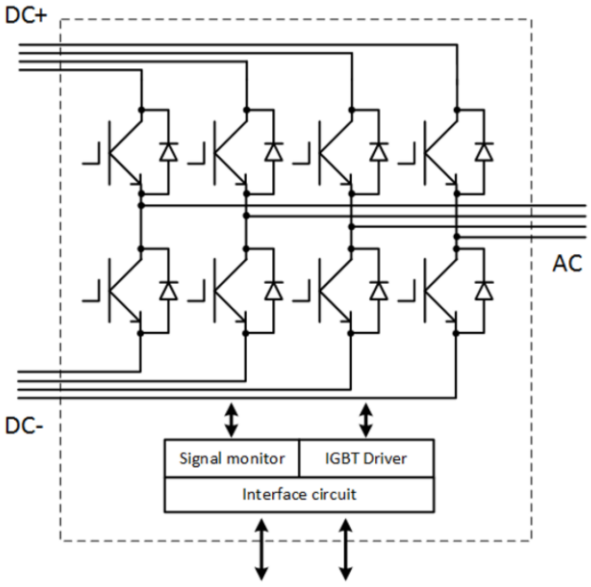

Figure 5-3: Topology of the Infineon converter, reprinted from [32]

In next sections, it is going to be seen that the voltage of the power converter is not a limiting factor. However, the operational current for TFC and Div1, obtained in Section 3.3.5, surpass the rated output current of the converter. This rated current has been defined for a continuous AC application and our system have a DC output.

Nevertheless, the operation time is really short so it can be considered a pulsed application. Therefore, the maximum limiting current would be between the 2.4kA of the integrate chip current and the 1.55kA of the rated output current. For this first design, the conservative limit of 1.55kA has been set, together with a switching frequency of 1kHz. This limit will be updated after a future thermal study of the converter.

5.1.2 Supercapacitors bank as storage system

The storage system is based on a supercapacitors bank (SB). The SB consists of commercial supercapacitors modules (SM) from SHAMWA, the DM04860888W0101 module [24]. Its main specifications are presented in Table 5-2. The maximum peak current is 2025A. Therefore, considering the limiting 1.55kA current of the power converter in Section 5.1.1, the SB will consist just of SM connected in series in order to increases the voltage as is represented in Figure 5-3. The number of SM in series is selected in order to have enough voltage margin for moments where the load is discharging, and the SB is charging, and also to have a duty cycle for the PWM lower than 0.9.

Table 5-2: SHAMWA SM specifications

Parameter	Value
Rated voltage (V)	48.6
Capacitance (F)	166.6
ESR DC (mΩ)	6
Maximum peak current (A)	2025
Maximum stored energy (Wh)	54.68
Dimensions (mm)	418×191×179

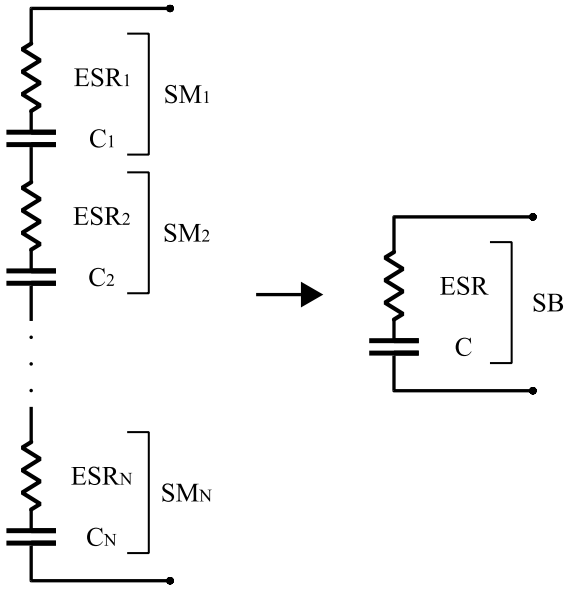

Figure 5-4: The SB consist of the series connection of N SM

5.1.3 LC filter

A significant temperature increase can produce damages in the SM [23]. For a first estimation of the LC filter, the cutoff frequency f_c is defined as half of the switching frequency until a future study obtain the proper dimensions to avoid a high temperature increase in the SB. The filter is defined with Equation (5-1), depending on the cutoff frequency and the resistance of the coil R_{coil}. With this design, the current ripple of the supercapacitors is maintained lower than 2% with respect to the maximum peak current.

$$L = \frac{\sqrt{2} \cdot R_{coil}}{2\pi \cdot f_c} \quad ; \quad C = \frac{\sqrt{2}}{2\pi \cdot f_c \cdot R_{coil}} \tag{5-1}$$

Between the H-bridge converter output and the load there is no filter in order to reduce costs. Furthermore, as it is shown in the following sections, thanks to the inductance of the load, the ripple obtained is always lower than 1% of the rated current, more than enough for this application.

5.1.4 Control strategy

In order to operate the H-bridge converters, a simple feedback control is implemented based on a PI controller comparing the current with its reference, as it is represented in Figure 5-5. The result is the voltage reference that is used by a Unipolar Pulse Width Modulation (PWM) module to obtain the switching signal for each IGBT.

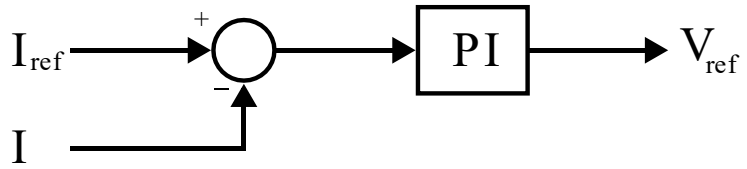

Figure 5-5: Control topology for the power supplies

The integral and proportional components of the PI controller are calculated from Equation (5-2), with a constant time τ_{cl} in order to achieve the reference in 5ms.

$$P = \frac{L_{coil}}{\tau_{cl}} \quad ; \quad I = \frac{R_{coil}}{\tau_{cl}} \quad ; \quad \tau_{cl} = 0.63 \cdot 0.5ms \tag{5-2}$$

For the power supplies where parallelisation is required, the control topology is shown in Figure 5-6. The reference voltage for each H-bridge is obtained by the sum of PI output of the total current and PI output of the specific current of the H-bridge.

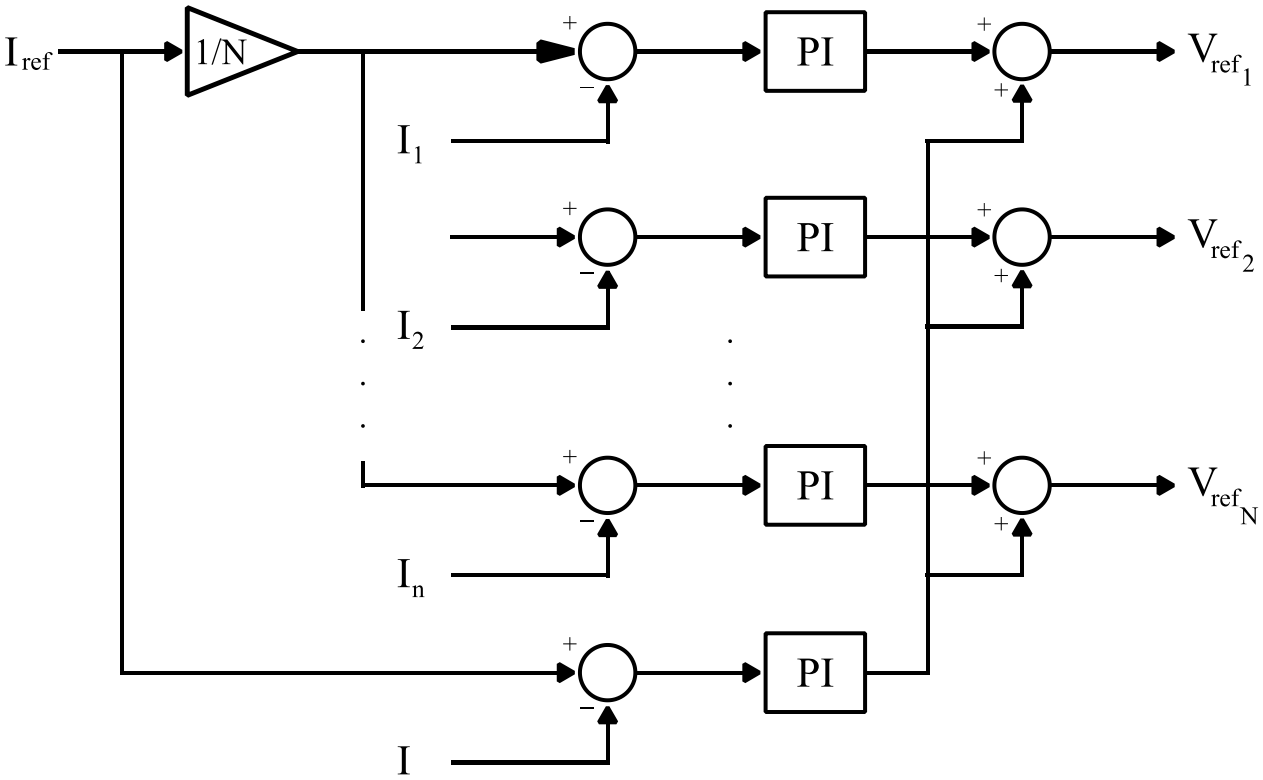

Figure 5-6: Control topology for a power supply with N H-bridges in parallel

5.2 PFC power supply

Some modifications are done to the baseline power supply in order to keep to the technical restrictions of the power converter and to reduce costs. The topology for each of the PFC is described and the systems are tested in MATLAB Simulink, explaining the results obtained. A generic reference current for the simulations is shown in Figure 5-7, where the rated current and slope of the power supply are equal to the operational limits for phase 1 obtained in Section 3.3.5.

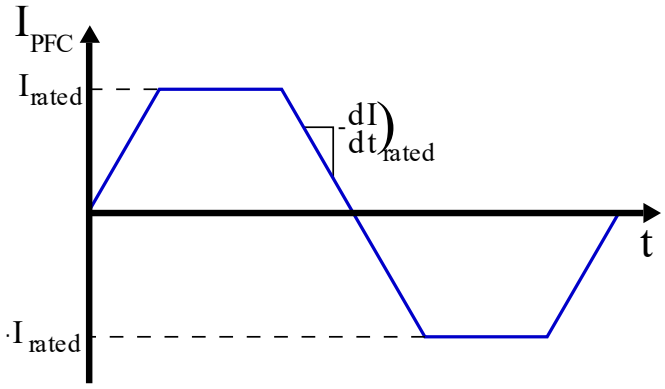

Figure 5-7: Reference current used for PFC power supplies simulations

5.2.1 PF1 and PF2 power supply topology

Considering the operational limits obtained in Table 3-4 of Section 3.3.5, PF1 and PF2 only need one H-bridge each, as their operational current limit is lower than the 1.55kA restriction of the converter shown in Section 5.1.1. However, as their operational limit is even lower than 1kA and they have similar resistance and inductance, they can share the same SB to reduce the costs, saving one SB. The SB will just consist of several modules in series up to the required voltage. Therefore, PF1 and PF2 power supply has the topology represented in Figure 5-8 and with the specifications of Table 5-3.

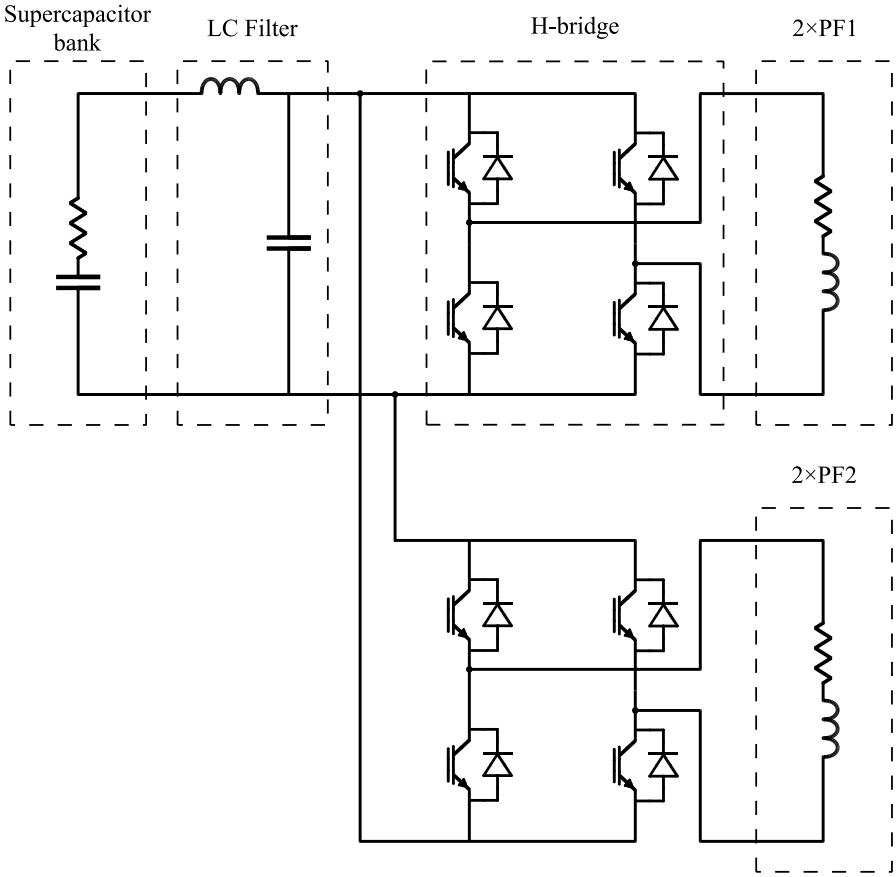

Figure 5-8: PF1 and PF2 power supply topology

Table 5-3: PF1 and PF2 power supply specifications

Parameter	2×PF1/2×PF2
Nº of SB and filters	1
Nº of H-bridges	2
SM in series	13
Rated current (A)	800
Rated voltage (V)	631.8
SB current ripple (%)	1.60
Load current ripple (%)	0.43/0.49
Filter L (μH)	25.2
Filter C (mF)	8.11

5.2.2 Div1 power supply topology

For Div1, the operational limit is higher than 1.55kA. Therefore, it requires the parallelization of the power supply, as shows Figure 5-9. To avoid short-circuits between the converters, a sharing inductor is placed at the output of each H-bridge [33]. The inductor has to achieve a compromise to able the parallel operation without slowing too much the dynamic of the system. It could be considered as a MMC as the ASDEX Upgrade prototype power supply in Section 2.5.1, but with an H-bridge as a cell instead of a half-bridges. The specifications of the power supply are presented in Table 5-4.

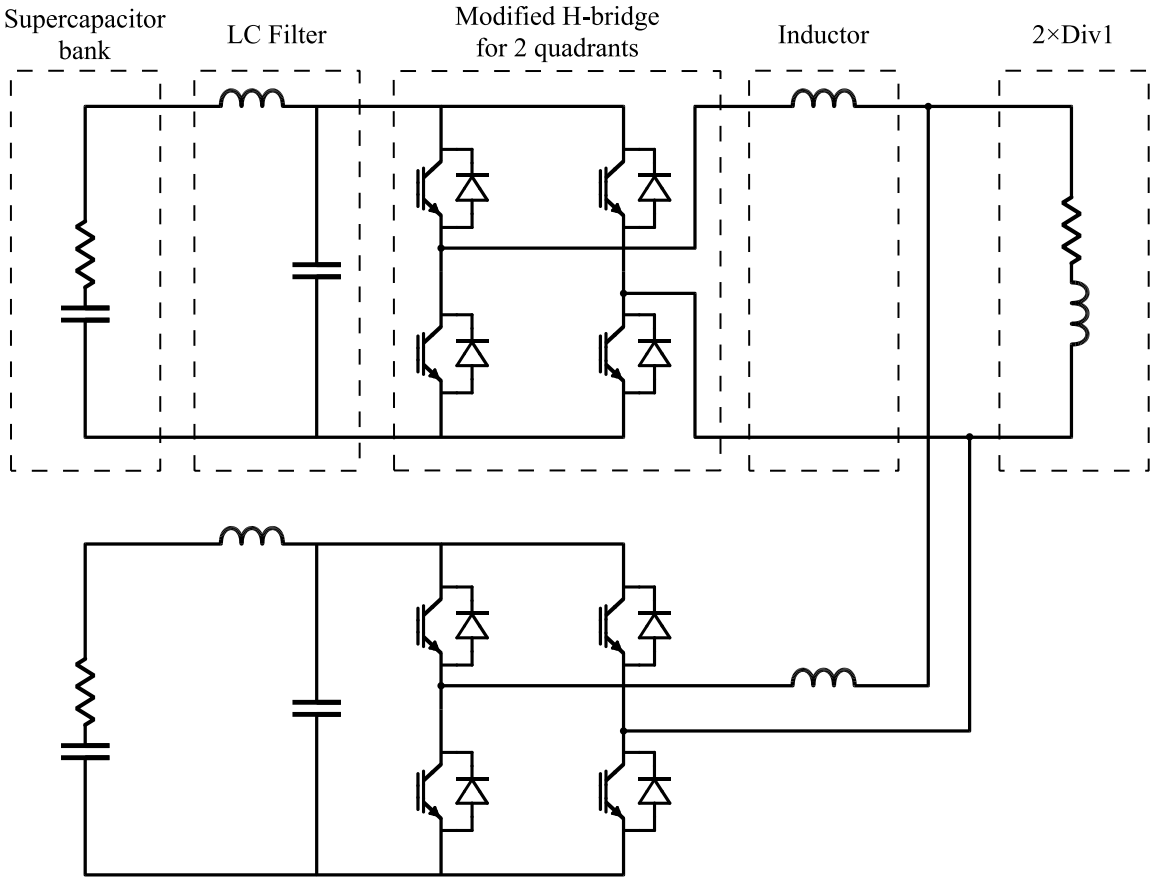

Figure 5-9: Div1 power supply topology

Table 5-4: Div1 power supply specifications

Parameter	2×Div1
Nº of SB and filters	2
Nº of H-bridges	2
SM in series	7
Rated current (A)	2000
Rated voltage (V)	340.2
SB current ripple (%)	0.72
Load current ripple (%)	0.42
Filter L (μH)	6.7
Filter C (mF)	30.2
Sharing inductor (mH)	1

5.2.1 Upper and Lower Div2 power supply topology

For Div2 coils, there are two independent converters for the upper and lower coils in order to be more flexible to control the vertical stability of the plasma by real-time control. However, as in the case of PF1 and PF2, due to the low requirement of the coils, they both share the same SB. The power supply topology is shown in Figure 5-10 and its specification in Table 5-5.

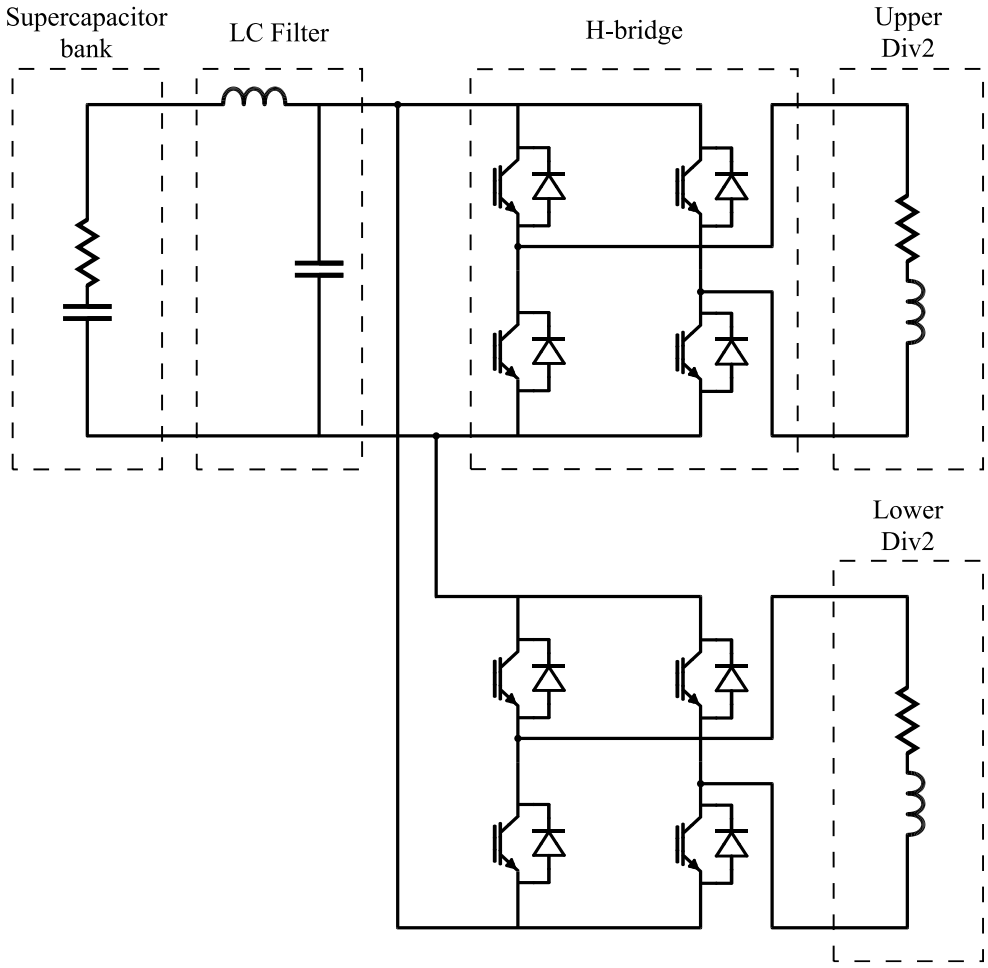

Figure 5-10: Upper and lower Div2 power supply topology

Table 5-5: Upper and Lower Div2 power supply specifications

Parameter	Upper Div2 / Lower Div2
Nº of SB and filters	1
Nº of H-bridges	2
SM in series	4
Rated current (A)	300
Rated voltage (V)	194.4
SB current ripple (%)	0.22
Load current ripple (%)	0.57
Filter L (µH)	6.7
Filter C (mF)	30.2

5.2.2 PF1 and PF2 simulation results

The system is simulated in MATLAB Simulink, obtaining the following results. In Figure 5-11, it can be seen how the PF1 power supply matches closely the reference, which reaches the operational limits for current value and slope. The current ripple, shown in Figure 5-12, is 0.43% of the rated current.

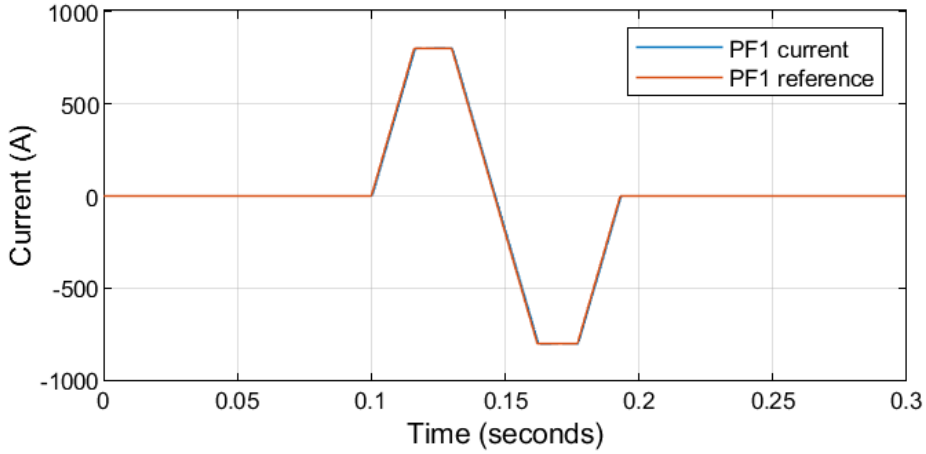

Figure 5-11: PF1 current compare to reference

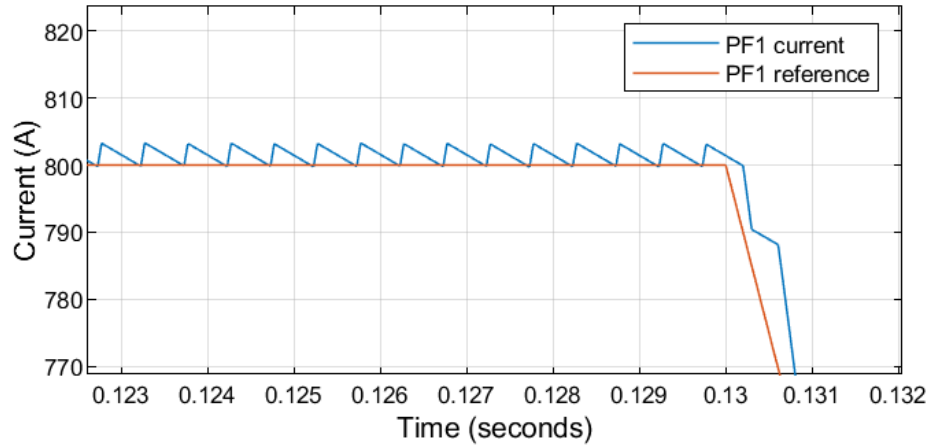

Figure 5-12: PF1 current ripple

The voltage seen by the coil is discontinuous due to the H-bridge switching. The voltage during operation is represented in Figure 5-13. As the power supply design is for phase 1 and the coils are designed for phase 2, the 2000V rated voltage for the two PF1 in series, obtained is Section 4.6, is far beyond the voltage achieve by the power supply.

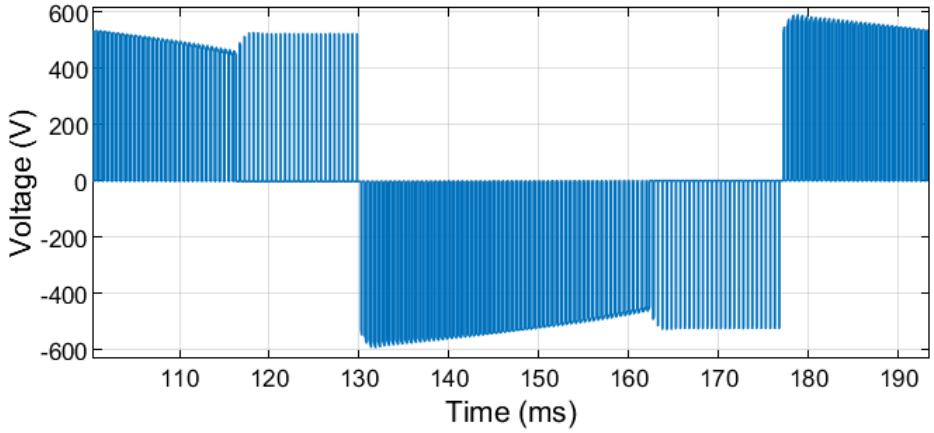

Figure 5-13: PF1 voltage during operation

The SB of this power supply is shared between PF1 power converter and the PF2 one. The input current of the power converters is also discontinuous. The LC filter allows to achieve just a maximum ripple of 1.6% in the SB with respect to its maximum peak current. In Figure 5-14 and Figure 5-15 is shown a comparison between the input current of the converter and the current that goes through the SB, and how the large ripple is almost avoided due to the filter. These currents are also equal to the output and input current of the LC filter, respectively. Figure 5-15 also shows the great margin that still have the SB up to its current limit.

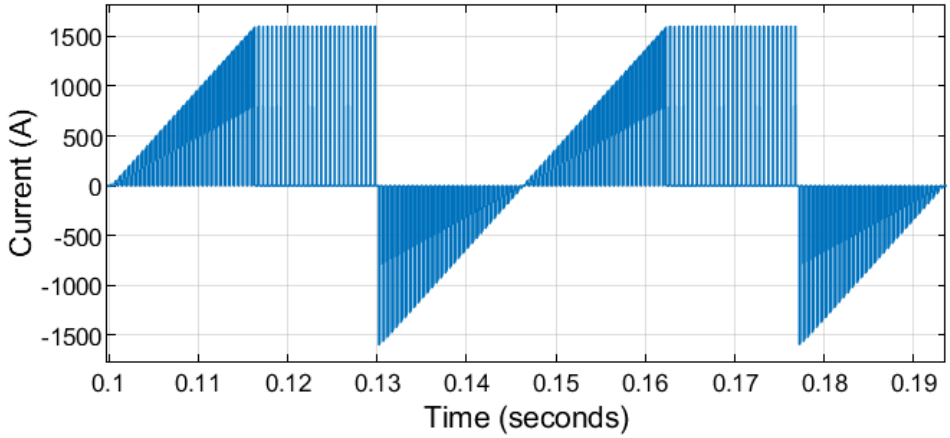

Figure 5-14: Input current in the PF1 and PF2 H-bridge converters

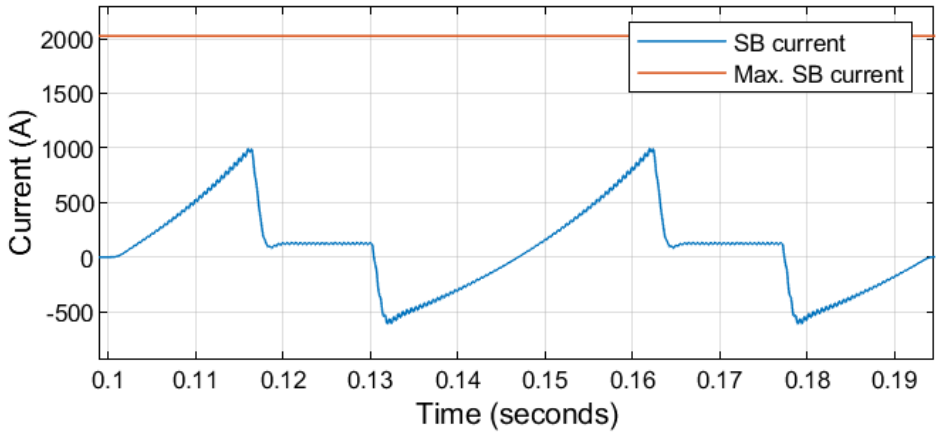

Figure 5-15: Current through the PF1 and PF2 SB and the maximum peak current of the SB

Regarding the voltage limit, the 13 SM in series are selected to have enough margin for the voltages increases due to the coil discharges, shown in Figure 5-16, and to have a duty cycle for the PWM of the H-bridge converter lower than 0.9, shown in Figure 5-17.

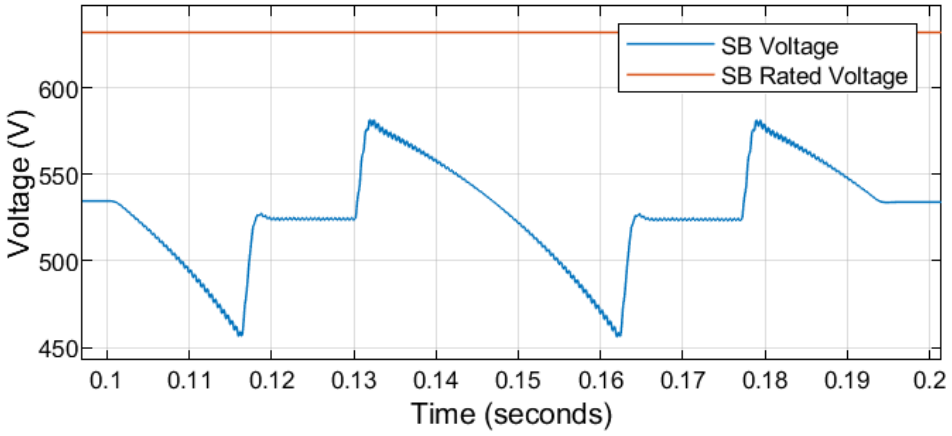

Figure 5-16: Voltage of PF1 and PF2 SB and rated voltage of the SB

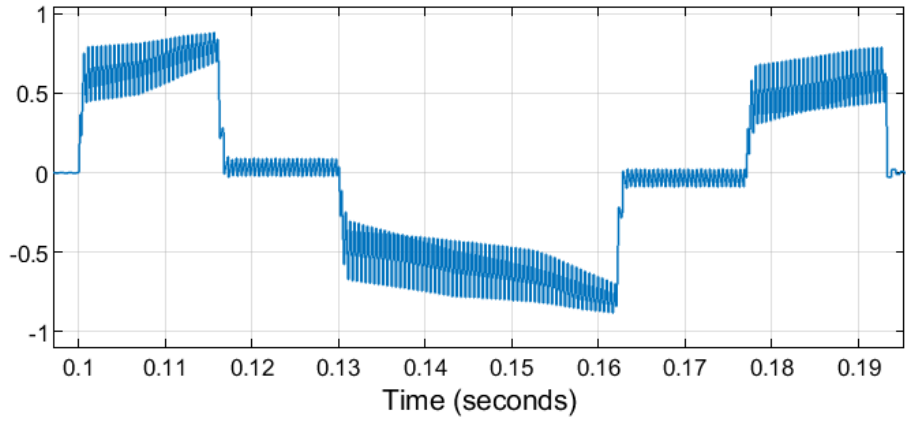

Figure 5-17: Duty cycle of the PF1 power converter

In the case of PF2, the current following the reference is shown in Figure 5-18. In this case, as it has lower inductance, the current ripple is slightly higher and goes up to 0.49%, represented in Figure 5-19.

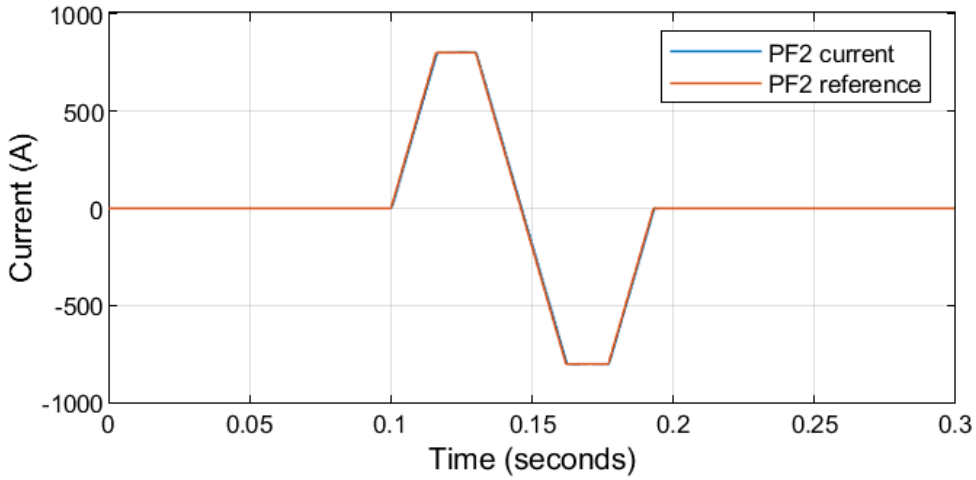

Figure 5-18: PF2 current compare to reference

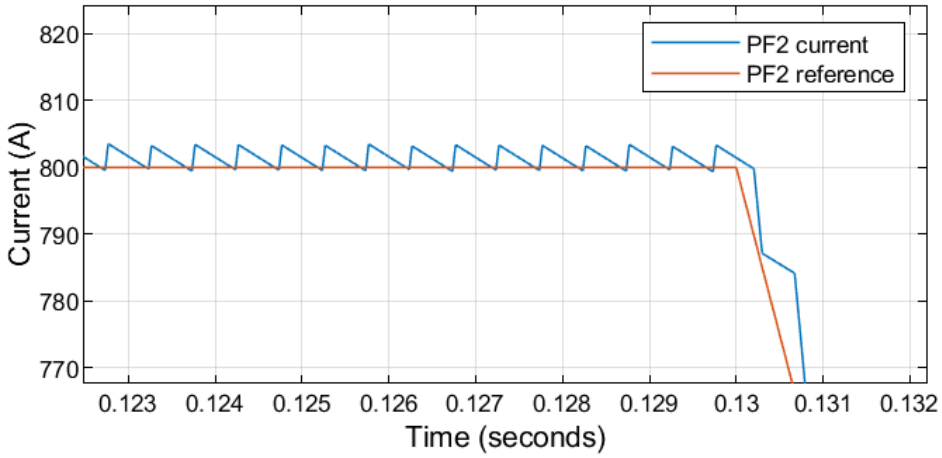

Figure 5-19: PF2 current ripple

The maximum voltage level of PF2 coils is the same that for PF1, as it is shown in

Figure 5-20. However, the duty cycle, in Figure 5-21, is lower as the lower resistance and inductance of the PF2 coils requires less mean voltage compare to PF1 coils.

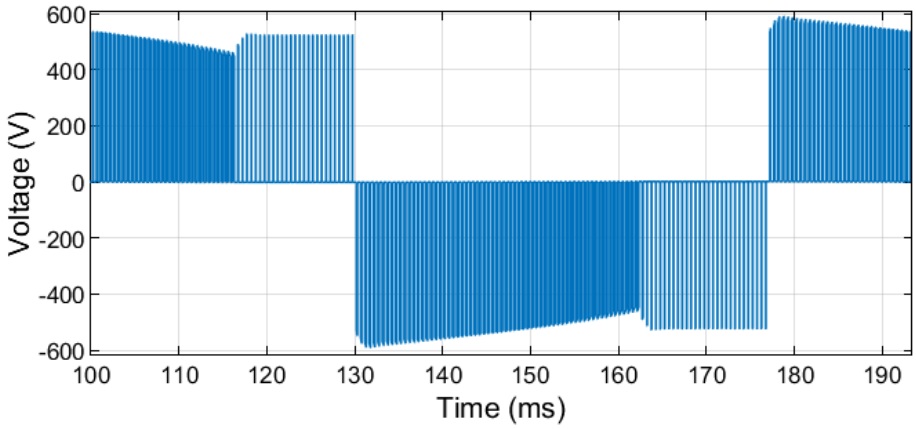

Figure 5-20: PF2 voltage during operation

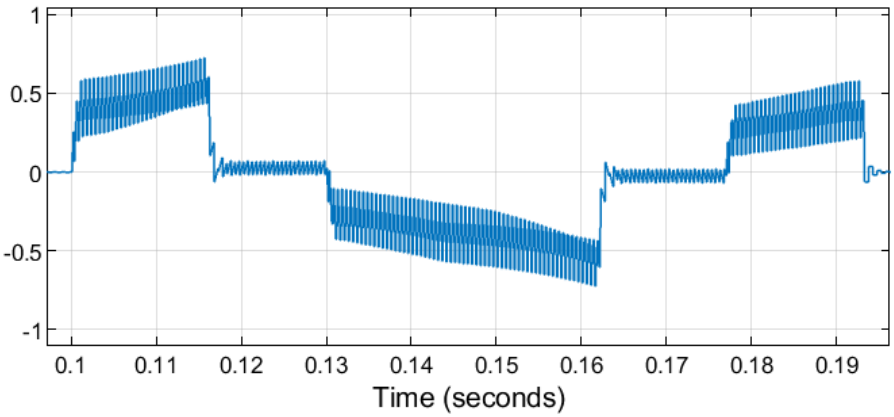

Figure 5-21: Duty cycle of the PF2 power converter

5.2.3 Div1 simulation results

Div2 needs to be supplied by 2 power converters in parallel, each of them with its own SB. In Figure 5-23, it is shown how the total current matches the reference. The current ripple, represented in Figure 5-23, is 0.42% with respect to the rated current.

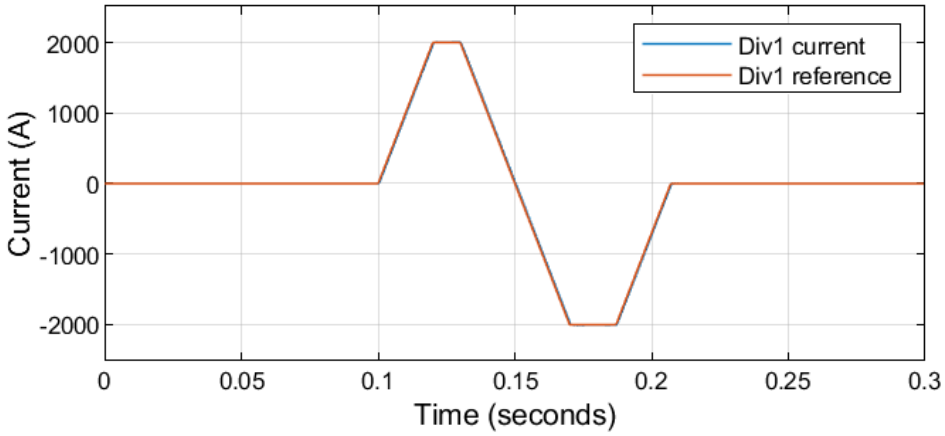

Figure 5-22: Div1 current compare to reference

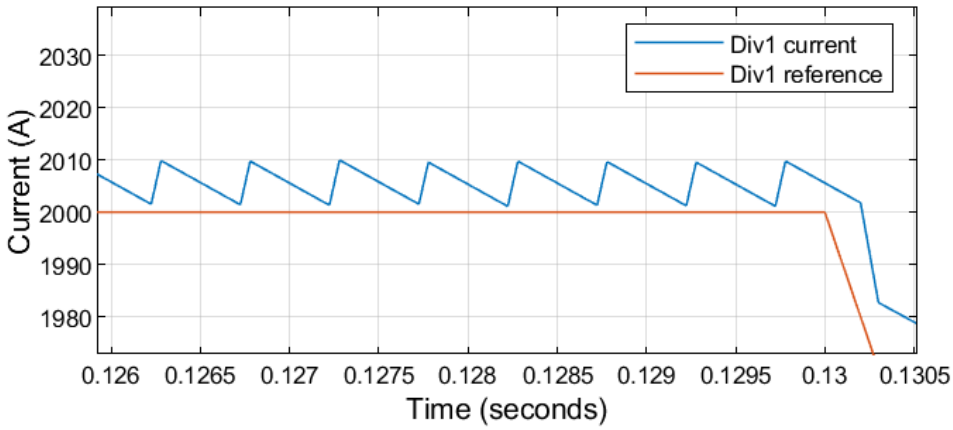

Figure 5-23: Div1 current ripple

The currents of each H-bridge, shown in Figure 5-4, are correctly equilibrated thanks to the control system explained in Section 5.1.4, where each H-bridge have to fulfill the total current for the TFC and the specific current of the H-bridge.

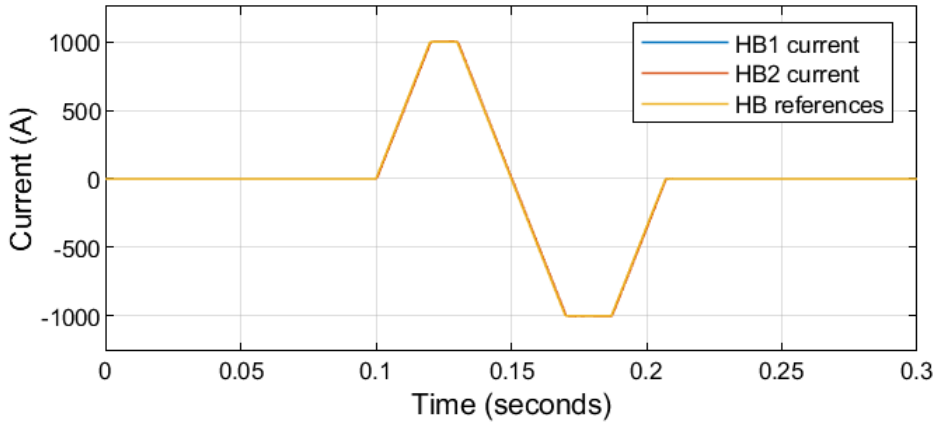

Figure 5-24: Div1 H-Bridges output currents compare to a reference

The maximum voltages for the Div1 coils, shown in Figure 5-25, are lower than the limit of 1000V obtained in Section 4.6. The current ripple of the input of each H-bridge, in Figure 5-26, is minimize by an LC filter to achieve a current through each SB, in Figure 5-27, with a ripple of 0.72% and enough current margin.

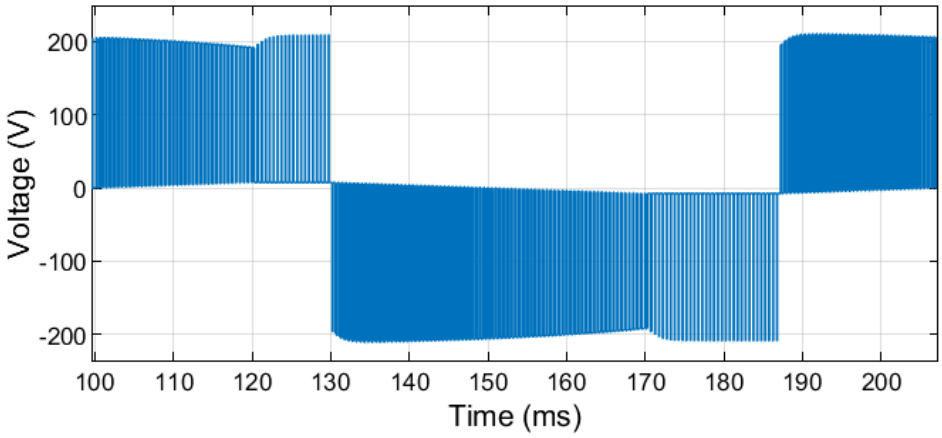

Figure 5-25: Div1 voltage during operation

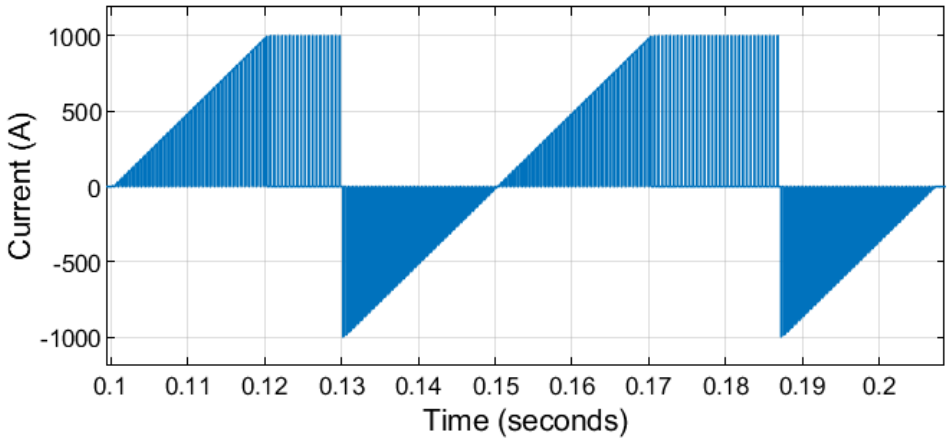

Figure 5-26: Input current in Div1 one H-bridge converter

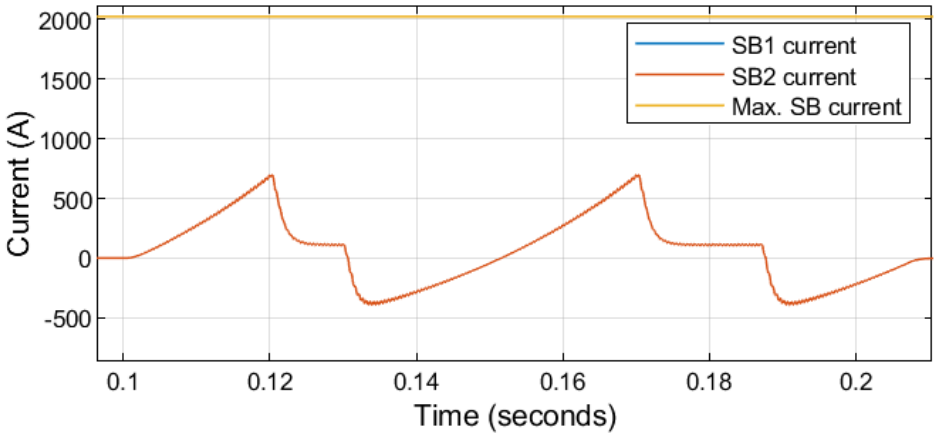

Figure 5-27: Current through Div1 SB and the maximum peak current of each SB

The SB consist of 7 SM that allow enough margin for the voltage variations of the SB, shown in Figure 5-28, and to achieve a duty cycle lower than 0.9, in Figure 5-29.

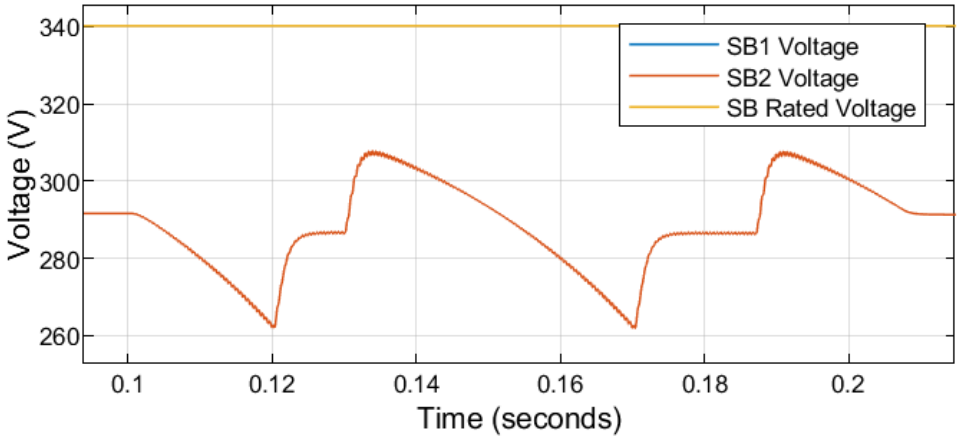

Figure 5-28: Div1 SB voltages

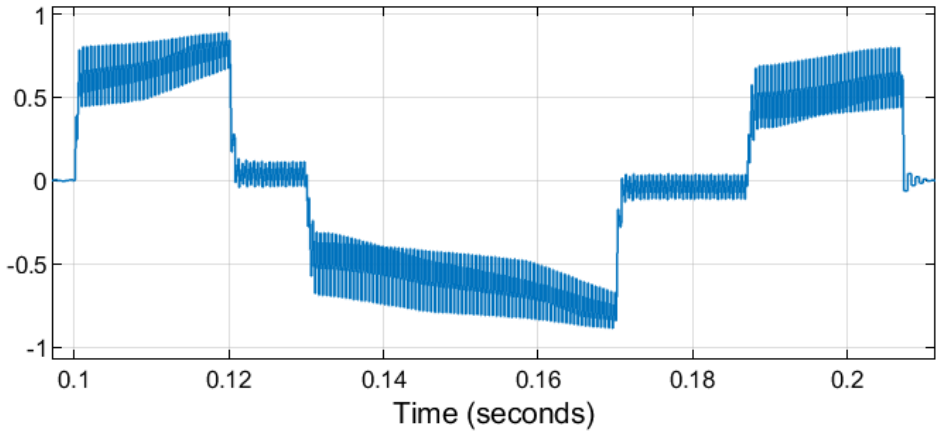

Figure 5-29: Duty cycle of one Div1 power converter

5.2.4 Upper and lower Div2 simulation results

The Upper and lower Div2 are connected to two different power converters but both connected to the same SB. Therefore, is a system very similar to PF1 and PF2 power supply but with two exact equal coils. Therefore, just the results of Upper Div1 are presented as are equal to the ones for Lower Div1. Once again, the current compare to the reference is shown in Figure 5-30 and its current ripple, in Figure 5-31, is 0.57%.

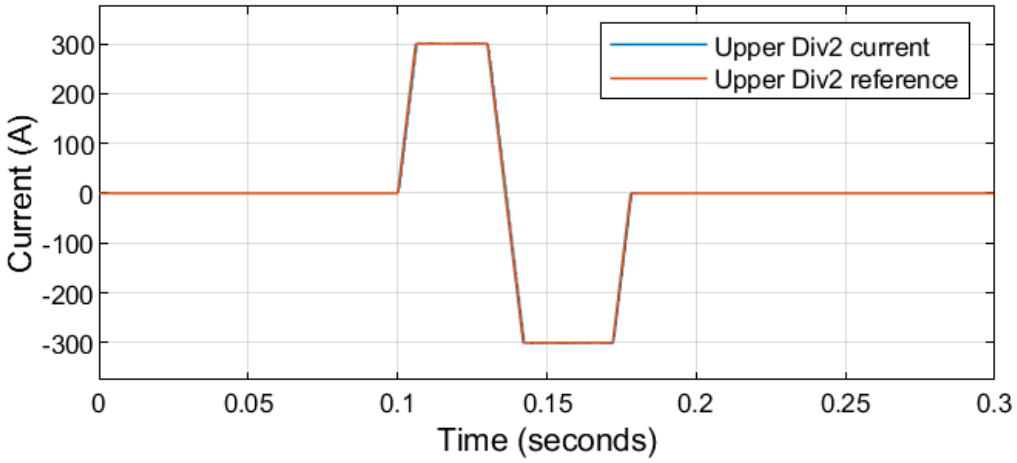

Figure 5-30: Upper Div2 current compare to reference

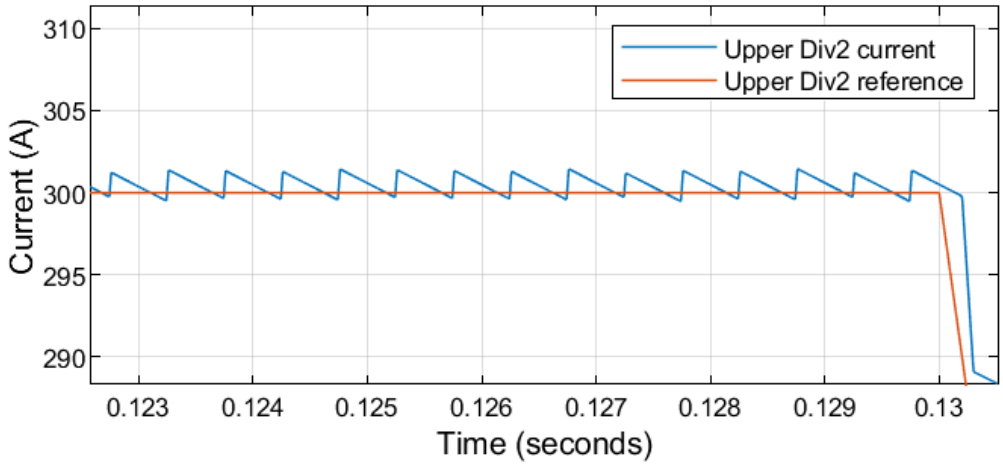

Figure 5-31: Upper Div2 current ripple

The coil voltage, in Figure 5-32, is lower than the 1000V of rated voltage from Section 4.6. The input current ripple, in Figure 5-33, of the power converter is reduced to 0.22% in the SB, in Figure 5-34, due to the LC filter.

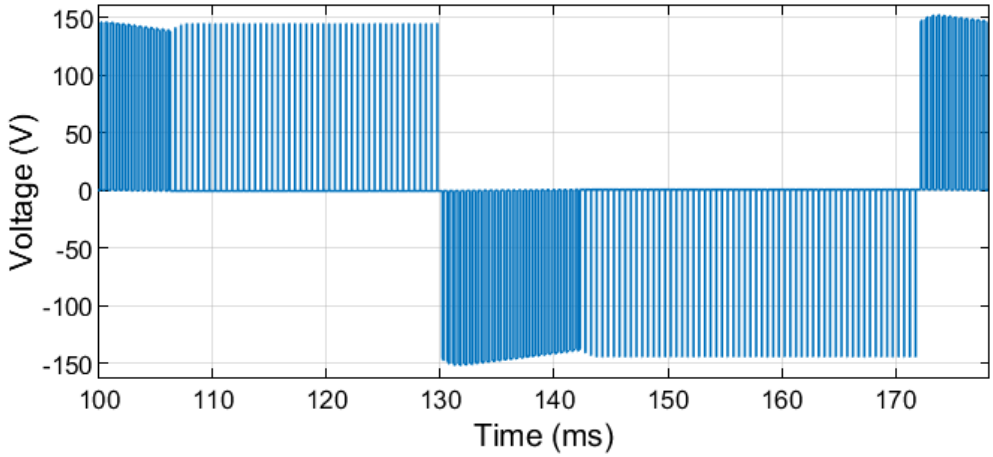

Figure 5-32: Upper Div2 voltage during operation

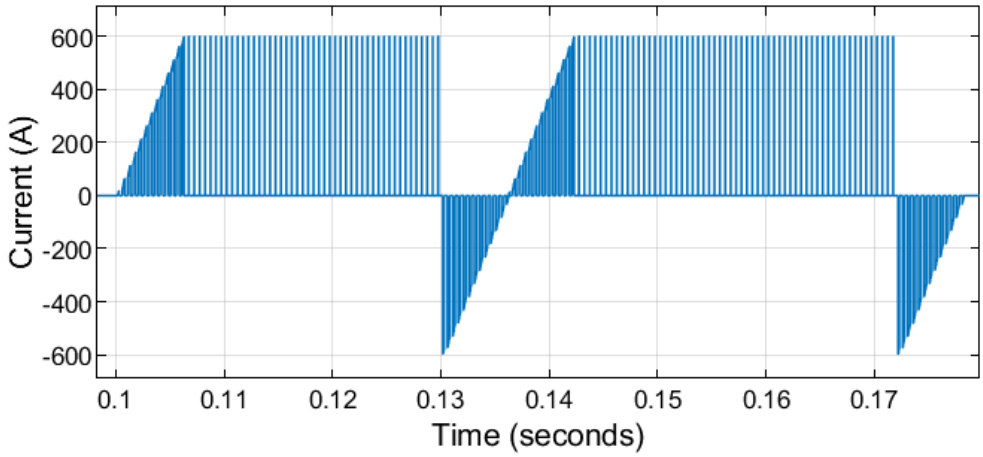

Figure 5-33: Input current in Upper and Lower Div2 one H-bridge converters

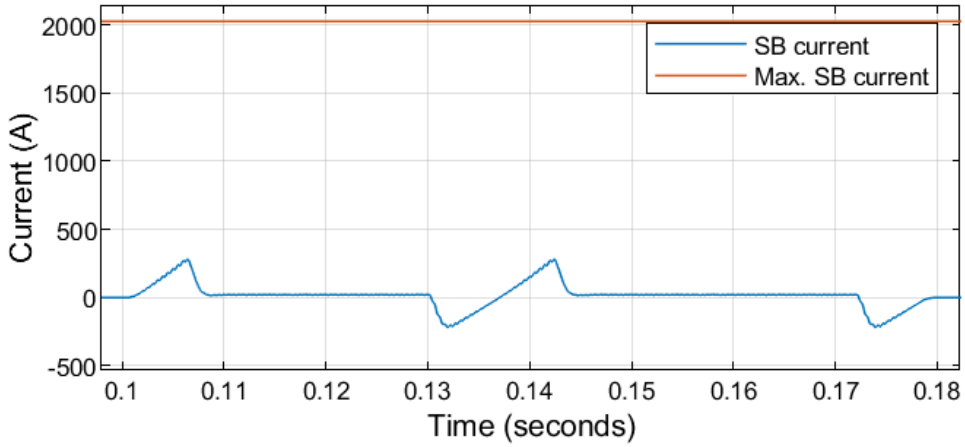

Figure 5-34: Current through the Upper and Lower Div2 SB and the maximum peak current of the SB

The SM in series to form the SB are 4, further enough to have margin between the voltage during operation and the rated voltage, shown in Figure 5-35, and to always have a duty cycle for the PWM lower than 0.9, in Figure 5-36.

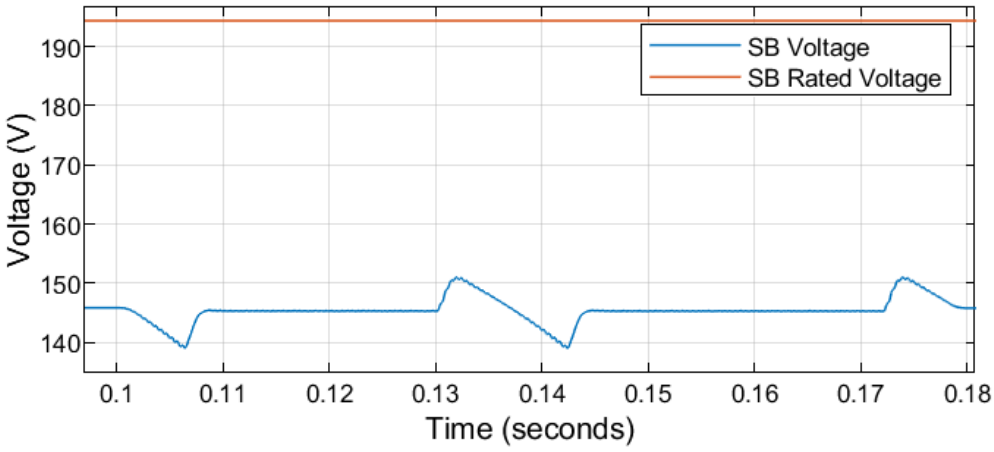

Figure 5-35: Upper and Lower Div2 SB voltage

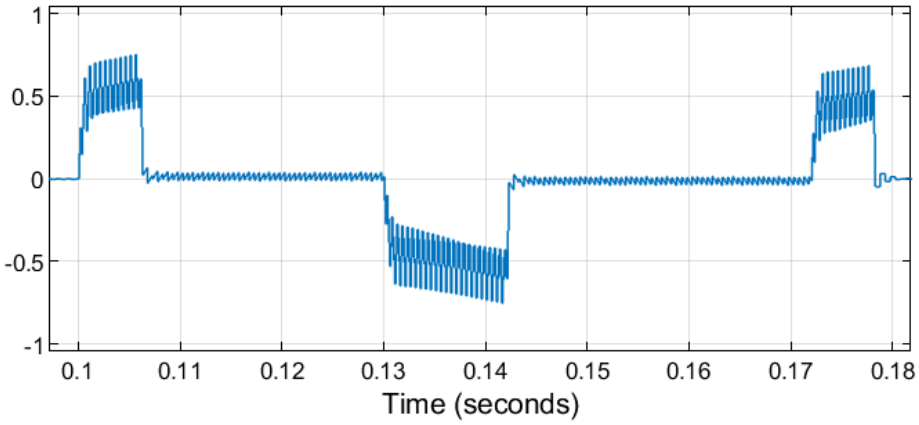

Figure 5-36: Duty cycle of the Upper Div2 power converter

5.3 TFC power supply

5.3.1 TFC power supply topology

As Div1, TFC have an operational current larger than the 1.5kA of the rated output current of the power converter defined in Section 5.1.1. Therefore, parallelization is needed. In this case, four converters in parallel are required. In Figure 5-37 it is shown the topology and in Table 5-6, the specifications of the power supply. As this system just need positive current, a modified H-bridge topology for two quadrants has been used as in the case of PROTO-SPHERA in Section 2.4.1.

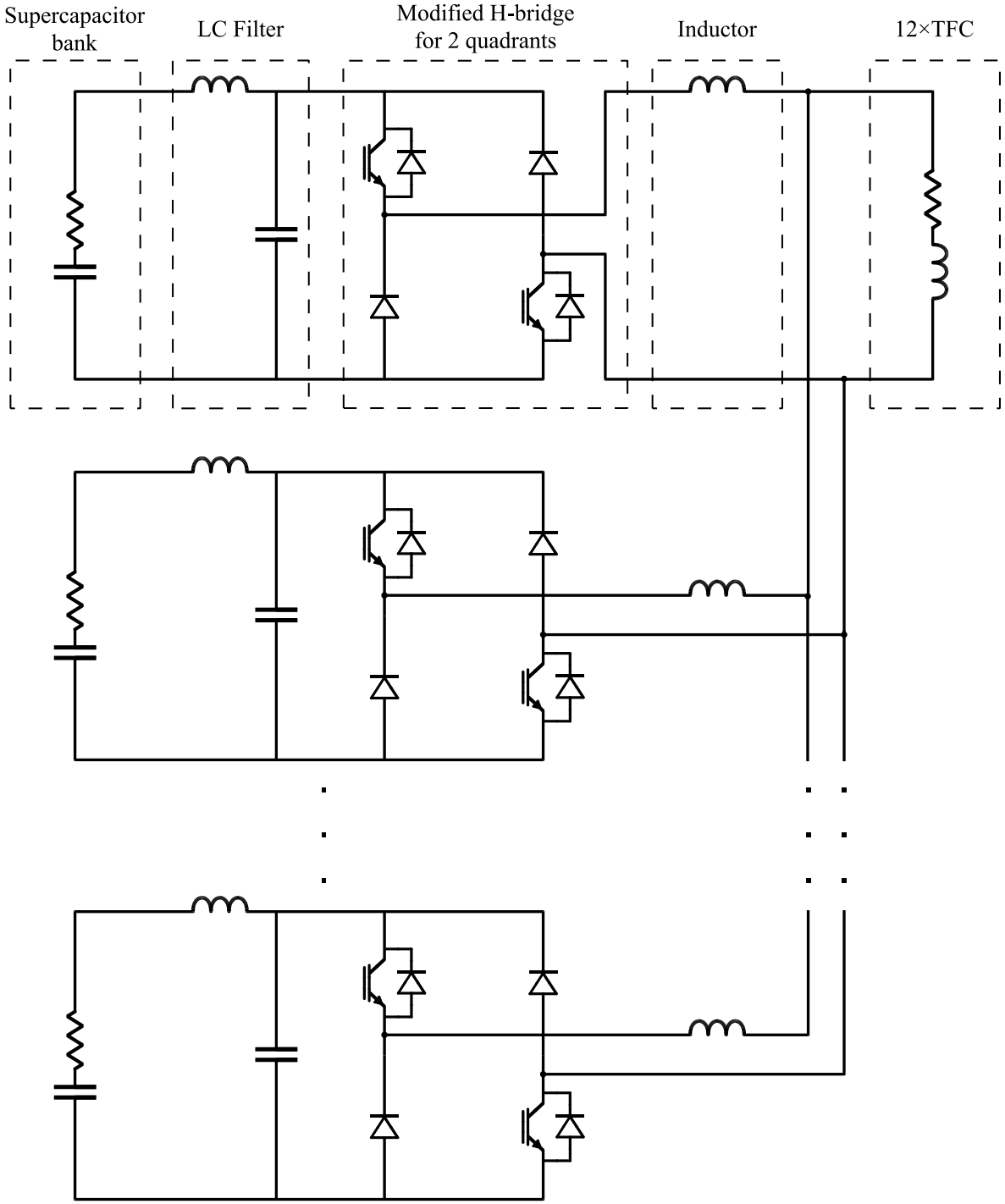

Figure 5-37: TFC power supply topology based on parallelization of H-bridges converters

Table 5-6: TFC power supply specifications

Parameter	12×TFC
Nº of SB and filters	4
Nº of H-bridges	4
SM in series	7
Rated current (A)	6000
Rated voltage (V)	340.2
SB current ripple (%)	1.99
Load current ripple (%)	0.13
Filter L (µH)	2.8
Filter C (mF)	73.6
Sharing inductor (mH)	1

5.3.2 TFC simulation results

The TFC requires four power converters in parallel, each of them with their own SB, to supply the total current required. It is a similar system to Div1 power supply, but the H-bridge are modified as they only provide positive current. The total current with its reference is represented in Figure 5-38. Its ripple, in Figure 5-39, is 0.13%.

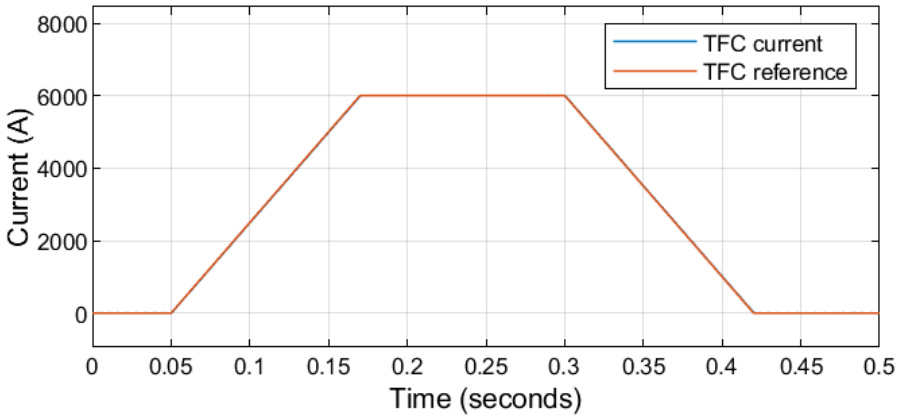

Figure 5-38: TFC current compare to reference

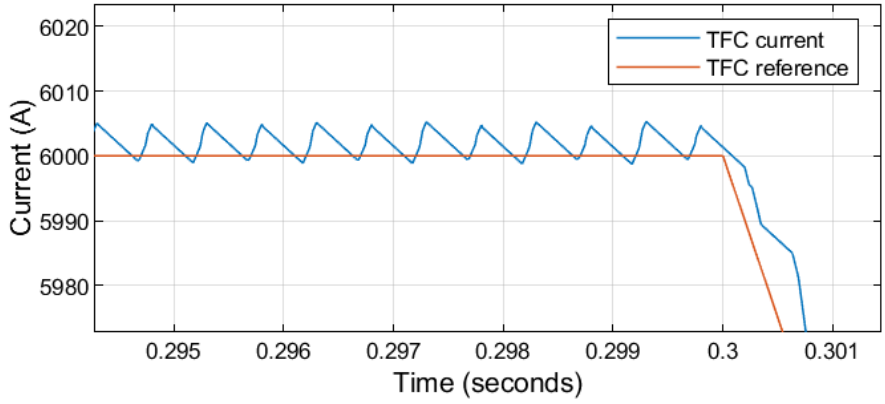

Figure 5-39: TFC current ripple

The current is well distributed between the four H-bridges due to the control strategy, as is shown in Figure 5-40. The reference voltage of each H-bridge tries to compensate its error and the one of the total current.

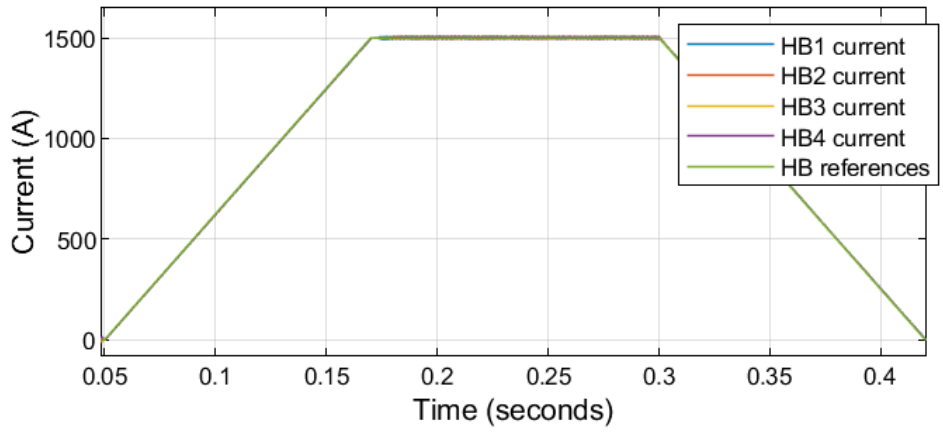

Figure 5-40: TFC H-Bridges output currents compare to a reference

The voltage of the TFC, in Figure 5-41, is lower than the 1000V of rated voltage defined in Section 4.6.

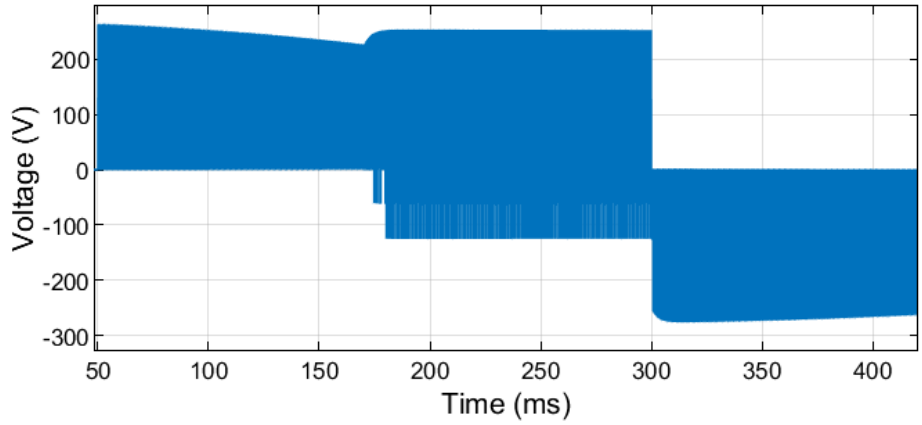

Figure 5-41: TFC voltage during operation

The ripple of the input current of the H-bridges, in Figure 5-42, is reduced for the SB current, in Figure 5-43, to 1.99% of the maximum peak current of the SB with the LC filter.

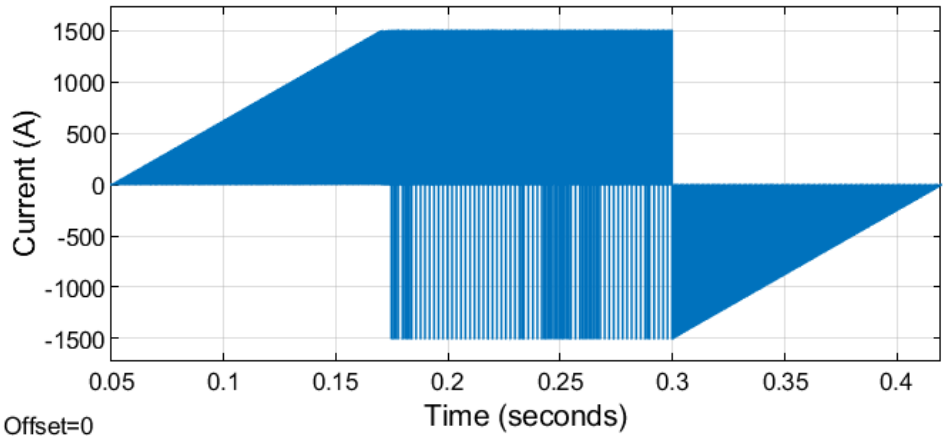

Figure 5-42: Input current in one TFC H-bridge converter

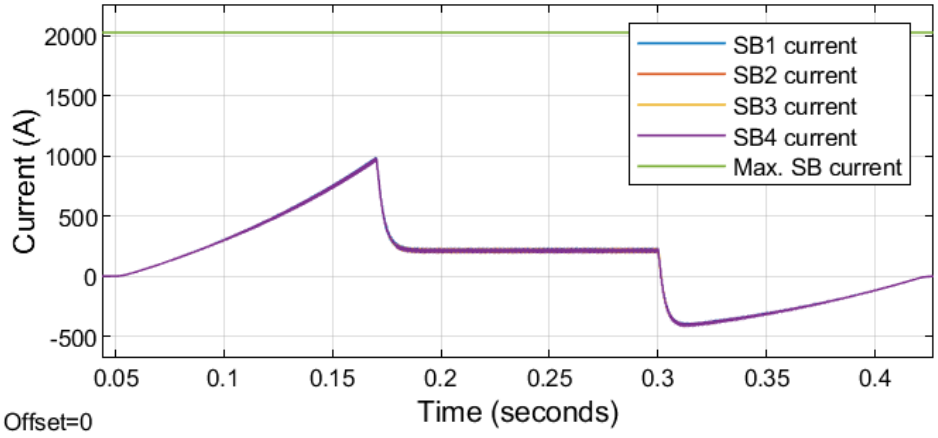

Figure 5-43: Current through TFC SB and the maximum peak current of each SB

The 7 SM in series are able to operate the SB without surpassing the rated voltage, as it is shown in Figure 5-44, and it obtains duty cycles for the PWM of the H-bridges lower than 0.9, shown in Figure 5-45.

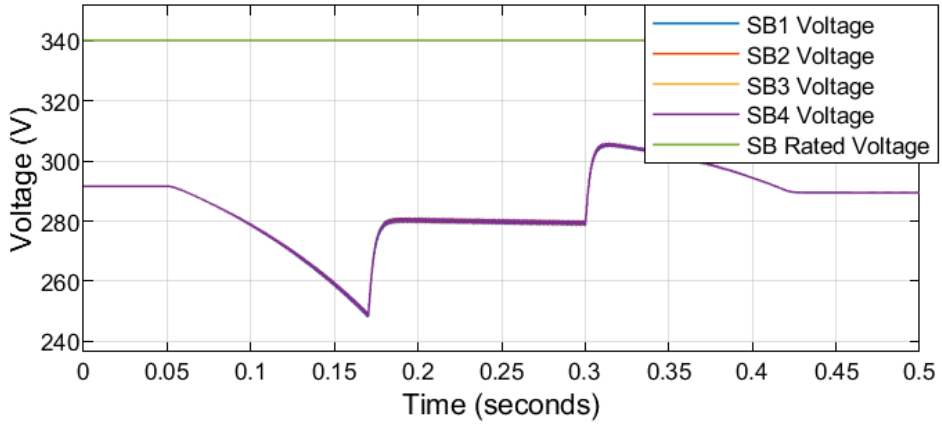

Figure 5-44: TFC SB voltages

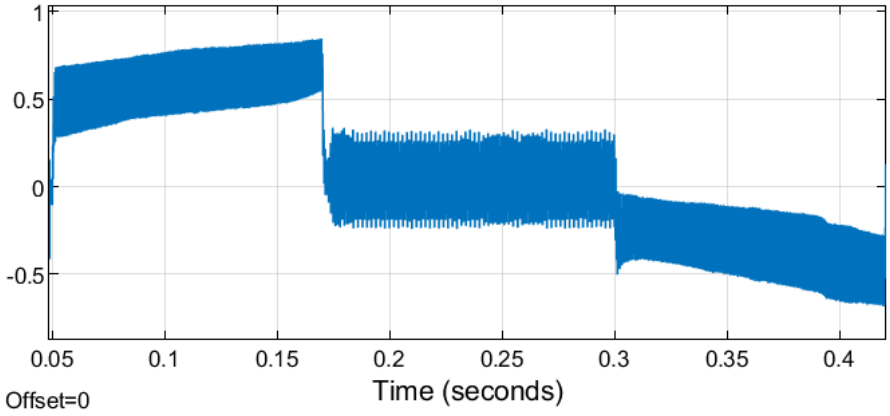

Figure 5-45: Duty cycle of one TFC power converter

5.4 Central solenoid power supply

5.4.1 Central solenoid power supply topology

The central solenoid power supply could completely fit its operational limits with the power supply baseline. However, as a first approach, in order to reduce the number of supercapacitors required, an auxiliary circuit with a capacitor and a dumping resistor, represented in Figure 5-46, was included to achieve the breakdown slope.

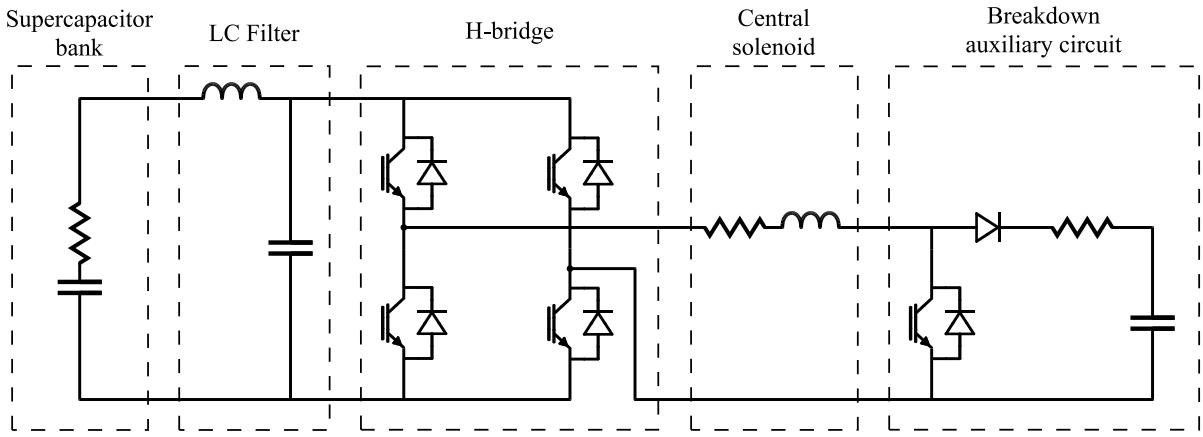

Figure 5-46: First version of the central solenoid power supply

Firstly, the H-bridge operates, and the auxiliary circuit is short-circuited thanks to the IGBT. When the breakdown starts, the H-bridge is short-circuited by the two upper or lower IGBT and the one of the auxiliary circuit opens. The capacitor of this circuit starts to be charged by the coil and when the current change of sign the central solenoid is short-circuited due to the antiparallel diode of the IGBT. At this point, the IGBT of the auxiliary circuit is closed, and the H-bridge operates again. The capacitor voltage and the resistance value are chosen to obtain the required slope for breakdown. In Figure 5-47, a generic reference is shown and indicates in which part operates each circuit.

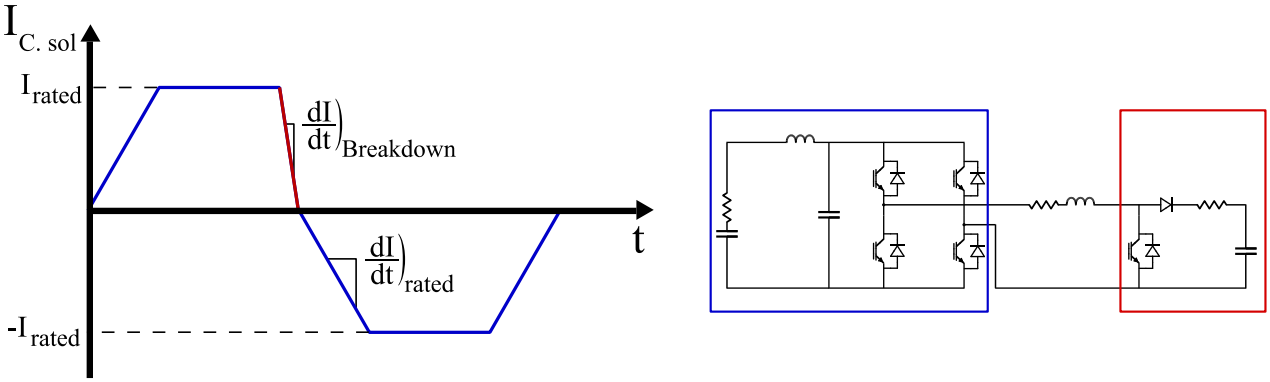

Figure 5-47: Refence current waveform for a first version of the central solenoid power supply. In blue and red which part of the circuit oversees each part of the current waveform

However, this system only allows to maintain the breakdown slope if the current is positive. It would be interesting to continue the slope in the negative part in order to maintain the breakdown condition for a longer time without increasing the maximum current value. Therefore, the topology in Figure 5-48 is proposed.

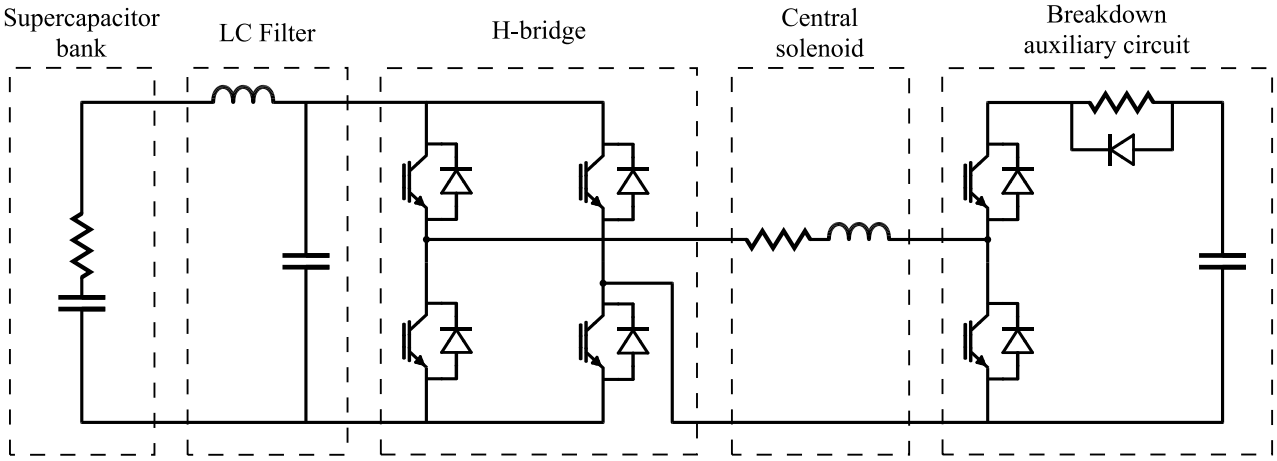

Figure 5-48: Final version of the central solenoid power supply

The second IGBT of the auxiliary circuit allows the recirculation of the current through the capacitor, maintaining the current slope even if the current is negative. The diode in parallel with the resistance avoid the counter-productive effect of the resistance while the current is increasing in the negative region. It is a similar system to the one used for breakdown by VEST power supply in Section 2.3.2. The current reference is shown in Figure 5-49 and, once again, which part is operated by each circuit. In Table 5-7, the final specifications of this power supply are presented.

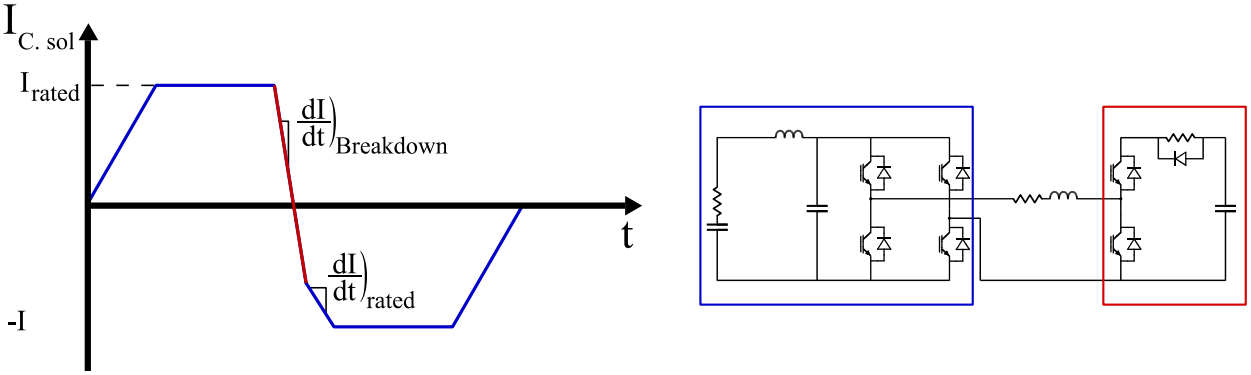

Figure 5-49: Reference current waveform for final version of the central solenoid power supply. In blue and red which part of the circuit oversees each part of the current waveform

Table 5-7: Central solenoid power supply specifications

Parameter	Central solenoid
Nº of SB and filters	1
Nº of H-bridges	1
SM in series	7
Rated current (A)	1500
Rated voltage (V)	340.2
SB current ripple (%)	1.82
Load current ripple (%)	0.8
Filter L (μH)	15.0
Filter C (mF)	13.5
Aux. dumping resistor (mΩ)	100
Aux. capacitor (mF)	10
Aux. capacitor rated voltage (V)	700

5.4.2 Central solenoid simulation results

The central solenoid power supply operates switching at high frequency except for the breakdown slope. For this ramp, the voltage of the capacitor and the resistance of the auxiliary circuit have to be selected in order to achieve the required slope. In Figure 5-50 is shown how the current matches correctly with the reference. The ripple, in Figure 5-51, obtained with the H-bridge is 0.8%.

A detail of the current for breakdown is shown in Figure 5-52, it is shown that the current does not switch during the hole breakdown and it have the second order dynamic of an RLC circuit. Therefore, this part has to be controlled as an open loop and after the breakdown, the close loop control of the H-bridge operates again.

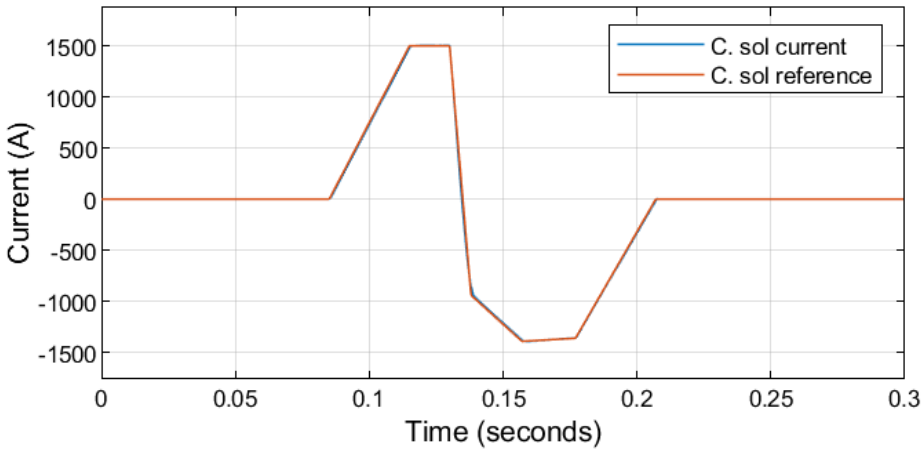

Figure 5-50: Central solenoid current compare to reference achieving breakdown slope with negative current

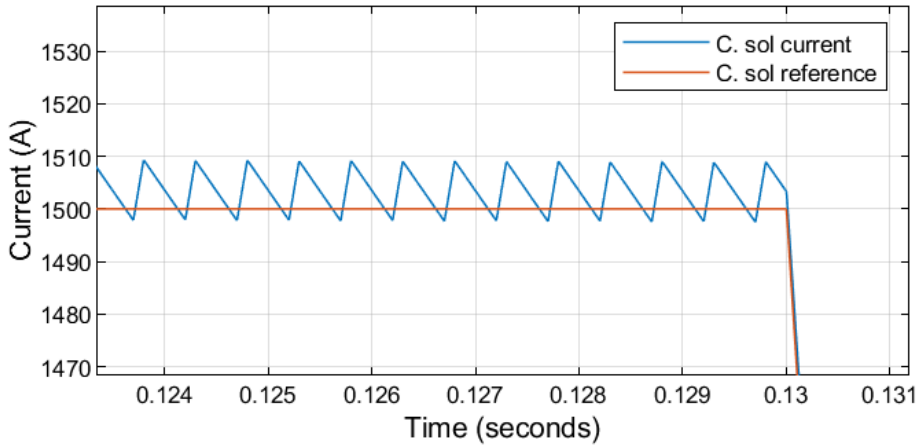

Figure 5-51: Central solenoid current ripple

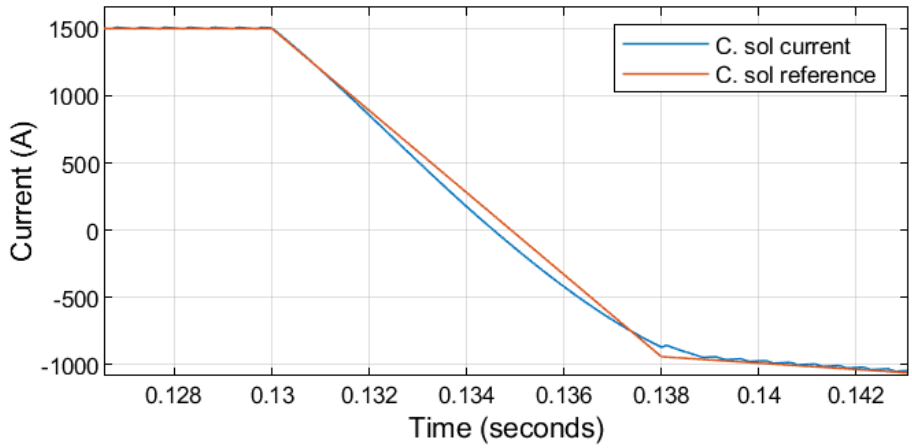

Figure 5-52: Central solenoid current during breakdown. The auxiliary circuit does not switch during its operation

In Figure 5-53, it is shown how the central solenoid voltage increases significantly during breakdown, but is much less than the 2000V of rated voltage obtained in Section 4.6. The voltage during the breakdown is due to the charge of the capacitor of the auxiliary circuit by the discharge of the coil. When the coil current is negative, the capacitor starts to charge the coil again, as is shown in Figure 5-54. The 700V of rated voltage of this capacitor is defined to have enough margin for this voltage variation. The current going through this capacitor is shown in Figure 5-55.

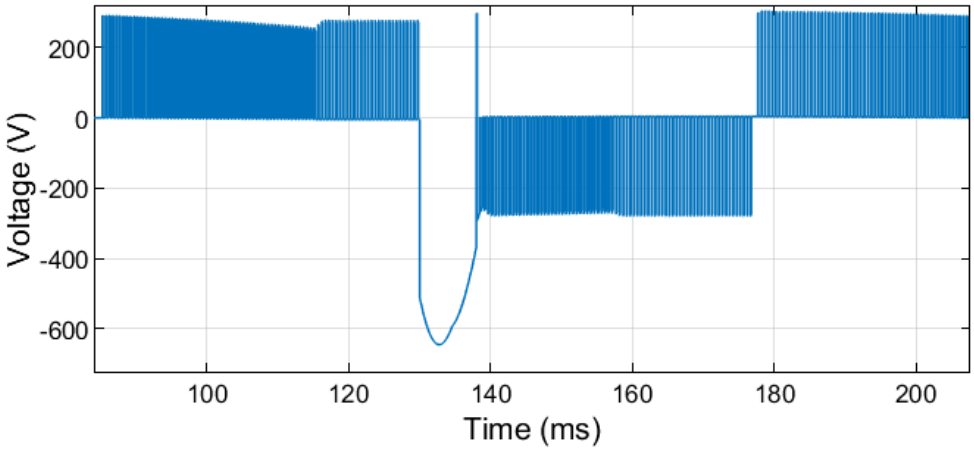

Figure 5-53: Central solenoid voltage during operation

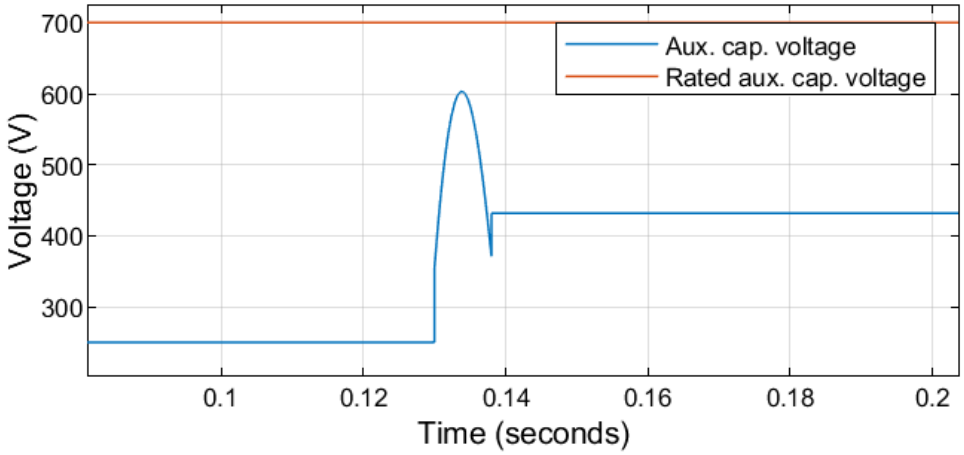

Figure 5-54: Auxiliary circuit capacitor voltage during operation

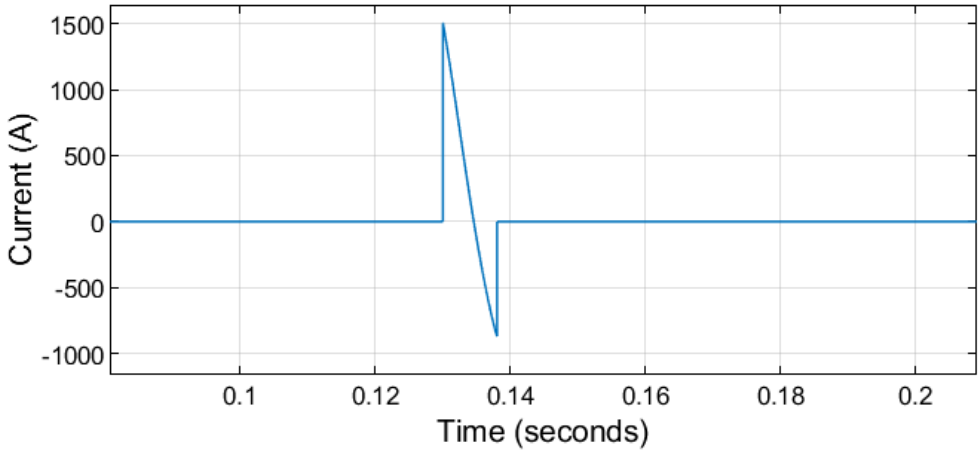

Figure 5-55: Auxiliary circuit capacitor current

The only IGBT that have to withstand this high voltage is the opened IGBT of the auxiliary circuit. The voltage of this IGBT is represented in Figure 5-56. Therefore, none of the components of the H-bridge circuit have to withstand the voltage for breakdown, reducing the cost of it.

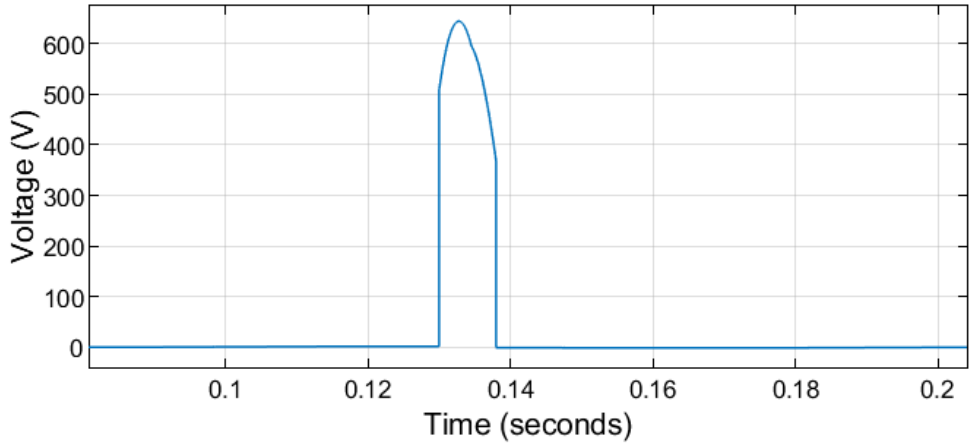

Figure 5-56: Voltage the have to withstand the opened IGBT of the auxiliary circuit during breakdown

The ripple input current of the H-bridge, represented in Figure 5-57, is minimize with the LC filter, obtaining a ripple of 1.82% in the current through the SB, represented in Figure 5-58.

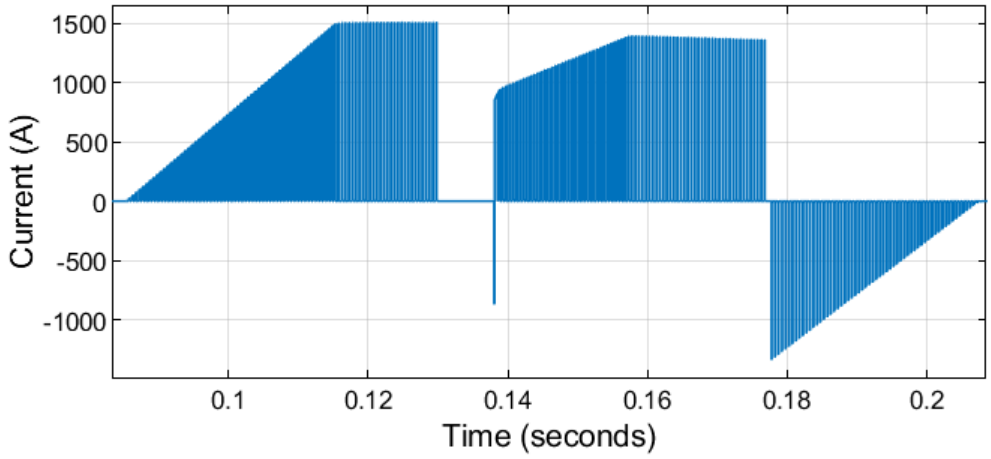

Figure 5-57: Input current in the central solenoid H-bridge converter

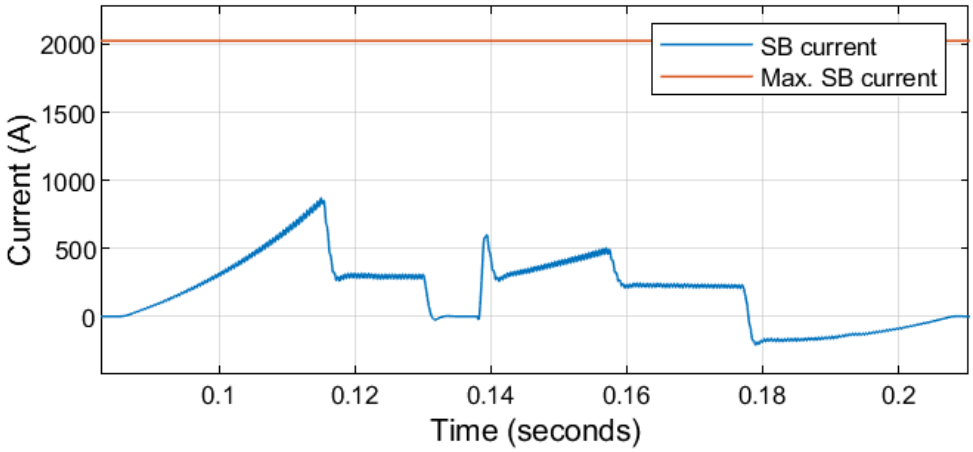

Figure 5-58: Current through the Upper and Lower Div2 SB and the maximum peak current of the SB

The SB consist of 7 SM in series that are able to operate the SB with enough voltage margin, as is shown in Figure 5-59, and a duty cycle generally lower than 0.9, in Figure 5-60. The peaks in the duty cycle that goes up to 1 and -1 are because of the transient between the open loop to the close loop control after the breakdown slope.

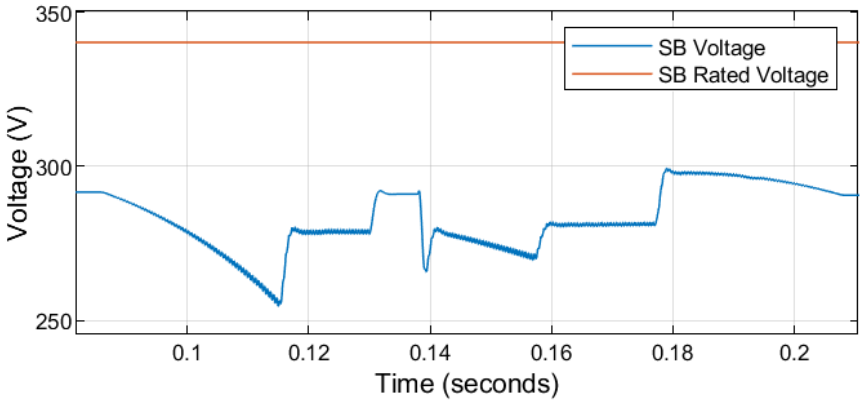

Figure 5-59: Upper and Lower Div2 SB voltage

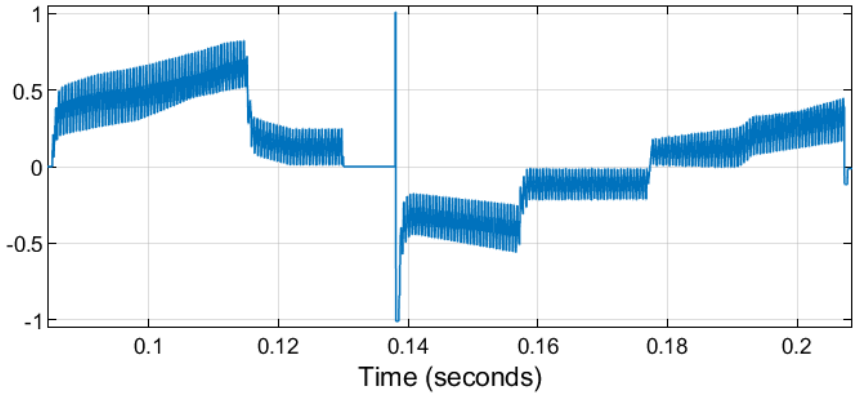

Figure 5-60: Duty cycle of the Upper Div2 power converter

5.5 Power supply overview

The final power supply specifications obtained are presented in Table 5-8.

Table 5-8: Power supply specifications

Parameter	12×TFC	C. solenoid	2×PF1/2×PF2	2×Div1	Upper Div2 / Lower Div2
Nº of SB and filters	4	1	1	2	1
Nº of H-bridges	4	1	2	2	2
SM in series	7	7	13	7	4
Rated current (A)	6000	1500	800	2000	300
Rated voltage (V)	340.2	340.2	631.8	340.2	194.4
SB current ripple (%)	1.99	1.83	1.60	0.72	0.22
Load current ripple (%)	0.13	0.8	0.43/0.49	0.42	0.57
Filter L (µH)	2.8	15.0	25.2	6.7	6.7
Filter C (mF)	73.6	13.5	8.11	30.2	30.2
Sharing inductor (mH)	1	–	–	1	–
Aux. dumping resistor (mΩ)	–	100	–	–	–
Aux. capacitor (mF)	–	10	–	–	–
Aux. capacitor rated voltage (V)	–	700	–	–	–

The rated current matches with the operational limits and the rated voltage with the sum of the rated voltages of the SM in series. It can be seen how the number of SM in series for the central solenoid have been reduced thanks to the auxiliary circuit that reaches up to 700V of rated voltage. Therefore, a complete power supply system have been designed where all the restrictions are fulfilled with enough safety margin, the ripple for the SB is always lower than 2% and the current ripple of the load is in all cases lower than 1%. With a ripple of this order of magnitude, the coils are able to confine the plasma with enough margin. Therefore, the main objective of this contribution is fulfilled.

6 CONCLUSION AND FUTURE WORK

6.1 Conclusion

The main objective and secondary objectives of this document have been successfully fulfilled. After a first overview of reference devices, including the description of some of their coils and power supplies, the definition of SMART components and operational limits was achieved. For the obtention of these limits, different plasma scenarios were considered to withstand the required values in all the possible cases.

The coils design was achieved able to withstand the operational limits defined for the first two operation phases of SMART. The cross-section required was estimated considering the geometry of the vessel and a simple analytical thermal model. The maximum temperature increase for the coils was of 5 ºC for phase 2. Commercial hollow conductors where employed for the central solenoid and PFC to allow the possible future use of water-cooling systems.

After the definition of the electrical parameters of the coils, the power supplies topologies for the first operation phase of SMART were defined taking into account the operational limits for this phase and the technical restrictions of commercial elements.

The final specifications for the complete power supply were fixed by the simulation of the system in MATLAB Simulink. A robust power supply has been designed where the operational limits are successfully achieved. The current ripple for the SMART coils is lower than 1%, which allows the complete control of the plasma confinement for the first operation of the tokamak.

6.2 Future work

The SMART project is currently in a phase where the design of the system will be completely optimized for the future commissioning and construction of the system. The following tasks are proposed:

- Study of an extended phase 2 or a third phase

As it was explained in Chapter 4, if a water-cooling system can be implemented to the coils, there is still and important margin for temperature increase. Therefore, a possible extended phase 2, with a longer pulse length, or even a phase 3, with enhanced plasma parameters, should be studied to maximize the use of the coils.

- Thermal and structural finite-element analysis

In order to study an extended phase 2, it is mandatory to have a detailed thermal analysis including the water-cooling system to define the maximum operational limits of the coils for this case. Furthermore, a structural analysis is required to guarantee that all the coils withstand the stresses produced by their magnetic interaction.

- Thermal study of the H-bridge converter

Due to the pulsed operation of the system, the current limit of the H-bridge converter is between the maximum instant current withstood by the component elements and the maximum current in continuous operation. To estimate this limit, a thermal study of the converters should be done considering our specific current waveforms.

- Optimization of the LC filter

The LC filter should be optimized in order to ensure a save temperature increase of the SM due to the current ripple produced by the converter.

REFERENCES

[1] "Advantages of fusion." https://www.iter.org/sci/Fusion (accessed Jul. 09, 2020).

[2] A. Lampasi and S. Minucci, "Survey of electric power supplies used in nuclear fusion experiments," Jul. 2017, doi: 10.1109/EEEIC.2017.7977851.

[3] A. Lampasi, S. Tenconi, G. Taddia, F. Gherdovich, and L. Rinaldi, "A new generation of power supplies for pulsed loads," *Fusion Eng. Des.*, vol. 146, pp. 1921–1925, Sep. 2019, doi: 10.1016/j.fusengdes.2019.03.066.

[4] F. Wagner, "Electricity by intermittent sources: An analysis based on the German situation 2012," *Eur. Phys. J. Plus 2014 1292*, vol. 129, no. 2, pp. 1–18, Feb. 2014, doi: 10.1140/epjp/i2014-14020-8.

[5] "Nuclear fusion - Wikipedia." https://en.wikipedia.org/wiki/Nuclear_fusion (accessed Jun. 30, 2020).

[6] A. Lépine-Szily and P. Descouvemont, "Nuclear astrophysics: nucleosynthesis in the Universe," *Int. J. Astrobiol.*, vol. 11, no. 4, pp. 243–250, Oct. 2012, doi: 10.1017/S1473550412000158.

[7] J. P. Freidberg, *Plasma Physics and Fusion Energy*. Cambridge: Cambridge University Press, 2007.

[8] "Tokamak | Max-Planck-Institut für Plasmaphysik." https://www.ipp.mpg.de/14869/tokamak (accessed Jun. 30, 2020).

[9] Y. An *et al.*, "Plasma start-up design and first plasma experiment in VEST," in *Fusion Engineering and Design*, Oct. 2015, vol. 96–97, pp. 274–280, doi: 10.1016/j.fusengdes.2015.05.015.

[10] V. K. Gusev *et al.*, "Globus-M results as the basis for a compact spherical tokamak with enhanced parameters Globus-M2," *Nucl. Fusion*, vol. 53, no. 9, p. 093013, Aug. 2013, doi: 10.1088/0029-5515/53/9/093013.

[11] A. Magnanimo, M. Teschke, G. Griepentrog, and M. P. I. for P. P. M. P. S. ASDEX Upgrade Team, "Supercapacitors-Based Power Supply for ASDEX Upgrade Tokamak," 2019.

[12] Z. Gao, "Compact magnetic confinement fusion: Spherical torus and compact torus," *Elsevier*, Accessed: Jul. 01, 2018. [Online]. Available: https://www.sciencedirect.com/science/article/pii/S2468080X16300279.

[13] Y.-K. M. Peng, "The physics of spherical torus plasmas," *Phys. Plasmas*, vol. 7, no. 5, pp. 1681–1692, May 2000, doi: 10.1063/1.874048.

[14] "Introduction | Max-Planck-Institut für Plasmaphysik." https://www.ipp.mpg.de/16208/einfuehrung (accessed Jul. 02, 2020).

[15] V. A. Belyakov, V. A. Korotkov, and V. F. Soikin, "Design and assembly of the globus-m tokamak magnets," *Plasma Devices Oper.*, vol. 9, no. 1–2, pp. 39–55, Dec. 2001, doi: 10.1080/10519990108224486.

[16] V. B. Minaev *et al.*, "Magnetic System for the Upgraded Spherical Tokamak Globus-M2."

[17] M. Cox, "Mega Amp Spherical Tokamak," *Fusion Eng. Des.*, vol. 46, no. 2–4, pp. 397–404, Nov. 1999, doi: 10.1016/S0920-3796(99)00031-9.

[18] K. J. Chung *et al.*, "Design Features and Commissioning of the Versatile Experiment Spherical Torus

(VEST) at Seoul National University," *Plasma Sci. Technol.*, vol. 15, no. 3, pp. 244–251, Mar. 2013, doi: 10.1088/1009-0630/15/3/11.

[19] B. K. Jung, K. J. Chung, Y. H. An, J. S. Kang, and Y. S. Hwang, "Design and commissioning of a TF coil power system using deep-cycle batteries for versatile experiment spherical torus (VEST)," *Fusion Eng. Des.*, vol. 88, no. 9–10, pp. 1597–1600, Oct. 2013, doi: 10.1016/J.FUSENGDES.2013.02.109.

[20] S. Hong, J. Park, Y. Kim, K. Chung, Y. S. Hwang, and Y. Na, "Snubber Circuit Optimization of the Central Solenoid Power System for Versatile Experiment Spherical Torus," pp. 17–19, 2018.

[21] Y. Hwang and V. Team, "Overview of Versatile Experiment Spherical Torus (VEST)," 2017.

[22] A. Lampasi *et al.*, "Progress of the Plasma Centerpost for the PROTO-SPHERA Spherical Tokamak," *Energies*, vol. 9, no. 7, p. 508, Jun. 2016, doi: 10.3390/en9070508.

[23] A. Lampasi, G. Maffia, P. Zito, G. Taddia, and S. Tenconi, "ETHICAL: A modular supercapacitor-based power amplifier for high-current arbitrary generation," Aug. 2016, doi: 10.1109/EEEIC.2016.7555773.

[24] A. Lampasi, G. Taddia, S. M. Tenconi, and F. Gherdovich, "Compact Power Supply with Integrated Energy Storage and Recovery Capabilities for Arbitrary Currents up to 2 kA," *IEEE Trans. Plasma Sci.*, vol. 46, no. 10, pp. 3393–3400, Oct. 2018, doi: 10.1109/TPS.2018.2859178.

[25] C. P. Kasemann, E. Grois, F. Stobbe, M. Rott, and K. Klaster, "Pulsed power supply system of the ASDEX upgrade Tokamak research facility," in *2015 IEEE 15th International Conference on Environment and Electrical Engineering, EEEIC 2015 - Conference Proceedings*, Jul. 2015, pp. 237–242, doi: 10.1109/EEEIC.2015.7165545.

[26] G. Cunningham, "High performance plasma vertical position control system for upgraded MAST," *Fusion Eng. Des.*, vol. 88, no. 12, pp. 3238–3247, Dec. 2013, doi: 10.1016/j.fusengdes.2013.10.001.

[27] V. D. Shafranov, "Plasma Equilibrium in a Magnetic Field," *RvPP*, vol. 2, p. 103, 1966, Accessed: Jul. 05, 2020. [Online]. Available: https://ui.adsabs.harvard.edu/abs/1966RvPP....2..103S/abstract.

[28] "Luvata | Hollow Conductors." https://www.luvata.com/products/hollow-conductors (accessed Jul. 05, 2020).

[29] C. R. Paul, "Que es el factor K?" Accessed: Jul. 04, 2020. [Online]. Available: https://www.academia.edu/11759673/Que_es_el_factor_K.

[30] Y. Zhai *et al.*, "Prototype Coil Evaluation for NSTX-U Replacement Inner Poloidal Field Coils," *Fusion Sci. Technol.*, vol. 75, no. 8, pp. 775–785, Nov. 2019, doi: 10.1080/15361055.2019.1610314.

[31] "Power Circuit Breaker Theory and Design - Google Libros." https://books.google.es/books?id=1RjpLBaFzM8C&pg=PA545&lpg=PA545&dq=epoxy+dielectrci+strength+20kV/mm&source=bl&ots=BPc-ynUpS7&sig=ACfU3U3vPidz6i7pI5F5978TfPhfLq1QZA&hl=es&sa=X&ved=2ahUKEwioi7TbmbbqAhUz8-AKHdJlCyoQ6AEwE3oECAYQAQ#v=onepage&q=epoxy dielectrci strength 20kV%2Fmm&f=false (accessed Jul. 05, 2020).

[32] "IFF2400P17LE4 - Infineon Technologies." https://www.infineon.com/cms/en/product/power/igbt/igbt-stacks-igbt-assemblies/iff2400p17le4/ (accessed Jul. 07, 2020).

[33] Z. Liu, I. Cvetkovic, Z. Shen, D. Boroyevich, R. Burgos, and J. Liu, "Imbalance Mechanism and Balancing Control of DC Voltages in a Transformerless Series Injector Based on Paralleled H-Bridge Converters for AC Impedance Measurement," in *IEEE Transactions on Power Electronics*, Aug. 2019, vol. 34, no. 8, pp. 8175–8189, doi: 10.1109/TPEL.2018.2880866.

GLOSSARY

SMART	SMall Aspect Ratio Tokamak
efm	Electromotive force
Φ	Magnetic flux
PSFT	Plasma Science and Fusion Technology
CNA	Centro Nacional de Aceleradores
SCR	Silicon Controlled Rectifier
IGBT	Insulated Gate Bipolar Transistor
VEST	Versatile Experiment Spherical Torus
PROTO-SPHERA	PROTOtype Spherical Plasma for HElicity Relaxation Assessment
TFC	Toroidal Field Coils
PFC	Poloidal Field Coils
SB	Supercapacitor Bank
SM	Supercapacitor Module
ESR	Equivalent Series Resistor
PWM	Pulse Width Modulation